The Budding Transition of Phospholipid Vesicles: A Quantitative Study via Phase Contrast Microscopy

by

Hans-Günther Döbereiner

Dipl.Phys., Friedrich-Alexander Universität Erlangen-Nürnberg, 1989

A THESIS SUBMITTED IN PARTIAL FULFILLMENT
OF THE REQUIREMENTS FOR THE DEGREE OF
DOCTOR OF PHILOSOPHY
in the Department
of
Physics

SIMON FRASER UNIVERSITY
February 1995

APPROVAL

Name: Hans-Günther Döbereiner

Degree: Doctor of Philosophy

Title of thesis: The Budding Transition of Phospholipid Vesicles: A Quantitative Study via Phase Contrast Microscopy

Examining Committee: Dr. John Bechhoefer
Chair

Dr. Michael Wortis
Senior Supervisor

Dr. Evan Evans
Department of Physics
University of British Columbia

Dr. Michael Plischke

Dr. Barbara J. Frisken
Internal Examiner

Dr. Myer Bloom
External Examiner
Emeritus Professor of Physics
University of British Columbia

Date Approved: Feb. 27, 1995

PARTIAL COPYRIGHT LICENSE

I hereby grant to Simon Fraser University the right to lend my thesis, project or extended essay (the title of which is shown below) to users of the Simon Fraser University Library, and to make partial or single copies only for such users or in response to a request from the library of any other university, or other educational institution, on its own behalf or for one of its users. I further agree that permission for multiple copying of this work for scholarly purposes may be granted by me or the Dean of Graduate Studies. It is understood that copying or publication of this work for financial gain shall not be allowed without my written permission.

Title of Thesis/Project/Extended Essay

The Budding Transition of Phospholipid Vesicles: A Quantitative Study via Phase Contrast Microscopy.

Author: _____
(signature)

Hans-Guenther Doebereiner
(name)

3 March 1995
(date)

Abstract

In an aqueous environment and under appropriate conditions, amphiphilic molecules spontaneously self-assemble to form closed membrane capsules. The morphology of these fluid lipid vesicles is governed by the bending elastic energy of the membrane. Fluid vesicles exist in a variety of shapes, which may be considered phases in analogy to thermodynamics. This thesis describes experiments which explore the phase diagram of micron-scale phospholipid (SOPC) vesicles, concentrating on the region of prolate shapes. We have especially studied thermally induced parameter changes leading to budding, i.e., the spontaneous formation of a satellite from a prolate vesicle.

The observations are carried out via quantitative phase-contrast microscopy. A computer-based protocol is developed for analyzing the two-dimensional contour shapes of the video images. Reconstruction of non-spherical 3D shapes from 2D contour data is discussed in detail. We apply the general procedure to prolate vesicles near the budding transition. Experimentally measured shapes and shape trajectories are compared to theory.

There are two main contributions to the elastic energy for single component vesicles: First, an unconstrained bilayer resists bending elastically. Secondly, constraint on monolayer areas connected to vesicle closure leads to an overall stretching/compression of one monolayer relative to the other, which gives rise to an area-difference elastic contribution. Both contributions are found to be important for a quantitative theoretical understanding of the experimental data. They have been incorporated into the area-difference-elasticity (ADE) model, which forms the basis for the interpretation of vesicle shapes and shape transitions in this work.

Our main results are as follows:

- Fourier amplitudes describing the equilibrium prolate shapes exhibit a hierarchical structure dominated by a few low-order amplitudes, largely determined by volume and area constraints.

- The volume-to-area ratio of the vesicles and the effective spontaneous curvature of their membrane are measured. This allows for a mapping of prolate shapes into the phase diagram of the ADE model. We discuss corrections due to finite temperature and gravitational effects.

- In accordance with the predictions of the ADE model, the budding transition is found to be first order. We monitor enhanced fluctuations and increased relaxation times in vesicles approaching the spinodal line of the metastable prolate shape. The scaling behavior can be understood within the context of a simple Landau theory.

Acknowledgments

First and foremost, I want to say "Thank You" to my wife Inken who made me come to Vancouver. She and my daughter Lisa had to put up with my somewhat insane working hours. They both gave me much needed moral support.

I am very grateful for the scientific education I got from my supervisor Michael Wortis. I have learned Physics from him. He always gave me the freedom to develop my own ideas. Working with him is both a privilege and a challenge. He helped to clarify my thoughts and encouraged me to materialize them. During that process, he made sure all possible (and impossible) questions were asked.

I thank Evan Evans for giving me access to his laboratory at the University of British Columbia where the experiments for this thesis have been performed. With his amazing enthusiasm, he succeeded in conveying upon me the importance and the beauty of experimental membrane physics.

The results of numerous and endless discussions with Udo Seifert constitute an integral part of this work. His overnight responses to the hundreds of questions I have asked him via the internet have been impressive and very helpful. I acknowledge his contributions to the theoretical interpretation of my experiments.

The support from all members of the lab has been most important for the successful completion of this thesis. I am especially indebted to Wieslawa Rawicz who taught me the nuts and bolts of vesicle experiments. I have enjoyed very much working with her. Without the technical expertise of Andrew Leung, the "theorist" never would have turned into an experimentalist. Thanks a lot for your help. I apologize for chewing on the ears of my fellow students David Knowles, Ken Ritchie, and Tony Yeung. Especially Tony had to endure numerous vocal outbreaks of unfiltered thoughts. Thank you all for the open atmosphere in the lab. It has been fun to work with you guys.

Many thanks also to Ling Miao and Maria Nikolić who went along with me the stony path to meet the expectations of our boss. The discussions with you two have been most

helpful.

I acknowledge the hospitality of Erich Sackmann of the Technische Universität München where I have spent two month of enjoyable collaboration with him and Josef Käs. Thank you, Josef, for the part you had in converting me to experimental physics.

Last but not least, I wish to thank Cristin Hiergeist for keeping my spirits up during the final showdown. Let me close by thanking Bernhard for his advice.

Contents

List of Tables

List of Figures

Chapter 1

Introduction

1.1 Artificial and Biological Membranes: The Role of Phospholipid Bilayers

This thesis treats the shapes of artificially produced phospholipid vesicles. Each vesicle is a simple membrane capsule which separates interior and exterior aqueous regions. The capsule itself has a bilayer structure, consisting of an inner and an outer "leaf." Each leaf is a closely-packed layer of oriented phospholipid molecules. This bilayer structure forms spontaneously in aqueous solution because the phospholipid molecule is amphiphilic, consisting of a glycerol backbone attached at one end to two fatty-acid "tails" (hydrophobic) and at the other end via a phosphate linkage to an hydrophilic head group (choline in these experiments). The phospholipid molecules are highly insoluble in water because of the hydrophobic tails; but, under appropriate conditions, they self-assemble into the bilayer structure, with heads pointing out and tails pointing in, which effectively shields the hydrophobic regions of the molecules from aqueous exposure. In this work, we shall exclusively study vesicles of simple, spherical topology, although more complex topologies do occur and have been studied elsewhere [1, 2, 3, 4]. For further information on the chemical properties of phospholipids and on the various other phospholipid lyotropic phases (in addition to the bilayer phase) which they may form in aqueous solution, the interested reader is referred to an extensive literature [5].

The bilayer membrane may be in either a high-temperature "fluid" phase or a lower-temperature "gel" phase, separated by a well-defined thermodynamic phase boundary called the "main transition." The main transition [6] is (weakly) first order, with the membrane thickness D being slightly larger in the gel phase. For the phospholipids used in our studies,

the main transition occurs in the room-temperature range. It is believed to be driven predominantly by the entropy of the hydrocarbon tails of the phospholipid molecules. These tails are single-bonded, except for, typically, one double bond, which forces a single "kink" into one of the two tails. For an isolated chain, there is relatively free rotation about the C – C axis of each single bond, so the cis and trans configurations are close in energy. In the fluid phase, above the main transition, the typical chain configuration has many cis bonds, so in the bilayer the tails form a disordered fluid-like structure in which relative lateral motion of nearby molecules is easy and the structure has no shear rigidity. By contrast, below the main transition, these internal rotations are mainly frozen out, almost all bonds are trans, and the molecules are rod-like. These rod-like structures pack tightly into an hexagonal array, which resists shear and behaves at short distances effectively as a two-dimensional elastic solid. [1] The shape experiments described in this thesis are confined to the fluid phase. [2]

In the fluid phase, the membrane behaves roughly as a (two-dimensional) isotropic incompressible fluid. Since the membrane is self assembled, it has a preferred (relaxed) area a_0 per phospholipid head group and, in the absence of external constraints, there is no surface tension. [3] The area a_0 depends on the temperature T, so there is a well-defined thermal expansion coefficient [10],

$$\beta_A = \frac{1}{a_0}\frac{da}{dT} , \tag{1.1}$$

which will play an important role in what follows. Applied lateral tension can force the actual area per head group a to deviate from a_0. In the linear regime [4] the area elasticity is described by an elastic constant,

$$K = a\frac{d\tau}{da} , \tag{1.2}$$

where τ is the (isotropic) applied tension. In the experiments described herein, the number of molecules N in the membrane of a single vesicle is effectively fixed on laboratory timescales, since the lipid solubility is low. The relaxed area of the vesicle membrane is, therefore, close to a value $A_0 = Na_0/2$, since roughly half the lipid molecules are in each of the bilayer leaves.

[1] In the absence of tension, the long-wavelength state must, in fact, be hexatic, as originally pointed out by Nelson [7]. In fact, some tension is generated by the volume constraint, as footnoted below, so there are crossover effects. In addition, the molecules in the two-dimensional solid state are often tilted, an effect whose consequences for the shape problem have been explored by MacIntosh and Lubensky [8].

[2] The phospholipid bilayers which appear in biological structures are (almost) always in the fluid phase.

[3] Actually, in a vesicle, a small surface tension is generated at nonzero temperatures by the volume and area constraints.

[4] The membrane undergoes rupture at about 3% to 5% excess area per molecule [10].

It is important to distinguish between flaccid and turgid vesicles. The vesicle volume is set by strong osmotic forces. The bilayer is an effective barrier to solute species but not to water. Thus, water flows across the membrane until the internal and external osmolarity are balanced. If the required volume is larger than

$$V_0 = \frac{4\pi}{3}\left(\frac{A_0}{4\pi}\right)^{\frac{3}{2}} , \tag{1.3}$$

then elastic expansion of the relaxed area A_0 is required. [5] Under these conditions, the vesicle is "turgid," the dominant energy is just the stretching energy, and the vesicle shape is effectively spherical. For volumes less than V_0, the vesicle is "flaccid", its shape cannot be spherical, but a whole range of nonspherical shapes is available to accommodate the required volume. The elastic constant K is sufficiently large so that, under flaccid conditions and subject only to the tensions which are generated by the geometrical constraints , the area change is negligible and the overall area of the vesicle remains effectively fixed at A_0. Our experiments are for flaccid vesicles.

The mechanical energy of a flaccid vesicle is still elastic in origin. As we shall see in more detail in Chapter 2, there are two contributions. The first is a bending elasticity, which comes about because bending the membrane splays the constituent molecules of the bilayer leaves relative to one another. This changes their chain configurations and the relative position of the lipid headgroups and, thus, costs elastic energy. In addition, the constituent lipid molecules have, in general, a natural or spontaneous splay in the relaxed state. Any asymmetry of this tendency between the two leaves of the bilayer produces a tendency for the membrane to assume a curved configuration in its relaxed state. This deviation from a flat sheet may be described by a preferred or "spontaneous" radius of curvature R_0, described by the so-called spontaneous curvature parameter $C_0 = 1/R_0$. The second contribution is a direct consequence of the bilayer structure: "Flip-flop" processes, which transfer molecules from one leaf of the bilayer to the other, are slow on mechanical timescales [11, 12], principally because of the high energy necessary to drag the hydrophilic head group through the hydrophobic bilayer interior. Thus, the difference between the number of phospholipid molecules in the inner and outer leaves of the bilayer is effectively fixed and determines a difference ΔA_0 between the relaxed areas of the inner and outer leaves. If the overall configuaration of the vesicle is not consistent with this initial relaxed area difference, then one of the leaves must be stretched relative to the other, with a corresponding cost in elastic energy. Both these effects lead to contributions to the energy of order KD^2, where

[5] Of course, if A_0 is too small, rupture occurs.

D is the thickness of the bilayer, so it is crucial to include this relative stretching of the monolayer leaves in the shape problem. [6] At room temperature, KD^2 is typically large on the scale of the thermal energy k_BT, so mechanical considerations apply to the overall vesicle shape, and thermal fluctuation effects are usually (but not always) small for micron-scale phospholipid vesicles. [7]

The equilibrium shape of a vesicle is determined by minimizing the mechanical energy. If the vesicle starts from a nonequilibrium configuration or if the parameters of the system are abruptly changed, the vesicle shape relaxes to the new condition of mechanical stability by a complicated dynamics which involves a combination of shape evolution, two-dimensional flow in the membrane, three-dimensional bulk flow in the surrounding fluid, and sliding of one monolayer over the other. For the micrometer-scale vesicles of our experiments, typical relaxation times are in the range $10^{-2} - 10^2$ s.

So far, we have sketched the behavior of ideal single-component laboratory vesicles. Nature uses phospholipid bilayer membranes in a wide variety of biological structures. Because of functional requirements, such membranes are typically far more complex than the simple membranes described above. We will briefly mention some of the added structure in the following paragraphs.

First of all, biological membranes are chemically complex and contain many different lipid and nonlipid species. There are a variety of distinct phospholipids, with different headgroups (charged and uncharged) and different hydrocarbon chain lengths. There is also another major class of lipids, the so-called glycolipids, which play an important role in signal transduction and targeting [13]. And, then, of course, there is cholesterol, which is believed to have a mainly structural role, strengthening the membrane and, at the same time, widening the temperature range of the fluid phase [9].

Second, according to the fluid mosaic model [14], the fluid bilayer serves as a matrix for functional proteins, which may be incorporated into the membrane as transmembrane proteins or adsorbed on the membrane surface. Indeed, by weight, most of a typical biomembrane consists of proteins, so one has to be very careful in generalizing properties of a pure lipid bilayer to those of biomembranes. An (arbitrary) example of the plethora of such specific functional proteins are molecular pumps, which regulate the chemical composition

[6] By contrast, the energy cost of an overall stretching of both leaves is of order KA_0, which is much larger than the bending-energy contribution. Thus, such overall area changes are strongly suppressed, as noted above.

[7] The generic technical statement is that thermal fluctuation effects are small as long as the vesicle size is significantly smaller than the de Gennes-Taupin persistence length, $\xi_p \approx a_0 exp(4\pi\kappa/3k_BT)$. In fact, even this statement requires qualification: Near a shape instability one or more fluctuation modes become soft. Such soft modes can have important thermal effects, as we shall see in Chapter 6, even when ξ_p is large.

of the cytoplasm and the interior of the cellular organelles.

And, third, proteins anchored in the lipid-bilayer matrix may form interlinked structures, which give the otherwise-fluid membrane some of the (solid) elastic structure of a cross-linked network. A particularly simple example is the spectrin network of the red-cell cytoskeleton.

The red blood cell (rbc) is one of the simplest biological membranes; nevertheless, all of the above complexity is realized even in such a "minimal model." The rbc membrane has receptors in the so-called glycocalix, which extends out into the exterior fluid. It employs protein pumps incorporated into the phospholipid bilayer. And, it possesses a cytoskeletal structure, including a spectrin network, which is attached on the cytoplasmic side of the membrane. The rbc cytoskeletal network is restricted to the vicinity of the plasma membrane and does not extend more than about 100 nm into the cell interior. [8] More typically, in other cells the cytoskeleton extends deep into the cytoplasmic interior of the cell. Nevertheless, biochemical properties first identified in the rbc have often proven to be of general significance, and the rbc continues to serve as a useful paradigm [15].

All the additional elements just enumerated influence the properties of the lipid bilayer. In turn, the (elastic) properties of the bilayer have consequences for protein function [16]. The whole system can only be described as a composite entity. Although a full physical description of a real biological membrane is beyond present capabilities, one may hope that the identification of some specific membrane properties and their separate study in well defined artificial systems or simple biological systems (such as the rbc), which are sufficiently controllable to allow a quantitative description, will contribute to an understanding of membrane function in the cellular environment. For further discussion of the possible role of elastic energies in the cell, we refer the reader to [17, 18, 19].

In the previous few paragraphs, we could only give a glimpse of some of the properties of real membranes. There is a much wider spectrum of research on the physics of membranes. An overview of the field can be obtained in various reviews and proceedings [21, 22, 23, 24].

1.2 The Shapes of Red Blood Cells and Artificial Vesicles: A Brief History

In this Section, we review some of the early history of vesicles shapes. Such work was originally motivated largely by biological structures, shape studies of red blood cells under various conditions being a prototype example.

[8] The interior of the rbc is filled with hemoglobin.

The biconcave discoid shape of the normal resting rbc has long been observed in microscope pictures. There have been many studies of abnormal rbc shapes, including both clinical observations of pathological shapes [25] and, more recently, in vitro studies of rbc shape changes induced by chemical treatment [26]. In these studies, different chemical treatments produce different cell morphologies in a systematic manner. Observed shapes range from cup-shaped stomatocytes to crenated and echinocytic cells.

Before theoretical models of rbc shape could be proposed, it was necessary to understand the membrane microstructure. The first evidence for the existence of the bilayer was found in 1925 by Gorter and Grendel [27]. However, it was not until the early 1970's that it was recognized that biological membranes generally have a composite structure, with a fluid lipid bilayer [14] containing proteins which form or are chemically linked to a cytoskeletal network.

On the basis of these structural observations, elastic models of rbc shape were proposed starting in the 1970's. Canham proposed in 1970 [28] that the dominant energy of the rbc was a bending energy (see Sec. 2.2) and that the normal rbc shape could be understood as one which produces a minimum of this bending energy.

Canham's work did not include a spontaneous curvature. Coming from a background in liquid crystals, Helfrich in 1973 [29] generalized Canham's work to include a spontaneous curvature (of unspecified origin) to describe the tendency of a vesicle for concave or convex curvature.

In 1976 Deuling and Helfrich [30] used a variational procedure to minimize the bending energy. By exploring a range of parameters such as vesicle area, volume, and spontaneous curvature, they were able to produce a "catalogue" of vesicle shapes which included the native shape of the rbc, the discocyte, and most but not all of the pathological rbc shapes observed in experiments. In a later paper [31], they compared the theoretically obtained shapes to experimental rbc contours, gathered in pioneering work by Evans and coworkers [32].

Both Canham and, originally, Helfrich treated the membrane as a single elastic layer, with no explicit reference to bilayer structure. The importance of the bilayer structure was first noted in 1974 by Sheetz and Singer [33] in the form of the "bilayer-couple hypothesis." In the same year, this concept of a bilayer-couple was formulated in the context of elasticity theory by Evans [34] and Helfrich [35]. It was noted by these authors that the shape of a closed bilayer vesicle should, because of elastic effects, depend on the difference ΔN in the numbers of molecules contained by the two constituent monolayers of the bilayer. This

idea was further developed in 1989 by Svetina and Zeks [36] who performed actual shape calculations allowing for an effective non-local spontaneous curvature induced by the area difference[9] $\Delta A_0 \propto \Delta N$.

It was demonstrated experimentally by Evans and coworkers in the 1970's [37] that the rbc has an appreciable resistance to shear. Its plasma membrane is, therefore, not completely fluid, which is an important realization with regard to the problem of the rbc shape. On the basis of these observations Evans proposed in 1980 [38] a model for rbc shape which included shear elasticity. It is now clear that this shear rigidity is caused by the spectrin network of the rbc, which is coupled to the membrane by specific protein complexes. [10] The issue of how much this network influences or even dominates cell shape is controversial and not yet resolved. It is evident, however, that the spectrin network serves to support the membrane structure and provides the rbc with the necessary robustness it needs in order not to be torn apart in the fine capilaries each rbc is pumped through repeatedly during its life cycle.

The biological reason(s) for the biconcave shape of the rbc are not clear. It could be that this shape represents the optimal compromise between low resistance to tank treading of the cell in the blood vessels, which would be lowest for a sphere, and sufficient deformability to squeeze through small capillaries.

Nonbiological vesicles, artificially produced from a single pure lipid species, offer the possibility of studying vesicle-shape behavior without the complications of the cytoskeleton or of the multicomponent lipid mixture which characterizes all biological membranes. Vesicles with a diameter on the order of 100 nm have been studied extensively because of possibilities for medical and cosmetic applications. However, shape observations of such objects are difficult and have only been achieved recently by cryo-electron microscopy [40].

Thus, to date, laboratory vesicle-shape studies have concentrated on giant vesicles, with typical diameters in the range of 2–20 μm. Shape studies on giant vesicle were initiated by Duwe, Engelhardt, and Sackmann in 1986 [41]. The first systematic work was done in 1990[11] by Käs and Sackmann [49, 50]. These latter measurements were mainly conducted with single-lipid vesicles in distilled water. Shape changes were induced by controlling the volume-to-area ratio of the vesicles. This ratio can be decreased by osmotic deflation of the vesicle volume or by thermal expansion of the membrane area. As more area becomes

[9] In this work, the geometrical area difference ΔA was constrained to be equal to the molecular area difference ΔA_0.

[10] Important proteins are Actin, Band 3, Band 4.1, and Glycophorin A [39].

[11] Earlier experiments with artificial giant vesicles focused on the measurement of the elastic bending modulus [42]and were done by a large number of groups. [43, 44, 45, 46, 47, 48]

available, nearly spherical vesicles generally deform into oblate or prolate ellipses. Under further deflation, these shapes eventually become unstable to other morphologies. One of these shape transitions is the so-called budding transition, where a small bud is expelled from the parent vesicle (see Fig. 1.1). Depending on the spontaneous curvature C_0 and area difference ΔA_0 of the membrane, such processes can also lead to "inverted" shapes where some exterior fluid is engulfed to form a stomatocyte or even an internal bud.

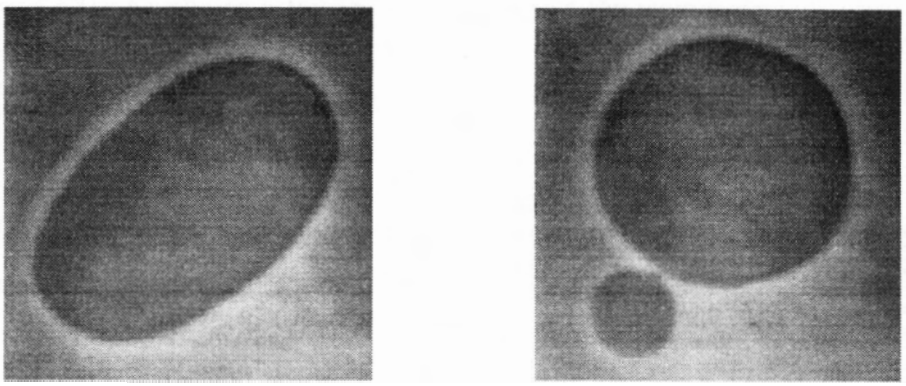

Figure 1.1: Example of a budding transition. For large positive spontaneous curvature C_0 (and/or large differential area ΔA_0), prolate vesicle shapes become unstable to budding as the volume-to-area ratio is decreased. The two video pictures show snapshots of a fluctuating vesicle before and after the budding transition. The pictures were obtained by phase contrast microscopy. The focal plane defines a cut through the vesicle body. It has been set in such a way as to include the axis of rotational symmetry of the vesicle.

Changing temperature affects not only the volume-to-area ratio of a vesicle but also the area difference between the monolayers (and possibly the spontaneous curvature). As will be described in Chapter 2, these two (three) parameters determine the vesicle shape, so temperature is an effective experimental control parameter which drives vesicles along thermal trajectories in a two-dimensional[12] parameter space.

Experimental trajectories were interpreted by Berndl, Käs, Lipowsky, Sackmann, and Seifert [50, 49] using the so-called ΔA or area-difference model. [13] This model focuses on the bilayer aspect of the membrane. It assumes that the geometrical area difference between the exterior and the interior monolayers is directly proportional to the difference in the number of molecules, i.e., it does not allow for relative stretching or compression of the monolayers. The budding transition is predicted to be a second-order transition in this model [51]. The up/down symmetry of a prolate vesicle is continuously broken in the

[12] It turns out that the spontaneous curvature and the area difference influence the shape only through a combined quantity, which will be defined in Sec. 2.4.

[13] Historically, this model was also called the bilayer-couple model [36].

transition to a pear-shaped vesicle, which then *smoothly* evolves into a budded configuration as the volume-to-area ratio is further reduced. In contrast, the experiments performed in [49] find a continuous symmetry breaking to a pear shape, followed by a *sudden* necking down of the pear to form the bud [50].

A spontaneous first-order transition was, in fact, predicted by Miao, Fourcade, Rao, Wortis, and Zia [52] as well as by Seifert et al. [51] for the spontaneous-curvature (SC) model (see Sec. (2.2)), which neglects the bilayer aspect of the membrane but introduces a preferred curvature of the membrane. In this transition, however, the bud is expelled directly from the symmetric prolate state, and no stable weak pears (as apparently observed in [50]) are predicted. Thus, it would appear that neither of the two earlier models is capable of fully describing the experimental situation. It is a central goal of this thesis to resolve this puzzle by interpreting the data within the context of a more general bending-energy model, the area-difference elasticity (ADE) model (see below).

In the experiments cited above, shape transitions were induced by thermally controlling the volume-to-area ratio and the area difference of the vesicles. One can also keep the volume-to-area ratio fixed and change only the difference in molecular area between the outer and inner monolayer. This differential area can be set by controlling the difference in the number of molecules via a pH gradient across the membrane. This technique has been developed by Cullis and collaborators for a lipid mixture of phosphoridylcholine and phosphoridylglycerol [53] [14] and was applied successfully by Mui et al. [54] to large unilamellar vesicles (LUV's) with a mean diameter of 100 nm. [15] Experimentally observed shapes (see Fig. 1.2) resemble semi-quantitatively theoretically obtained contours. This result is encouraging and strongly supports the notion that bending elasticity is a valid concept to describe shapes of membranes over a range of length scales.

The differential area of vesicles can be changed not only by pumping lipids from one monolayer to the other but also by selectively removing molecules from the outer monolayer or adding them to it. This can be achieved by setting the chemical potential of membrane area via certain additives to the exterior solution. [16] Experiments by Farge and Devaux

[14] The pH gradient controls the degree of dissociation of the glycerol headgroup. Since the neutral form has a higher flip-flop probability than the charged one, the phosphoridylglycerol lipids distribute asymmetrically across the membrane. Setting the pH gradient, thereby, allows to control the number difference between the two monolayers, and, thus, the differential area.

[15] In the biochemical literature these vesicles (100 nm), which are prepared by extrusion, are called large as opposed to small vesicles (25 nm) produced by sonification.

[16] The monolayer area is set by the chemical equilibrium between additives within the membrane and in bulk solution. This equilibrium can be controlled by the concentration of additives, like lyso-lipids, or albumin.

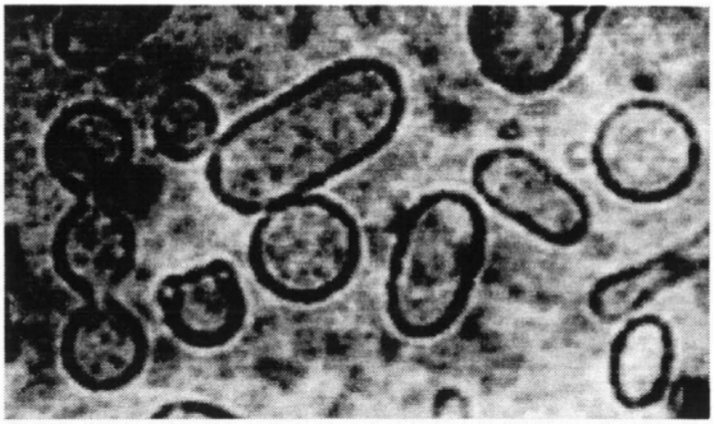

Figure 1.2: Example of Nanometer Vesicle Shapes. The picture was obtained via cryo electron microscopy [54]. Shapes with various volume-to-area ratios are visible. All observed shape contours (in this picture) have a theoretical counterpart obtained via minimization of the bending energy of the ADE model.

[55] used this idea to modify the shapes of giant (μm) vesicles. These papers [54, 55] demonstrate clearly that an excess of molecules on the outer monolayer leads to outwardly curved shapes, whereas an excess of molecules on the inner monolayer results in inwardly curved morphology.

In vesicles composed of a single lipid species the topology usually does not change during the budding transition, i.e., full fission does not occur and the bud remains attached to the parent vesicle by a narrow neck. However, in multi-component vesicles the bud can fission off from the parent (see Fig. 1.3). This process has been studied in vesicles prepared from the natural phospholipid sphingomyelin by Döbereiner, Käs, and collaborators. Fission was found not only in giant vesicles with a size of about 10 μm but also in much smaller vesicles on the submicron scale. [19]

None of the vesicle-shape data gathered in all of the experiments mentioned above has been compared in detail to theory. So far, the interpretation of experimental vesicle shapes has been limited to the identification of symmetry classes and estimated thermal trajectories.

The major accomplishment of this thesis is the development of a technique for quantitative shape measurement. From data collected by this technique, all the elastic parameters relevant for vesicle shapes can in principle be extracted. Thermal shape trajectories are

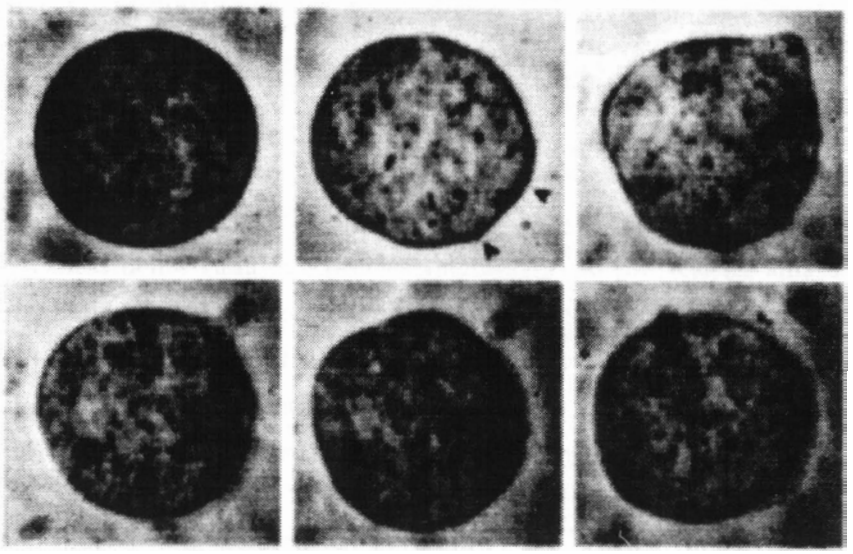

Figure 1.3: Example of fission of sphingomyelin vesicles. The video sequence shows the expulsion of a small bud as the volume-to-area ratio is decreased. After spontaneous budding, the satellite separates from the parent vesicle (see the last picture).

followed in detail through the parameter space and described within the ADE model, which will be introduced in Sec 2.4.

Because it interpolates between the two previous models (SC and ΔA), the ADE model provides a convenient framework for comparison of theoretical and experimental shapes and shape trajectories. This model, parts of which were originally proposed in 1974 by Evans [34, 38] and Helfrich [35], was derived from a simple mechanical model of the bilayer in 1985 by Svetina, Brumen, and Zeks [56]. [17] In 1992, the first actual shape calculations in that model were performed by Miao et al. [57, 58, 59].

In this thesis, the ADE model is tested in several ways. We find that it is, indeed, necessary to include aspects of both the SC and ΔA models in treating the bending elasticity of the bilayer in order to account for all experimental vesicle-shape observations.

[17] A systematic derivation of the ADE model along the same lines can also be found in [57, 58].

1.3 An Overview of the Thesis

Chapter 2 reviews the ADE model and its predecessors. This material provides a context and a language for describing the experimental observations. A schematic phase diagram of the ADE model is given.

Chapter 3 is devoted to a description of experimental techniques, including sample preparation, chamber construction, and data collection. For stable observation of vesicle shapes over long times, it is necessary to restrict motion of vesicles so that their shapes can effectively be monitored in a fixed focal plane. This is done by making the surrounding aqueous solution slightly less dense than the vesicles themselves, so the vesicles sink to the bottom of the measuring chamber. For prolate vesicles, then, the symmetry axis remains in or close to a single horizontal plane. Observations of vesicle shape are done by phase contrast video microscopy, looking upward through the transparent floor of the experimental chamber. Thus, the upshot of the experiments is a set of two-dimensional video images, which may be computer analyzed in real time[18] or stored on tape for later use. The algorithm used to digitize the vesicle contours is described in detail.

Chapter 4 discusses the procedures we have developed for analyzing these digitized vesicle contours. Much of our work is focussed on the part of the (shape) phase diagram which includes strongly prolate shapes, both near and beyond the budding boundary. To parameterize such shapes, we have developed a mode expansion based on identifying the mean symmetry axis and expressing the contour angle with respect to this axis as a function of the arclength from the pole. We address the principal problems and uncertainties with regard to finding the correct reference frame for analyzing a fluctuating shape and for reconstructing three-dimensional shapes from two-dimensional contour data.

In Chapter 5, we are (mostly) interested in the fluctuation spectrum of a vesicle. We analyze in detail a particular set of vesicle-shape thermal trajectories, in which a prolate shape becomes unstable to bud formation as temperature is increased. We argue from the data that this instability of the symmetric prolate is, in fact, a spinodal instability marking the limit of stability of a metastable branch of shapes. The experimental data on the variation of static and dynamic shape fluctuations are consistent with a simple Landau theory based on an order parameter which measures the up/down asymmetry of the vesicle shape. We observe that vesicles are in general slightly asymmetric, even in the theoretically "symmetric" prolate state of the ADE model.

In Chapter 6, the mean shape amplitudes are analyzed for a range of vesicles. This

[18] This does not imply that each video frame is analyzed.

information is then turned into a consistency check of the validity of the ADE model. To place each vesicle in the phase diagram, one needs not only the volume-to-area ratio of the vesicle, which can be infered directly from shape geometry, but also, as it turns out, a combination of variables which measures the spontaneous curvature and the monolayer area difference. Once these parameters are known, each vesicle can be located on an experimental phase diagram, which can then be compared with its theoretical counterpart. In principal, all elastic parameters relevant for vesicle shapes can be obtained from an analysis of the thermal shape trajectories. However, this analysis is complicated by finite-temperature and gravitational corrections to the vesicle shape, and we address these issues as well as we can.

In Chapter 7, we summarize our work and collect all the evidence in support of the ADE model. One central question is whether the budding transition is a continuous or discontinuous transition. We argue in this thesis that our data are consistent with an interpretation of budding as a discontinuous first-order transition with hysteretic behavior in accordance with the ADE model.

Chapter 2

Theory of Vesicle Shapes

This Chapter presents the theory of shapes of fluid-phase lipid vesicles. As emphasized originally by Canham [28], the equilibrium shape of a vesicle is expected to be that shape which (globally) minimizes its energy subject to appropriate constraints. More generally, a shape may be mechanically (meta-) stable, if it is a local energy minimum subject to appropriate constraints. In either case, identification of the right energy functional (with its associated constraints) is the central theoretical issue.

Historically, there have been two somewhat different bending-energy models, which are now incorporated into a single more-general model, the area-difference elasticity (ADE) model. In Secs. 2.2 and 2.3, we will define for completeness the earlier spontaneous curvature (SC) and area-difference (ΔA) models. The general ADE model is described in Sec. 2.4. The important parameters of the ADE model will be introduced and discussed and the general features of the predicted shape (phase) diagram for low-temperature structures will be described. The summary of results in Sec. 2.4 will be restricted to a generic description only. Specific results will be cited later in the text, as they are needed in the discussion of the experimental results.

2.1 Geometrical Constraints

Since constraints come into all three models, it is appropriate to discuss them at the outset:

(a) Fixed volume. All three models constrain the vesicle volume V. Physically, this requirement arises because the membrane is permeable to water but not to solvent molecules (on the timescale of mechanical experiments). Thus, the volume of the vesicle responds immediately to any difference in osmolarity between the interior and

exterior aqueous environments. The energies involved in this osmotic balance are large on the scale of bending energies, so, once achieved, osmolarity balance assures volume conservation during mechanical shape equilibration. It is, thus, the *permeability* of the membrane to water which is responsible for the *constancy* of the enclosed water volume at given osmolarity. The amount of osmolarity difference which can be induced by membrane curvature depends on the curvature scale. This difference can be estimated by equating the change in bending energy E_B with volume V to the osmotic pressure [51], $\frac{\partial E_B}{\partial V} \simeq \frac{8\pi\kappa}{V} = RT\ \Delta n$, where R is the gas constant; T, the temperature; and Δn, the molarity difference. With $\kappa = 10^{-19}J$ and $V = \frac{4\pi}{3}(10\mu m)^3$, one finds at room temperature the extremely small number $\Delta n \simeq 10^{-10}$ mol/l. Keeping the volume constant during minimization is, therefore, an excellent approximation.

(b) Fixed area. All three models constrain vesicle membrane area A. This requirement is a consequence of the existence of the preferred, relaxed area a_0 per headgroup, as introduced in Chapter 1. The relative importance of membrane area elasticity versus bending elasticity can be investigated employing a simple model of stress distribution within the bilayer [57, 58]. In this approach, each monolayer is taken to consist of two hypothetical surfaces (representing the heads and tails of the lipid molecules), where all the elastic forces are imagined to be concentrated. Each individual surface has a preferred area but does not resist bending. The bending elasticities of the monolayers individually and of the bilayer as a whole are a result of the relative stretching/compression of these surfaces relative to one another. One finds that the energy scale for an overall expansion of the bilayer area is larger than that for a for pure bending deformation without overall stretch by a factor $(R_A/D)^2 \simeq 10^6$, where $R_A = (A/4\pi)^{\frac{1}{2}}$ is the area-equivalent radius of the vesicle which measures the overall scale of the membrane curvature. It is, thus, a very good approximation to assume that the membrane area is fixed.

(c) Fixed area difference. This constraint enters only in the ΔA model. In the ΔA model, the area difference ΔA between the outer and inner leaves of the bilayer is assumed fixed. Under the assumption of fixed membrane thickness D, the area difference ΔA is directly connected to the vesicle shape via a simple geometrical relation to the integrated mean curvature,

$$\Delta A = D \int dA(C_1 + C_2) \quad + \quad O(D/R_A), \tag{2.1}$$

where C_1 and C_2 are the local principal curvatures of the membrane. The integral runs over the full vesicle surface. Now, the requirement of a fixed area difference reflects the picture that (i) the number of lipid molecules, N^{out} and N^{in}, in the inner and outer leaves of the bilayer are separately conserved for low-solubility lipids in the absence of flip-flop and (ii) the actual area difference ΔA is proportional to the fixed difference $N^{in} - N^{out}$ via the relation,

$$\Delta A = \Delta A_0 = A_0^{out} - A_0^{in} \simeq a_0(N^{out} - N^{in}) \,, \tag{2.2}$$

which equates ΔA to ΔA_0, the relaxed area difference of the two monolayers. Under these assumptions, the fixed value of N^{out} and N^{in} places a hard constraint on the integrated mean curvature of permissible vesicle shapes. In fact, as we shall argue in Sec. 2.4, assumption (i) is valid but assumption (ii) is false, and, indeed, the elastic-energy contribution of a difference between ΔA and ΔA_0 is entirely comparable to the bending energy. Thus, the assumptions of the ΔA model are not really viable.

We come now to a discussion of the three bending-energy models.

2.2 The Spontaneous Curvature Model

In the SC model, the elastic bending energy is obtained by integrating over the whole vesicle area the contributions from local deviations in mean curvature from the preferred relaxed state. Helfrich's original model [29, 30] is based on the following Hamiltonian:

$$H_{SC} = \frac{\kappa}{2} \int dA (C_1 + C_2 - C_0)^2, \tag{2.3}$$

where κ is the (local) bending modulus. The spontaneous curvature C_0 explicitly recognizes the possibility that the relaxed state of the membrane is not flat. In the SC model the shape is found by minimizing Eq. (2.3) for given, fixed enclosed volume V and membrane area A of the vesicle.

Generally, we expect that elastic energies should be independent of overall translations and rotations of the vesicle. For this reason, we expect that an energy functional such as Eq. (2.3) should depend only on local Euclidean invariants of the vesicle shape. Low-order surface invariants can all be built from the local curvature tensor $\mathcal{C}$, whose eigenvalues are the principal curvatures C_1 and C_2. Isotropy (of the fluid membrane) prohibits invariants which distinguish between the two principal axes. Thus, to second order in the curvature, the only available invariants are Tr $\mathcal{C} = C_1 + C_2$ (the mean curvature), (Tr $\mathcal{C}$)^2, and Det $\mathcal{C} = C_1 C_2$

(the Gaussian curvature). Equation ((2.3) contains the first two of these invariants. The third has been omitted, since the Gauss-Bonnet theorem [60] guarantees that the integral of the Gaussian curvature over a closed surface is a topological invariant. Since we shall be considering vesicles of fixed, spherical topology, such a term contributes to the energy only an uninteresting constant.

2.3 The Area-Difference Model

The ΔA model is based on a Hamiltonian which is formally identical to (2.3) with C_0 set to zero:

$$H_{AD} = \frac{\kappa}{2} \int dA (C_1 + C_2)^2 \tag{2.4}$$

The energy minimization is now taken at fixed ΔA in addition to fixed V and A. Inspection of Eqs. (2.3) and (2.4) reveals that the SC and ΔA models are related via a Legendre transformation, in which C_0 and ΔA are conjugate variables. Thus, including a spontaneous curvature in the Hamiltonian (2.4) would only add an irrelevant constant term. The Legendre-transformation connection means that the two models have, in fact, the same set of shapes as stationary-energy solutions. This *does not* imply, of course, that the phase diagram is the same, since at equilibrium it is the lowest energy stationary shape which is selected and this will in general be different for the different models.

2.4 The Area-Difference-Elasticity Model

2.4.1 The Hamiltonian

The ADE model can be derived [56, 57, 58] starting from the model of stress distribution within the bilayer mentioned in Sec. 1.2. As was already pointed out, the energy scale for an overall expansion of the bilayer area is much larger than for pure bending of the membrane. However, the bending contributions which come from relative stretching and compression of the monolayers at fixed bilayer area are of the same order in an expansion in D/R_A as those which originate from bending the monolayers separately. The upshot is that the mean area $A_0 = (A_0^{out} + A_0^{in})/2$ can be assumed fixed, whereas changes in the area difference $\Delta A = A^{out} - A^{in}$ away from its relaxed value $\Delta A_0 = A_0^{out} - A_0^{in}$ have an elastic energy cost which is entirely comparable to the bending energy. Thus, the assumption in the ΔA-model of a fixed area difference is untenable and must be dropped.

The ADE model consistently keeps all terms up to order $O(D/R_A)$ and is given by

$$H_{ADE} = \frac{\kappa}{2}\int dA(C_1 + C_2 - C_0)^2 + \frac{\bar{\kappa}}{2}\frac{\pi}{AD^2}(\Delta A - \Delta A_0)^2 \,, \tag{2.5}$$

where $\bar{\kappa}$ is called the nonlocal bending modulus of the membrane. In the ADE model, the shape is found by minimizing Eq. (2.5) at fixed enclosed volume V, membrane area A, and relaxed area difference ΔA_0 of the vesicle. Note that, while the first term is an integral of a local quantity, the second term depends on the square of the area difference (2.1) and, therefore, appears to be nonlocal. Actually, this term arises as the integral of an elastic energy associated with the local area compressibility of the monolayers. The fact that the two-dimensional (fluid) density becomes uniform over the individual monolayers [1] allows the elastic field to be eliminated from the problem and leads to the apparently nonlocal shape interaction [58]. We shall find in what follows that the relaxation of the constraint $\Delta A = \Delta A_0$ makes the physics of the ADE model very different from that of the ΔA model.

Because the extra term in the ADE energy functional only depends on the vesicle shape through the variable ΔA, it follows that the catalogue of stationary shapes for the ADE and ΔA models are the same. We shall use this fact extensively in Chapter 6, when we discuss the mapping of the experimental shapes into the ADE-model phase diagram.

In the remainder of this section, we discuss the important control parameters of the ADE model. The two elastic moduli κ and $\bar{\kappa}$ have units of energy. At $T = 0$, where the overall energy scale disappears, it is only the ratio,

$$\alpha = \frac{\bar{\kappa}}{\kappa} \,, \tag{2.6}$$

which is relevant to the shape problem. The remaining parameters in the energy functional (2.5) are all lengths and areas. Thus, the dimensionless factors which multiply κ and $\bar{\kappa}$ are invariant under a transformation that rescales all lengths by the same factor. We exploit this invariance by choosing a length scale based on the area-equivalent radius, R_A defined by $A = 4\pi {R_A}^2$. This allows us to introduce the following dimensionless quantities:
The reduced volume,

$$v = \frac{V}{(4\pi/3)R_A^3}, \tag{2.7}$$

the reduced value of the relaxed area difference,

$$\Delta a_0 = \frac{\Delta A_0}{8\pi D R_A}, \tag{2.8}$$

[1] Since the monolayers can slide past one another, they are uniformly stretched or compressed in equilibrium. In general, there are cross terms between bending and stretching contributions to the energy, which lead to a non-uniform monolayer density. These terms come in only in higher order and are smaller by a factor $(D/R_A)^2 \simeq 10^{-6}$ [58].

and the reduced spontaneous curvature,

$$c_0 = C_0 R_A \ , \tag{2.9}$$

as well as $\Delta a = \Delta A \ / \ (8\pi D R_A)$ and $c_i = C_i R_A, \ i\epsilon\{1,2\}$, in parallel with Eqs. (2.8) and (2.9). In terms of these quantities, we may reexpress the energy functional (2.5) in scaled form,

$$\frac{H_{ADE}}{(4\pi)^2\kappa} = \frac{1}{8\pi}\int da\,(c_1+c_2)^2 + \frac{\alpha}{2}\left(\Delta a - (\Delta a_0 + \frac{1}{2\pi\ \alpha}c_0)\right)^2 + \text{ const }, \tag{2.10}$$

where $da = dA/(4\pi R_A^2)$. Note that, in this form, the relaxed area difference Δa_0 and the spontaneous curvature c_0 appear only in the combination,

$$\overline{\Delta a_0} = \Delta a_0 + \frac{1}{2\pi\ \alpha}\ c_0. \tag{2.11}$$

This observation is already evident in Eq. (2.5), since, apart from uninteresting, shape-independent terms, C_0 and ΔA_0 both enter only as multipliers of the integrated mean curvature. It will play an important role in our analysis in Chapter 6.

The three relevant dimensionless parameters of the ADE model are, therefore, α, v, and $\overline{\Delta a_0}$. We now discuss each one briefly:

The ratio α measures the relative importance of the two terms in Eq. (2.10). For $\alpha = 0$ there is no resistance to bending from differential area elasticity, and one recovers the SC model. For $\alpha \to \infty$ the geometrical area difference ΔA does not deviate from the preferred area difference ΔA_0 of the monolayers, and the ADE model reduces to the ΔA-model. The dimensionless parameter α has been estimated as 1.4 for SOPC, and generally is of the order of unity for common phospholipids [58]. This estimate is directly corroborated by recent measurements [61], thus demonstrating the necessity of treating the two terms in Eq. (2.10) on an equal basis. Note that the ratio α of elastic moduli is characteristic of the lipid molecules (and to a lesser extent their aqueous environment) but should not vary between one vesicle and another in the same preparation.

The reduced volume v is a purely geometrical quantity and measures in effect the membrane area available for shape changes. Spherical vesicles ($v = 1$) have no freedom to adjust their shape. For smaller reduced volume v, more shape geometries become available and the branch structure of the minima of Eq. (2.10) gets increasingly complicated. A completely collapsed vesicle, without any interior volume, would correspond to $v = 0$.

The parameter $\overline{\Delta a_0}$ measures the tendency of the membrane to curve. We may call it an effective area difference or, alternatively, an effective spontaneous curvature, depending on

the viewpoint. In any case, it reflects the different sources of preferred membrane curvature. A large positive scaled area difference Δa_0 tends to curve the membrane outward, while a small or negative value favors invaginated shapes. Likewise, a scaled spontaneous curvature c_0 different from unity would favour outwardly or inwardly curved shapes with respect to the unit sphere. [2] It is the combination of the two parameters which determines the shape, the relative contributions being fixed by the ratio α of elastic moduli.

2.4.2 The Phase Diagram

For given α, the $T = 0$ equilibrium shape of a vesicle is uniquely determined by the two control parameters v and $\overline{\Delta a_0}$. As these parameters vary, the equilibrium vesicle shape (i.e., the lowest-energy shape) changes. Almost everywhere in the two-dimensional (v,$\overline{\Delta a_0}$) phase space, the change is smooth; thus defining distinct regions of a (shape) phase diagram. Across special loci in the two-dimensional phase space, the shape may change in a nonanalytic manner, thus defining phase boundaries. The shape change across a phase boundary may be abrupt ("first-order," discontinuous) or it may be smooth ("second-order," continuous), as when a shape evolves smoothly from one symmetry class to another ("symmetry breaking"). A generic example of such a (shape) phase diagram for the ADE model is shown in Fig. 2.1. From a theoretical perspective [58], such a phase diagram reflects the structure of the solutions of the variational equations which express the minimization of the energy functional (2.10) subject to appropriate constraints. These Euler-Lagrange equations [52] are highly nonlinear and have, in general, many solutions, describing different branches of stationary shapes. Along any given branch, shapes generally change smoothly, as the control parameters are varied. At nondegenerate points in the phase diagram, one of the solutions has an energy which is less than all others. At phase boundaries, two or more solutions become degenerate. A first-order transition occurs, when two branches (corresponding to different shapes) cross, one replacing the other as the equilibrium (lowest-energy) shape. Second-order boundaries occur when the lowest-energy branch undergoes a bifurcation.

A brief discussion of the general features of the phase diagram of the ADE model [62, 63] is given in the caption of Fig. 2.1. A detailed examination of the part of the diagram which is relevant for the experimental results presented in this Thesis, i.e., the region of the budding transition, will be done later in Sec. (5.1).

[2] A flat membrane sheet would be stable for $\overline{\Delta a_0} = 0$.

Figure 2.1: Generic ADE Phase Diagram for $\alpha = 1.4$. The control parameters of vesicle shapes are the reduced volume v and the effective differential area $\overline{\Delta a}_0$. The reduced volume v describes the geometrical quantity volume-to-area ratio and is normalized to unity for the sphere, which is the largest possible value. Thus, going from the right to the left in this diagram, the volume of vesicle shapes decreases until, at $v = 0$, there is no internal space left. The effective differential area $\overline{\Delta a}_0$ describes the tendency of the membrane to curve. Roughly, positive values $\overline{\Delta a}_0 \gtrsim 1$ correspond to outwardly curved shapes, whereas values $\overline{\Delta a}_0 \lesssim 1$ correspond to inwardly curved shapes. The shapes depicted in the diagram are globally minimal energy shapes of the ADE bending energy. Their location indicates (roughly) the values of the corresponding parameters $(v, \overline{\Delta a}_0)$. All shapes shown with full lines are rotational symmetric bodies with their axes of symmetry in the figure plane as is indicated for one prolate shape. The dashed contour depicts a non-axisymmetric body which has a flat starfish-like shape whose arms are approximately axisymmetric. Non-axisymmetric shapes (the dashed contour shown is only one example) are the minimal energy shapes in the middle part of the phase diagram located in between prolate and oblate shapes for not too large values of v. At large values of the reduced volume, prolate and oblate phases are directly connected via a (weak) first order transition ($\mathrm{D}^{\mathrm{obl}}$). Near the sphere ($v \lesssim 1$), prolate and oblate vesicles are the only stable shapes. For small reduced volume, prolate shapes develop into long tubes (the boundaries of this region are not known), whereas oblate shapes transform into discocytic shapes resembling red blood cells (the further structure of this region is also not known). Both phases, prolates and oblates, have an equatorial symmetry plane, i.e., they are up/down symmetric. This symmetry is broken for large absolute values of $|\overline{\Delta a}_0 - 1|$. As this parameter is increased, prolate shapes become higher in energy than pear shapes at the budding transition ($\mathrm{D}^{\mathrm{pear}}$, $\mathrm{C}^{\mathrm{pear}}$), whereas oblate shapes are eventually replaced by stomatocytes as the lowest energy shapes ($\mathrm{D}^{\mathrm{sto}}$, $\mathrm{C}^{\mathrm{sto}}$). These two symmetry breaking transitions can be either first-order (full lines; $\mathrm{D}^{\mathrm{pear}}$, $\mathrm{D}^{\mathrm{sto}}$) or second-order (dashed lines; $\mathrm{C}^{\mathrm{pear}}$, $\mathrm{C}^{\mathrm{sto}}$). Increasing $|\overline{\Delta a}_0 - 1|$ further leads to shapes where the membrane touches itself. The two limiting lines ($\mathrm{L}^{\mathrm{pear}}$, $\mathrm{L}^{\mathrm{sto}}$) correspond to shapes which are built out of two spheres which sit inside or on top of each other, respectively. Especially, the upper one of these lines ($\mathrm{L}^{\mathrm{pear}}$) represents the limiting line of the budding transition. The limiting lines of the pear and stomatocytic regions have the interesting property that the absolute value of $\overline{\Delta a}_0$ diverges as $v \to 0$. The first order transition lines ($\mathrm{D}^{\mathrm{pear}}$, $\mathrm{D}^{\mathrm{sto}}$) of the prolate and oblate shapes to the pear and stomatocytic shapes, respectively, exhibit the same feature.

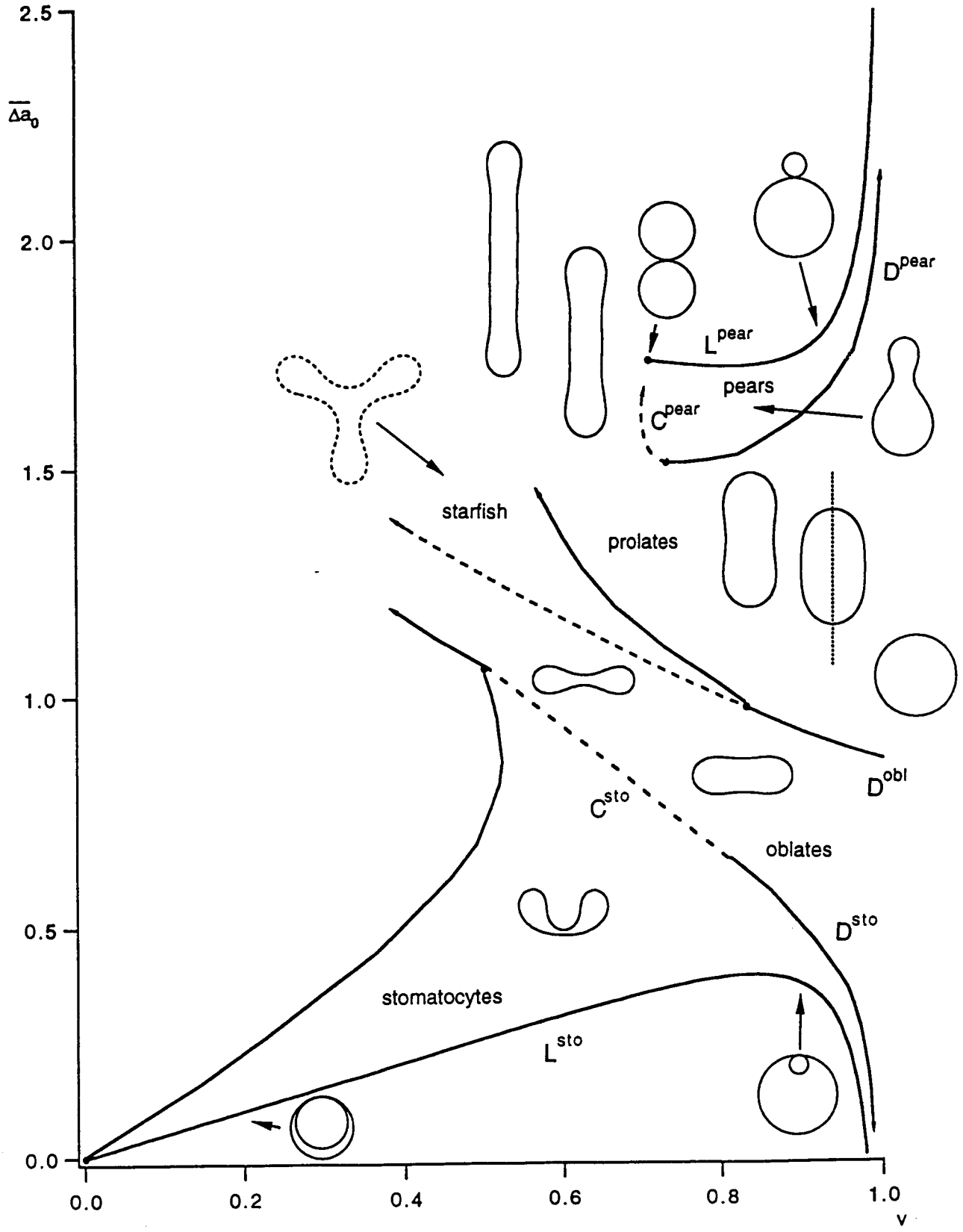
2.5
$\overline{\Delta a_0}$
2.0
1.5
1.0
0.5
0.0
0.0
0.2
0.4
0.6
0.8
1.0
v
D^{pear}
L^{pear}
pears
C^{pear}
starfish
prolates
D^{obl}
C^{sto}
oblates
D^{sto}
stomatocytes
L^{sto}

2.4.3 The ADE Model at $T > 0$

Since experiments are done near room temperature, it is important to understand the effect of nonzero temperature on vesicle shapes. Because the vesicle is a finite system, thermal fluctuations wipe out all sharp phase boundaries, at least, in principle. However, the low-lying energies of this finite system are of order κ, so, as long as $k_BT/\kappa \ll 1$ ($k_BT/\kappa_{\rm SOPC} \simeq 0.04$), there are still recognizable boundaries, although they are in principle fuzzy. Shapes which are near the principal energy minima will continue to dominate the ensemble; but, there are shape fluctuations about the preferred zero-temperature configurations.

Metastability, i.e., the existence of shapes which are locally stable, but do not correspond to the global minimum, will continue to be observable as long as nearby minima are separated by energies significantly larger than k_BT; however, metastable states must in principle have finite lifetimes, since the full stationary ensemble averages over all low-lying regions of phase space. As a consequence, all thermodynamic states have the full Euclidean symmetry of the initial energy functional, and symmetry changes cannot occur.

Does this make the phase-diagram considerations we have outlined above irrelevant to the experiments? The answer, of course, is "no". We shall argue in Chapter 4 that, provided we remain in the low-temperature region, it is possible to infer the ideal zero-temperature behavior from observation of finite-temperature fluctuating contours. Indeed, if fluctuations were unrestricted and Gaussian, then an appropriately defined "mean" of the thermally fluctuating experimental shapes would give the exact zero-temperature shape. The existence of constraints modifies this picture, introducing thermal shifts of the mean shape even at the Gaussian level. In Sec. 6.6, we shall discuss these thermal shifts and estimate their magnitude. It will turn out that normally they are rather small, basically because κ/k_BT is small. On the other hand, in certain regions of the phase diagram, where there are either soft modes or hard constraints, they may become appreciable.

In regions where the thermal corrections are calculable, it is in principle possible to apply thermal corrections to the observed (room-temperature) data and, thus, to infer equivalent zero-temperature shapes. It is these zero-temperature shapes which must be compared with the predicted $T = 0$ phase diagram [see Chapter 6]. In addition, the magnitude of the thermal fluctuations provide important information (for example, nearby soft modes produce large thermal fluctuations), which can also be compared to the predictions of the theory [see Chapter 5].

Chapter 3

Experimental Techniques

3.1 Materials

For all experiments, vesicles were prepared from the common phospholipids 1-Stearoyl-2-Oleoyl-sn-Glycero-3-Phosphatidylcholine (SOPC) or 1,2-Dimyristoyl-sn-Glycero-3-Phosphatidylcholine (DMPC). These lipids have their main phase transition at 5 °C and 23 °C , respectively [5]. They were purchased in powder form (Avanti) and stored dissolved in chloroform:methanol (2:1) in special chemically inert glass vials (Fischer) below -15 °C .

It is desirable in shape experiments to cover a large range of volume-to-area ratios in order to sample widely the shape (phase) diagram. Although the thermal expansion coefficient of lipid membranes is much larger than that of water, [1] one still needs relatively large temperature changes to induce a significant shape change. Thus, one aims for the largest possible temperature interval within which shape experiments on fluid vesicles can be performed. The experimental accessibility is, basically, limited by two factors. First, the vesicles have to be in a fluid phase and, second, the onset of convection makes observation at too high a temperature impossible. [2] In addition, within a range of a few degrees around the main transition temperature, the elastic moduli are strongly temperature dependent [64], so it is wise in shape experiments to stay well away from this region in order to avoid unnecessary complications. The main transition of SOPC is at a lower temperature than that of DMPC, so, for the above reasons, SOPC was used for most measurements.

[1] Typical numbers are $\beta_V(H_2O) \simeq 3 \times 10^{-4}/K$ and $\beta_A(SOPC) \simeq 3 \times 10^{-3}/K$ [10].
[2] Observations at 60 °C are still feasible.

3.2 Preparation of Vesicles

Preparation was done using a standard technique developed in the laboratory of Evan Evans: A few drops (30 μl) of lipid solution (10 mg per ml chloroform:methanol) are spread with a syringe needle on a roughened teflon disk. The solvent is evaporated in a vacuum chamber overnight. The disk with the dried lipid is placed in a glass beaker (50 ml) and pre-hydrated with a stream of Argon saturated with water vapor for about 20 minutes. [3] Then, the desired solution for vesicle swelling is added, and the beaker is covered with parafilm and placed in the oven. To avoid heat shock, the solution and the beaker with the teflon disk are heated separately to the swelling temperature prior to incubation. Swelling was done with 50 mMol sucrose solution at a temperature of 36 °C .

Successful vesicle development is indicated by whitish streaks in the swelling solution. These streaks are collected with cleaned glass pipettes and incubated into Eppendorf tubes at the swelling temperature. Excess glucose solution (48 mMol) is then added to obtain the desired density of vesicles in the observation chamber. The end result of this procedure is a vesicle suspension with an interior sucrose solution and an exterior glucose solution (with a slight admixture of sucrose). The excess density of the interior relative to the exterior sugar solution is approximately 4 g/l. This is needed in order that the vesicles sink gently to the bottom of the experimental cell, as explained in Sec. 3.4.1.

If not otherwise indicated, vesicles were stored at the swelling temperature and used within a few days.

3.3 Cleaning

Cleaning is an important step of the preparation process, since one wants to avoid the accumulation of surface-active impurities and dust particles in the membrane. Beakers and disks are pre-cleaned with laboratory soap and tap water. They are then rinsed extensively in double-distilled water and air dried. Prior to usage, a final cleaning step with chloroform:methanol is performed. Syringes for application of lipid organic solution to the disks are also cleaned before each usage in a two-step process with chloroform:methanol. All aqueous solutions are prepared from double-distilled water and filtered.

[3] It is believed that the pre-hydration step serves to create coherent lipid bilayer "strata" prior to the addition of excess water. This apparently leads to a more gentle vesicle development and more good giant unilamellar vesicles.

3.4 Data Aquisition and Experimental Setup

3.4.1 Overall Procedure

The general setup for observation and data collection is shown in Figure 3.1. Vesicles were incubated in a tightly sealed microchamber and monitored by video phase contrast microscopy. Because of the slightly higher density of the interior sucrose solution with respect to the exterior glucose solution, vesicles sink to the bottom cover glass, thus locating them conveniently for the optical system. In addition, resting (gently) against the floor of the experimental cell effectively restricts angular diffusion. For example, a prolate vesicle will have its principal axis effectively restricted close to a horizontal plane, as shown schematically in Fig. 3.2, thus permitting continuous monitoring of the shape with the "mean" symmetry axis[4] always in or near to the focal plane. This restriction of rotational diffusion will play an important role in the shape analysis of Chapters 5 and 6. Of course, if the density difference is too large, significant gravitational deformations of the free shape may occur. This point is discussed in Sec. (6.6.2).

At this point, the material visible in the microscope focal plane at the bottom of the chamber is typically highly diverse, including topologically complex and multilamellar material, small vesicles included within larger ones, vesicles with visually obvious defects, [5] partial adhesions, etc. In selecting a particular vesicle for detailed observation, we tried to identify a vesicle which was topologically spherical, unilamellar, and free of visible defects. The final percentage of usable vesicles is small – well below one percent. Furthermore, we monitored the fluctuations of each selected vesicle for some time prior to data acquisition. In this way, vesicles with "abnormal" behavior (e.g., those exhibiting sudden changes in excess area or obviously irregular shapes) could be rejected. Therefore, in order to ensure high quality of the data, analysis has been restricted to a small number of vesicles only. In this thesis, we present quantitative results obtained from three different vesicles. The total amount of data gathered consists of over 100 hours of video tape containing information on numerous vesicles. However, the trajectories of most of these vesicles, unfortunately, were not in the (budding) part of the phase diagram which is of interest in this work. In addition, it is an extremely elaborate process to record a high quality budding trajectory consisting of several data points. On the one hand, one has to measure long enough to obtain good

[4]The meaning of the expression "mean symmetry axis" will be discussed in detail in Sec. 4.3.2.

[5]Structures which have length scales below optical resolution or those which, for other reasons, do not result in a diffraction pattern cannot be detected visually, unless for some reason they have a strong effect on the local membrane curvature.

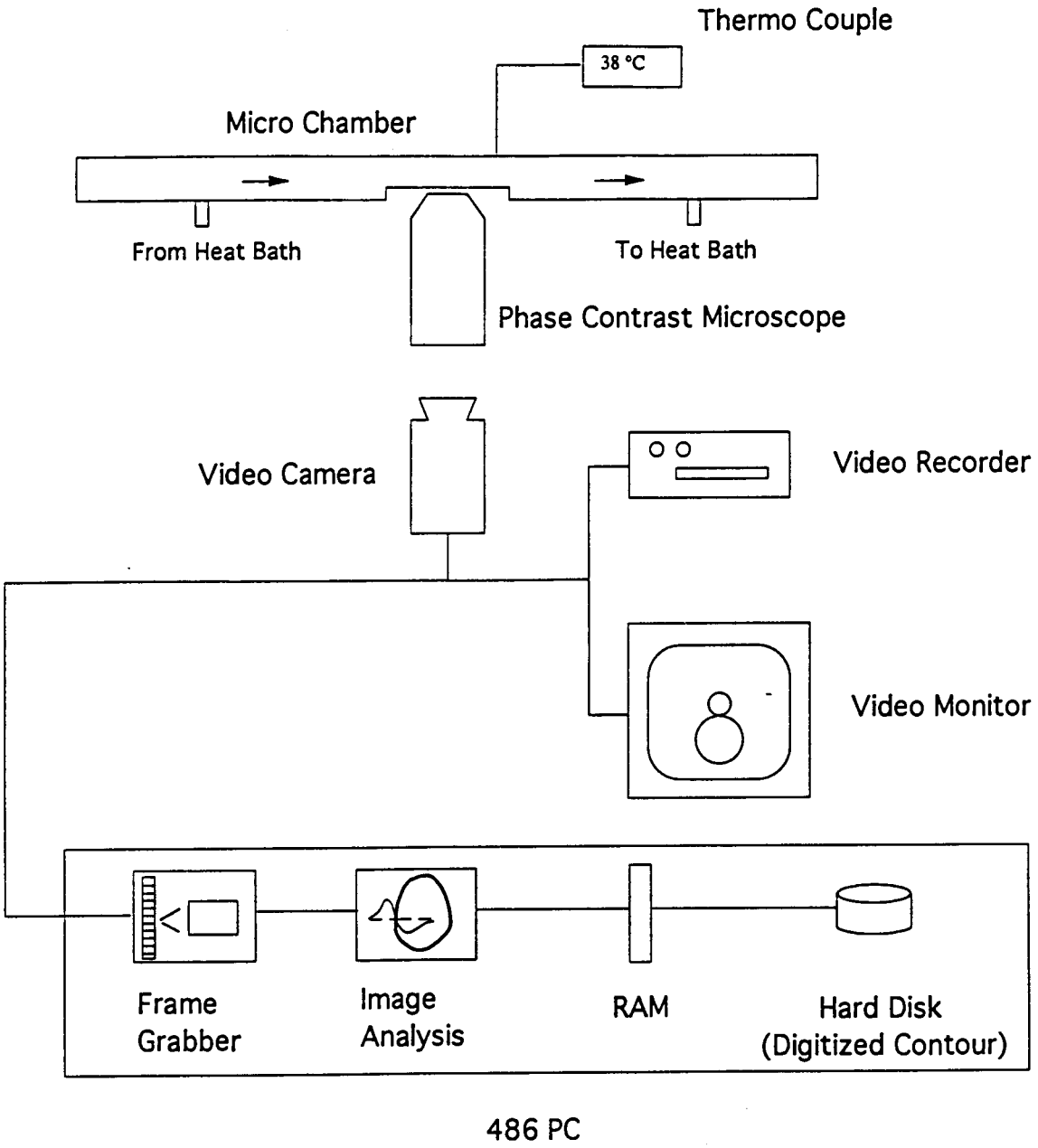

Figure 3.1: Flow Diagram of Experimental Setup. Details of the micro chamber can be found in Fig. (3.3).

statistics for each point. On the other hand, too long a measurement time for the whole trajectory leads to corruption of the data by degradation effects. Out of these reasons, only a small number of vesicles were selected for detailed analysis. However, the qualitative behaviour encountered in those vesicles not selected is consistent with the picture to be presented here.

To sample a "shape trajectory," data must be gathered at several different temperatures. Typically, the recording time for each temperature was about 20 minutes. Water bath temperature was adjusted in order to obtain the desired temperature reading from the thermocouple within the observation chamber. The chamber was allowed to equilibrate for at least 5 minutes after temperature changes. The precision of constant temperature control and temperature determination is ± 0.1 °C . Changing the temperature by 1 Kelvin corresponds to a change in reduced volume v of only 0.004. Thus, temperature is an extremely sensitive control parameter for the reduced volume (compare the typical scale in v of different vesicle phases in Fig. (2.1)).

Time sequences of vesicle contours were recorded by performing image analysis on frames captured (Matrox) from the video camera. Each frame analysis was fully completed before grabbing the next one. Digitized vesicle contours were stored in computer memory and swapped to disk at the end of each sequence. Preliminary analysis was performed after each sequence, and data were checked for consistency. Data aquisition was normally aborted when unusual behaviour was detected. The whole video sequence was backed up to tape (U-Matic, Sony) to allow reobservation after measurements were performed.

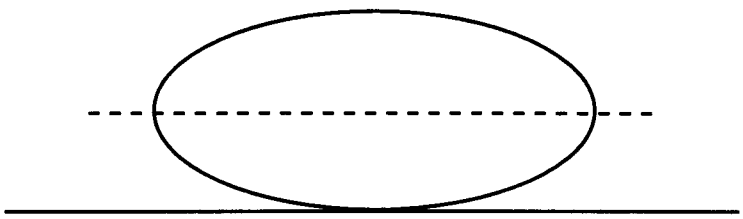

Figure 3.2: A prolate vesicle rests gently under gravity against the floor of the experimental cell, because of a slight density mismatch between interior and exterior sugar solutions. Gravity inhibits excursions of the vesicle's principal symmetry axis away from the horizontal plane. Translational and rotational diffusional motion in which the axis remains horizontal are unrestricted and do, in fact, occur.

3.4.2 Chamber

The special chamber shown in Figure 3.3 was utilized to monitor vesicles at fixed temperature. The steel frame (SF) and the two steel plates (SP) containing the water in- and outlets are built out of stainless steel and mounted on a glass microscope slide (GS). These parts and one cover glass (CG) are permanently glued together with silicone adhesive. Water from the temperature bath flows steadily through the water compartment (WC) and keeps the observation chamber (OC), which is filled with vesicle solution, at the desired temperature. The observation chamber, separated from the water compartment by a thin cover glass (0.17 mm), is cut from a teflon spacer (TS) (0.3 mm) and closed by another cover glass (0.17 mm). The teflon spacer and the cover glasses (Fisher Premium) are held together with vacuum grease (Dow Corning). The temperature is measured with a thermocouple (TC) placed between the two cover glasses. In this way differences between the measured and the actual temperature of the vesicle under investigation are minimized. The sandwich structure (glass-water-glass) of an aqueous solution with a high thermal conduction coefficient between insulating glass plates reduces thermal gradients within the vesicle solution. [6]

Initially, the thin cover glass between the observation chamber and the water compartment resulted in transduction of pressure fluctuations caused by the water pump of the heat bath. This coupling was completely eliminated by routing the water flow through a damping tank.

[6] A simple calculation shows that for such a structure gradients appear almost exclusively within the insulating material. Thus, there are only minor temperature gradients within the vesicle suspension. Gradients are well below the precision of temperature control of ± 0.1 °C . In addition, the measurement is only affected when these gradients change with temperature.

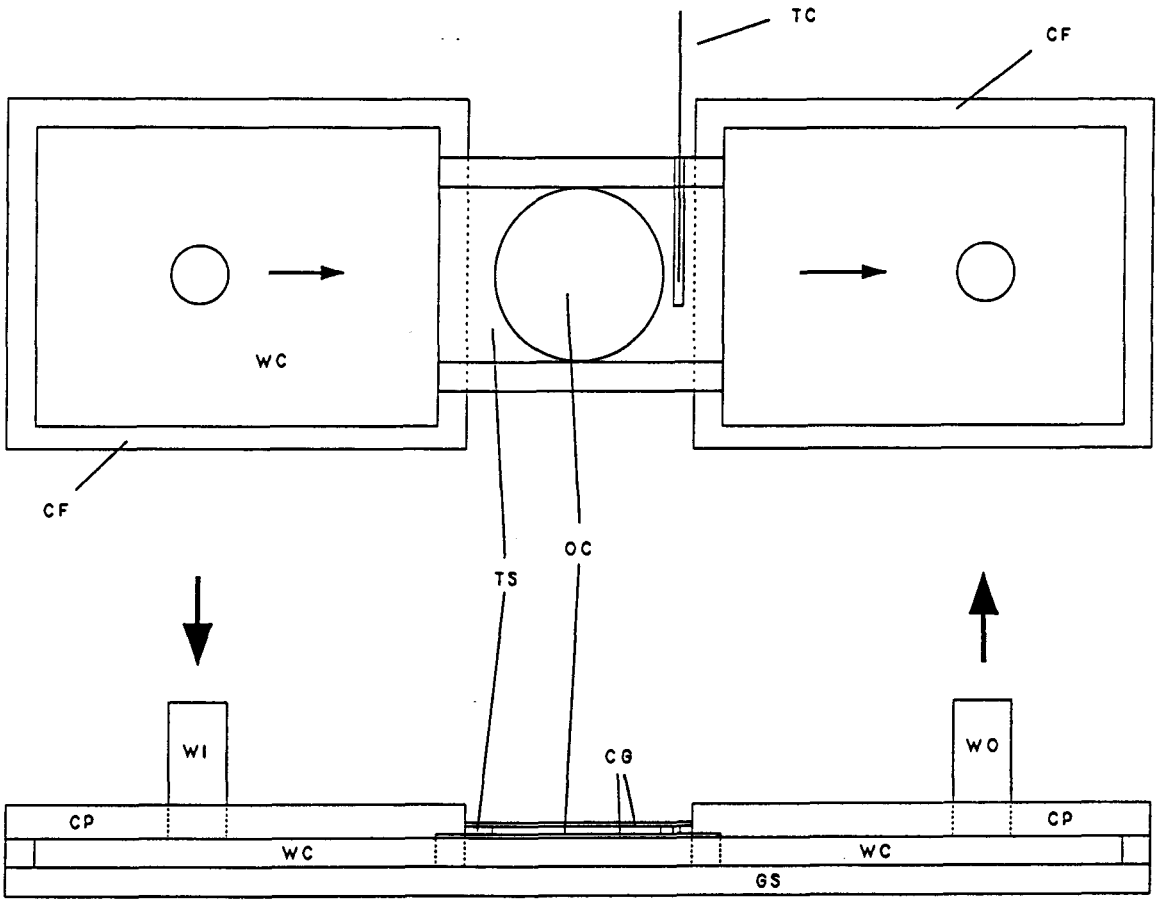

Figure 3.3: Design of observation chamber :
CG cover glasses, GS glass slide, TS teflon spacer, WC water compartment, WI water inlet, WO water outlet, OC observation chamber, CF steel frame, CP steel plates, TC thermocouple.

3.4.3 Video Phase Contrast Microscopy

The optical system used was a standard inverted Leitz microscope equipped with phase contrast [7] capable of an overall magnification of 500 times. The light source was a Hg arclamp powered by an Orion high-voltage transformer. A permanent green filter [8] and various grey filters were used to minimize degradation of the lipids. The video camera was positioned above the eye piece in such a way as to gain a resolution of 86 nm per pixel in a 480×480 frame. A typical picture of a fluctuating vesicle obtained with this setup is shown in Figure 3.4. The distinct halo inherent to the phase contrast technique is clearly visible.

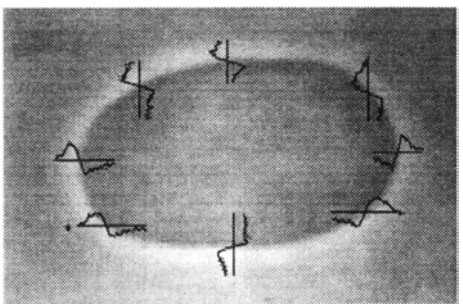

Figure 3.4: Snapshot of a fluctuating vesicle at the bottom of the chamber. The overlay shows several contour profiles plotted with respect to the local background across the membrane. A contour profile is characterized by its width $2n_a$ and the extension of the steep slope $2n_s$.

A typical profile across the vesicle boundary (see Fig. 3.4) exhibits a pronounced maximum and a minimum. These extrema are well separated by a steep slope which falls off towards the vesicle interior. Inspection of Figure 3.4 reveals that, at least to visual accuracy, the slope crosses the local background [9] at its steepest point.

It is necessary to have a protocol for selecting from this halo profile the nominal position of the membrane. We have chosen this to be the crossing point of the slope with the local background, which is identical in practice to the point of maximum slope. It is not clear that this convention corresponds exactly to the position of the membrane; however, there is some theoretical justification for this choice. Wilson and Sheppard [65] calculated the form of the profile expected for a straight-edge object, assuming a circular phase disk [65]. They, indeed, find that the slope of the profile is maximum at the position of the edge. In principle, this calculation should be redone for the specific parameters of our optical system[10] and for

[7] Objective Leitz Phaco 40/0.65, Condenser 0.7/L4.

[8] Corion P10-546 - F-1 340.

[9] The local grey value of the background is obtained by averaging the profile over $2n_a$ pixels.

[10] The phase-contrast system used in this work has the usual annular illumination and a phase ring.

the curved geometry of the typical vesicle contour. This has not been done; however, we anticipate that deviations from the crossing rule are too small to affect our data appreciably.

Another point of concern is the effect of the three-dimensional structure of the vesicle on the two-dimensional image. The "general wisdom" seems to be that what is seen in phase contrast microscopy is a cut through the vesicle in the focal plane [43, 44, 45, 46, 47, 48]. However, this is probably an oversimplification. Phase contrast is particularly sensitive to edges, so that vesicle boundaries which "overhang" the focal plane (relative to the optical axis) may contribute to the image, to a greater or lesser extent depending on the focal depth and the amplitude of the edge contrast. Following the literature, we shall ignore such effects in what follows. We wish only to point out that there is in principal a question which should be addressed in future work.

3.4.4 Contour Algorithm and Time Series

For efficient shape analysis, we have implemented "real-time" digitization of the two-dimensional vesicle-shape contours directly from the grabbed frames coming from the video camera (see Fig. (3.5)). To follow the vesicle dynamics, it is necessary to take relatively small time

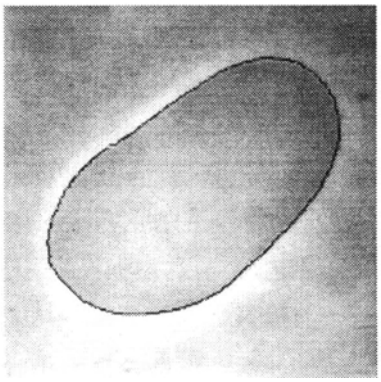

Figure 3.5: Example of a digitized vesicle contour obtained with the algorithm described in the text. Note that the fuzziness of the contour is a result of limited *printing* resolution. In fact, the accuracy with which the contour is determined is better than a pixel.

intervals between frames. On the other hand, to implement the digitization in real time, the interval between grabbed frames must be long enough to allow operation of the contour algorithm.

The algorithm described below needs between 0.4 and 0.6 s to find a contour, [11] depending on vesicle size. This is relatively slow compared to processing times on the order of 0.1 s, which have been reported in the literature [47, 48]. However, in contrast to the fast procedures used elsewhere, our algorithm has a better-than-pixel accuracy in finding the contour. [66, 67] This increased resolution turns out to be critical to the success of our experiments, since the later analysis requires detection of shape changes which are small. At the same time, an interval of 0.6 s between successive contours is sufficiently short to capture the dynamics of the slow fluctuation modes of a typical vesicle, provided that the vesicle radius is not too small. In particular, we are interested in the slow dynamics associated with the approach to the spinodal line of the budding transition, where, as we will see later, the relevant time scales are well above one second. Thus, we did not optimize our algorithm for speed.

Once the vesicle profile is located at a particular point, the algorithm must extract the membrane position at that point and then proceed sequentially to follow the membrane around until the contour closes. This is a local procedure. The program must then take the next grabbed frame and find a starting point for the next contour. This step is nonlocal, both because the vesicle may have moved appreciably (on the scale of pixels) between one timeframe and the next and/or because the target vesicle has gone temporarily out of focus or has been obscured by another (typically smaller) vesicle drifting nearby. The next few paragraphs discuss how our implementation solves these problems.

As discussed in the preceding Section, a vesicle-edge contour, as observed by phase contrast microscopy, is quite well approximated as a line orthogonal to the steepest gradient along the halo. To find this line, one should in principle determine the direction of steepest descent by probing the gray-scale values of the video pixels in a two-dimensional region around the point of interest. However, such a procedure is very time consuming and not practical, if one wants to obtain reasonable sampling times. Instead, we have adopted a simplified procedure, described in the following paragraphs, in which gradients are taken only along the x- or y-directions:

The search is always started on the left side of a vesicle, and it proceeds initially in the positive y-direction. We label the pixel grid by integers (n_x, n_y). For each vesicle the first point in the initial frame of a sequence is found by selecting a whole video line n_y, utilizing a cursor which is overlayed on the video picture. The profile $g(x)$ of this line is then searched for the pixel position n_x where the slope m_x is maximally negative, as averaged

[11] Thus, for a video frequency of 30 frame/s, we are processing only every 15th frame. In this sense, we perform only a "dilute" real-time image analysis.

over $2n_s+1$ pixels. The vesicle contour (x,y) (measured in pixel units) thus passes near the point $x=n_x, y=n_y$. We may refine this estimate, however, by interpolation of the x value between the integer pixel coordinates. To do this, we first determine a local background level $\bar{g}_x$ by averaging over the $2n_a+1$ nearby points, according to

$$\bar{g}_x = \frac{1}{2n_a+1}\sum_{n=-n_a}^{n_a} g(n_x+n). \tag{3.1}$$

We then determine a smoothed linear approximation $\bar{g}(x)=xm_x+t_x$ to $g(x)$ in the vicinity of $x=n_x$ by making a linear least-square fit over an interval extending n_s pixels to the left and right of n_x,

$$m_x = \frac{< x >< g(x) > - < xg(x) >}{< x >^2 - < x^2 >} \tag{3.2}$$

$$t_x = \frac{< g(x) >< x^2 > - < x >< xg(x) >}{< x >^2 - < x^2 >}, \tag{3.3}$$

where $< >$ denotes the average over $2n_s+1$ pixels. Solving for the intersection, $\bar{g}(x)=\bar{g}_x$, locates our estimate for the contour edge position at (x,n_y), where

$$x = \frac{1}{m_x}(\bar{g}_x - t_x). \tag{3.4}$$

In this way, we obtain a resolution which is better than the one defined by the pixel grid. Of course, noise limits the accuracy which can be obtained. This is discussed in Sec. (4.1.1).

Once the first contour point (x,y) is found, the y-coordinate of the next point is set to $y=n_y+1$ and the procedure to determine the next x-coordinate is repeated, where now n_x is set to the integer part of the previous "exact" x-coordinate.

This repetition eventually would run into problems at the north pole of the vesicle, where there is no gradient along the x-axis, and the direction of the contour search along the y-axis would have to be reversed. Practically, the advancement along the y-axis breaks down much earlier, since on average the slope along the x-axis becomes smaller (and, thus, the intersection, less well defined) the closer one is to the north pole or to any other local turning point of the contour. The search routine must, therefore, be generalized to handle these events: For each point (x,y) of the contour, the slopes m_x and m_y are calculated. If m_y has been larger than m_x for n_{switch} times, the search mode is switched and the next x-coordinate is found by setting $x=n_x+d_x$, where $d_x=\pm 1$, depending on the average direction of the contour along the x-axis over the last $n_{average}$ pixels. Then, n_y is set to the integer part of the previous y-coordinate, and the next y-coordinate is calculated to be

$$y = \frac{1}{m_y}(\bar{g}_y - t_y), \tag{3.5}$$

n_s	n_a	n_{switch}	$n_{average}$
5	15	10	5

Table 3.1: Parameters used in the contour search algorithm described in the text.

where $\bar{g}_y$, m_y, and t_y are given by replacing x with y in Eqs. (3.1) - (3.3). Similarly, if m_x has been larger than m_y for n_{switch} times, the next point is determined by $y = n_y + d_y$ and Eq. (3.4). Again, $d_y = \pm 1$, depending now on the average direction of the contour along the y-axis over the last $n_{average}$ pixels.

Since the contour is calculated from a still picture by Eqs. (3.4) and (3.5), it closes in on itself exactly. The contour search for one particular frame is stopped when the last point found is within one pixel of the contour starting point.

The search parameters which have been used are collected in Table 3.1. Choosing the parameter n_{switch} appreciably greater than unity ensures that the search direction is not needlessly switched back and forth many times in regions where the difference $m_x - m_y$ fluctuates near zero. For a simple convex contour with four turning points the search direction is switched exactly four times. Choosing the parameter n_{average} greater than unity but not too large allows for an unlimited number of turning points, as may occur for a general two–dimensional closed curve. [12]

Finally, the search loop is completed by defining the starting point for the contour search for the next grabbed frame. To do this, the final y-value determines the first video line for the next frame. This line is scanned for the starting point of the next contour within an interval around the previous mean x-value by determining the pixel value n_x of the most negative slope of the profile. This restricted global search allows for centering the vesicle on the screen and readjusting focus without stopping the contour search. Likewise, the presence of a few additional vesicles in the field of view does not disrupt the time series.

Every once and a while, the search algorithm fails and loses the contour. Most of these events can be identified by monitoring the contour length and the distance between subsequent points on the contour. Such points are discarded, and the next available video frame is grabbed for analysis.

By this protocol, a time series of two-dimensional vesicle contours is obtained. In the next Chapter, we discuss the procedures developed to analyze these data.

[12] For instance, a dumbbell shape has 8 turing points.

Chapter 4

Shape Reconstruction

This Chapter describes how we parameterize the individual digitized two-dimensional shape contours discussed in Sec. 4.1, how we average the shape parameters over a data set which provides a thermal ensemble for the room-temperature vesicle, and how we extract information about the average shape of the three-dimensional vesicle. Sec. 4.2 is devoted to the discussion of a typical data set for a vesicle of prolate shape and is intended to motivate the general procedure of shape reconstruction outlined in Sec. 4.3.

4.1 Characterization of 2D-Contours

4.1.1 Contour Smoothing and Resolution

Experimental contours appear "noisy" and must be smoothed before shape parameters can be extracted. The noise reflects a combination of causes, including the intrinsic noise of the original optical signal, the statistics of the pixelation, the digitization of the grey scale, and other factors. In addition, there is a systematic effect coming from the video electronics: Alternate video lines are scanned in each $\frac{1}{60}$ s interval, so that an entire video frame takes $\frac{1}{30}$ s to update and consists of two superposed images, taken $\frac{1}{60}$ s apart. If the vesicle were stationary in this interval, there would be no effect; but, vesicle motion at a characteristic speed of, say, 1 $\mu m/s$ will produce an offset of about 20 nm, which, as we shall see, is clearly visible at our estimated resolution of roughly 30 nm. Smoothing corrects for these effects.

The smoothing was done, separately in the x and y coordinates, using a binomial filter

of width $2n = 20$. Implementation of this procedure involves the replacement, [1]

$$x_i \rightarrow \frac{1}{4}(x_{i-1} + 2x_i + x_{i+1}) , \tag{4.1}$$

$$y_i \rightarrow \frac{1}{4}(y_{i-1} + 2y_i + y_{i+1}) , \tag{4.2}$$

which is repeated n times, thus resulting in an effective averaging of width $\sqrt{2n} \simeq 4.5$ pixels. This smoothing window corresponds to a contour segment which is smaller than 0.5 μm (4.5 x 86 nm $\simeq$ 390 nm). The choice, $n = 10$, removes spurious spikes in the contour and defines a proper physical contour length. At the same time, n is small enough not appreciably to affect the vesicle shape on the large length scales which are of interest in this thesis. Figure 4.1 shows an example of typical data smoothed by this algorithm.

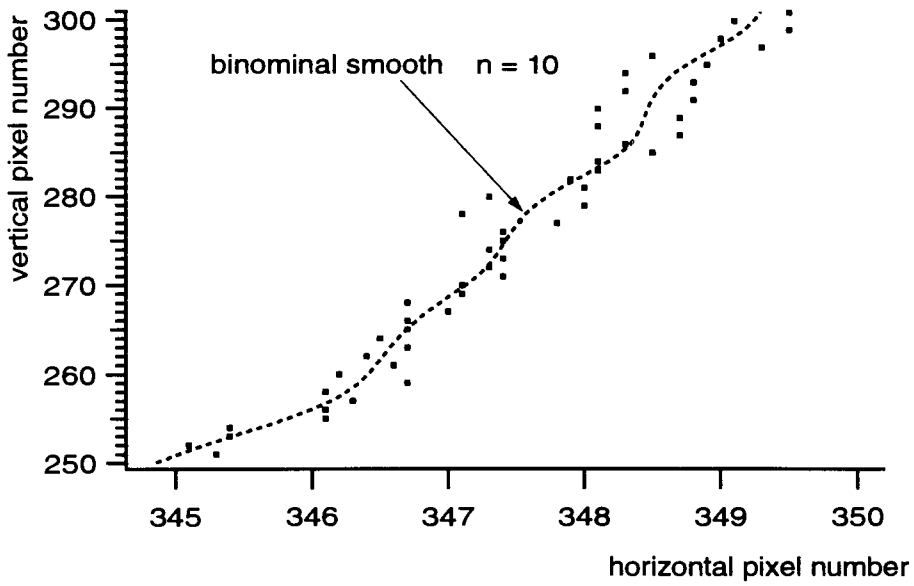

Figure 4.1: Typical contour data (points) along with the curve (dashed) generated by binomial smoothing, as described in the text. Note the difference in the horizontal and vertical scales. In this example, the vertical data is integer. The tendency of the data points to alternate systematically to the left and right of the smoothed curve reflects the composite property of the video image, as noted in the first paragraph of this Section.

An estimate of the lateral resolution can be obtained from an analysis of the scatter of individual contour points. A histogram of the deviations from the smoothed contour is given in Fig. 4.2. As can be read off from the mean square deviation, the local lateral

[1] The contour coordinates (Sec. 3.4.4) are always integers in either x or y. Note that the binomial algorithm has no effect on the integer coordinate.

resolution is about 30 nm. This resolution, well below the nominal optical resolution given by the wavelength of light, is a result of the delicate line-shape discrimination achievable via phase contrast. Note that the typical magnitude of a large scale vesicle motion is one micron. Thus, different vesicle configurations can be well discriminated.

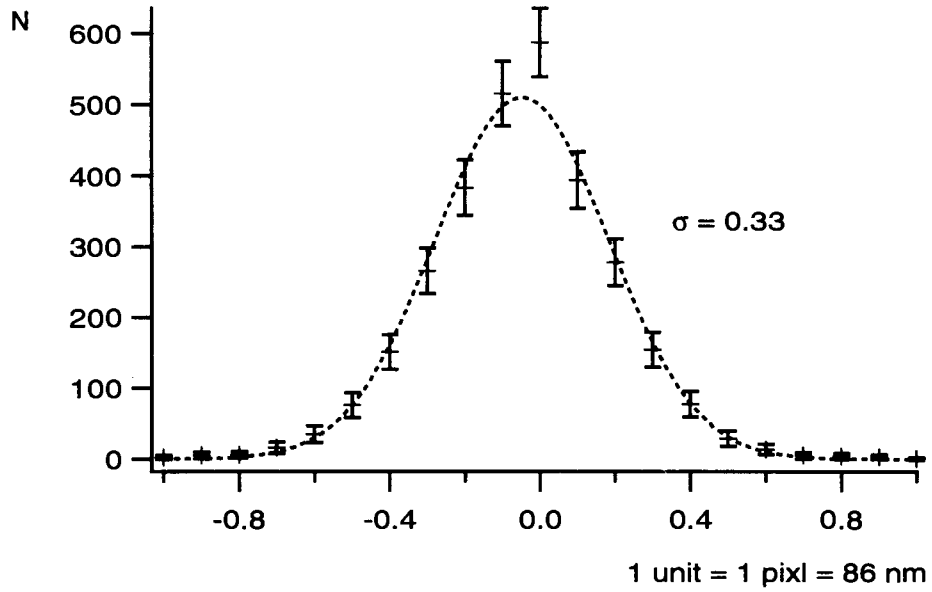

Figure 4.2: Cumulative histogram of contour scatter in x or y direction over 5 consecutive frames. The total number of points is 3016. The error bars give the uncertainty in counting events. The dashed line shows a least square fit to a Gaussian distribution. The rms deviation σ of data points from the mean contour position provides an estimate of the resolution.

We turn now to the issue of shape parameterization, i.e., how efficiently to parameterize the contour shapes.

4.1.2 Extraction of Principal Axis

To start, it is necessary to establish a frame of reference. A convenient choice is to place the origin at the "center of mass" of the contour (i.e., the point which would be the center of mass if the contour were a uniformly weighted line) and then to align the x and y axes along the long and short axes, respectively, of the corresponding inertial ellipse. We shall discuss further the logic of this choice in Sec. 4.3.2. For now, we restrict attention to the implementation, only.

Because of the square pixel grid, the density of points varies along the contour. Since

each length element of the contour should enter with the same weight in a calculation of the center of "mass" and the "inertia" tensor, we define the weight,

$$w_i = \frac{\sqrt{(x_{i+1} - x_i)^2 + (y_{i+1} - y_i)^2}}{\frac{1}{N}\sum_{j=1}^{N} \sqrt{(x_{j+1} - x_j)^2 + (y_{j+1} - y_j)^2}}, \tag{4.3}$$

where N is the number of contour points and the point $N + 1$ is identified with the first point. For the remainder of the paragraph we drop the summation indices whenever sums run over all contour points. If the center of "mass,"

$$x_m = \sum w_i \, x_i \tag{4.4}$$

$$y_m = \sum w_i \, y_i, \tag{4.5}$$

is taken as the origin (with orientation still arbitrary), then the inertia tensor is

$$I = \begin{pmatrix} \sum w_i \, x_i^2 & -\sum w_i \, x_i y_i \\ -\sum w_i \, x_i y_i & \sum w_i \, y_i^2 \end{pmatrix}. \tag{4.6}$$

The principle axes of the inertia tensor follow from the eigenvectors of I. In particular, the slopes of the two axes are given by

$$k_{\pm} = -\frac{b}{2} \pm \frac{1}{2}\sqrt{b^2 + 4}, \tag{4.7}$$

where

$$b = \frac{\sum w_i \, (x_i^2 - y_i^2)}{\sum w_i \, x_i y_i}. \tag{4.8}$$

Note that the long axis of the inertial ellipse corresponds to the smaller moment of inertia. The angle that this long axis makes with the (vertical) y axis is given [2] by

$$\alpha = \begin{cases} \arctan k_- & \text{if } \sum w_i x_i y_i > 0 \\ 0 & \vdots \quad = 0 \\ \arctan k_+ & \vdots \quad < 0, \end{cases} \tag{4.9}$$

up to multiples of π. The initial orientation of the vesicle defines an angle $|\alpha(0)| < \pi/2$ at time $t = 0$. The angle $\alpha(t)$ is then followed beyond $\pm\pi/2$ in order to preserve the orientation of up/down asymmetric shapes.

In further analysis, we shall assume that the Cartesian axes have been chosen in such a way that the y axis points along the long axis of the inertial ellipse, i.e., that the contour has been rotated by $-\alpha$.

[2] The sign of $\sum wxy$ can be used as a case label. Let x', y' denote the contour coordinates in the principal axes system. The sign of $\sum wxy = \sin\alpha\cos\alpha(\sum w'x'^2 - \sum w'y'^2)$ is opposite to the sign of α for an axisymmetric prolate oriented along the y' axis.

4.1.3 Mode Expansion

It is convenient to be able to characterize each contour by a small number of parameters. We do this by expanding the contour in terms of a set of shape modes, whose amplitudes become the required parameters. We shall assume for simplicity that the shapes we are treating are approximately axisymmetric and that it is the y axis which corresponds to the (approximate) symmetry axis. [3]

The y axis typically divides the contour into two inequivalent halves. We choose to describe the two halves separately, each one in an angle (ψ) versus arclength (s) representation, as shown in Fig. 4.3,

$$\psi(s) = \pi\frac{s}{s^*} + \sum_{n=1}^{\infty} a_n \sin(n\pi\frac{s}{s^*}) + \sum_{n=0}^{\infty} b_n \cos(n\pi\frac{s}{s^*}) \ . \tag{4.10}$$

Let s^* denote the overall arclength between the north pole ($s = 0$) and the south pole ($s = s^*$). It is convenient to employ a trigonometric representation, for each half contour. The first (linear) term describes a half circle. Nonzero coefficients a_n and b_n describe deviations from the circle. Contours which intersect the y axis at the poles at right angles obey $\psi(0) = 0$ and $\psi(s^*) = \pi$, and have $b_n = 0$ for all n. Note that all axisymmetric shapes fall into this class.

Our experiments are conducted mainly in regions of the phase diagram where the average or mean shape is axisymmetric. (Of course, at nonzero temperature thermal fluctuations about the mean result in nonaxisymmetric shapes.) Thus, in dealing with mean shapes, we may set $b_n = 0$ for all n. Furthermore, for these axisymmetric mean shapes, the representation (4.10) distinguishes efficiently between shapes (like the "prolates" of Fig. 4.4) which are up/down symmetric and those (like the "pears" in Fig. 4.4) which are not. For up/down symmetric shapes, $a_{2n+1} = 0$ for all n.

We note as an aside that a shape described by Eq. (4.10) with arbitrary coefficients does not in general close, i.e., does not achieve radius $x = 0$ from the symmetry axis at $s = s^*$. By noting that

$$\frac{dx}{ds} = \sin\psi(s) \ , \tag{4.11}$$

it is easy to show that the condition for closure is

$$x(s^*) = \int_0^{s^*} ds \ \sin\psi(s) = 0 \ , \tag{4.12}$$

which places a complicated nonlinear condition on the coefficients a_n and b_n. In practice, of course, the data originate in closed contours, so this condition is always satisfied.

[3] In practice we shall analyze mainly prolate ellipsoidal and pear shapes.

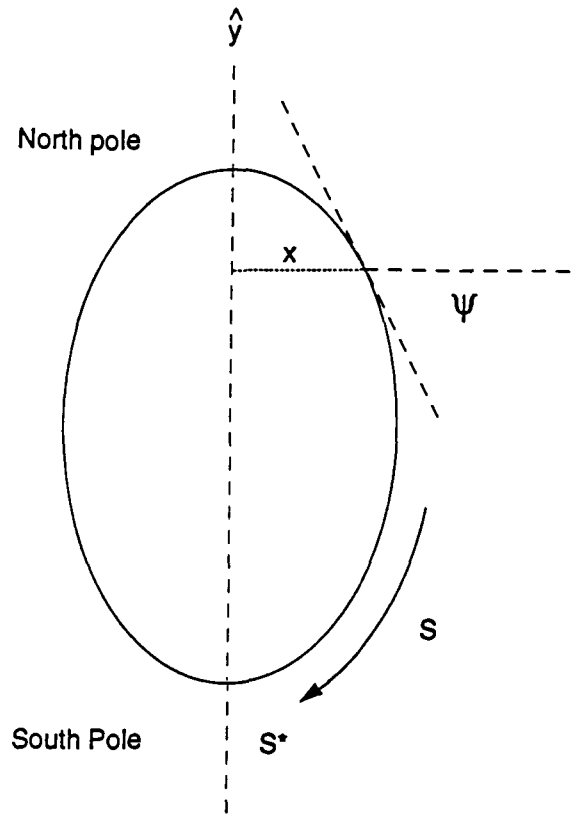

Figure 4.3: The contour is characterized by the tangent angle ψ as a function of arclength s.

The contour amplitudes a_n are given by an inversion of Eq. (4.10). The tangent angle at each contour point is taken to be

$$\psi_i = -\arctan\left(\frac{y_{i+1} - y_{i-1}}{x_{i+1} - x_{i-1}}\right), \tag{4.13}$$

where the arctangent is defined on its Riemann surface, i.e., $\psi(s)$ is continuous at the equator. The amplitudes are then obtained by a numerical integration using the trapezoidal rule

$$a_n = (-1)^n \frac{2}{n} + \sum_{i=1}^{M} \left(\psi_i \sin\left(n\pi \frac{s_i}{s^*}\right) + \psi_{i+1} \sin\left(n\pi \frac{s_{i+1}}{s^*}\right) \right) \frac{s_{i+1} - s_i}{s^*}, \tag{4.14}$$

where s_i is the arclength measured from the north pole to the contour point (x_i, y_i). The summation is over the M points of the half contour. [4]

[4]The first and last point need a special treatment. The integration interval is only taken up to the y axis. The tangent angle at these points is determined by using one point beyond the y axis.

Figure 4.4: Examples of a prolate and a pear shape.

4.1.4 Effective Area and Volume

It will prove useful to define an effective area and volume, A_e and V_e, as the volume and area of the shape generated by rotating each half contour about its y axis, i.e.,

$$A_e = \pi \sum_{i=1}^{M} (x_i + x_{i+1})(s_{i+1} - s_i) \tag{4.15}$$

and

$$V_e = -\frac{\pi}{2} \sum_{i=1}^{M} (x_i^2 + x_{i+1}^2)(y_{i+1} - y_i). \tag{4.16}$$

In a similar spirit, we introduce an effective reduced volume,

$$v_e = \frac{V_e}{\frac{4\pi}{3}(\frac{A_e}{4\pi})^{\frac{3}{2}}} . \tag{4.17}$$

If the original shape is axisymmetric, as would be true at $T = 0$ in the axisymmetric regions of the phase diagram, then these quantities are, respectively, the true, physical area and volume and the corresponding reduced volume. Generally, at $T > 0$, they are all constructs based on a particular half-contour; and, they fluctuate over time, even though the true A, V, and v are invariant. However, when thermal fluctuations are small , these effective quantities never deviate very much from their physical counterparts. One might hope in this situation that, by averaging the fluctuating quantities, one could obtain a good approximation to the physical ones. This is, indeed, how we shall in practice infer physical parameters from the data. One might naively imagine that, in a regime where the fluctuations are still Gaussian, average parameters correspond exactly to their zero-temperature counterparts. Unfortunately, this is not the case, because the presence of

constraints forces thermal shifts even at the Gaussian level. Nevertheless, by using the theory, it is in principle possible to correct for these shifts and to extract effective zero-temperature values.

Before we discuss these issues further, it will be instructive to look at some experimental data in the next section.

4.2 A Typical Data Set

In this section, we present a representative set of shape data. Typical histograms of the amplitudes of the first few Fourier modes (Eq. (4.14)) and of the effective reduced volume (Eq. (4.17)) are shown for a prolate vesicle in Fig. 4.5. As long as the reduced volume is sufficiently smaller then unity, the probability distributions are Gaussian within experimental error. The mean values,

$$< X > = \frac{1}{N} \sum_{i=1}^{N} X_i \, , \tag{4.18}$$

and the standard deviations,

$$\sigma_X = \sqrt{\frac{1}{N} \sum_{i=1}^{N} (X_i - < X >)^2} \, , \tag{4.19}$$

are collected in Table 4.1. The estimated Gaussian errors ($N = 1378$) of the mean values,

$$E(< X >) = \sigma_X \left(\frac{1}{N} \right)^{\frac{1}{2}} , \tag{4.20}$$

are also given. Differences between the data sets of the left and right half-contour are on the order of the statistical errors. One observes that $< a_2 >$ is much larger than $< a_3 >$

X	$< X > \pm E(< X >)$	σ_X
v_e	0.9538 ± 0.0002	0.0089
a_1	0.0002 ± 0.0002	0.0059
a_2	0.2974 ± 0.0008	0.028
a_3	-0.0020 ± 0.0013	0.047
a_4	-0.0039 ± 0.0012	0.043

Table 4.1: Statistics of observables shown in Fig. 4.5.

and $< a_4 >$. This is the generic situation for a prolate vesicle not too far from the sphere, as we will briefly discuss in the following few paragraphs.

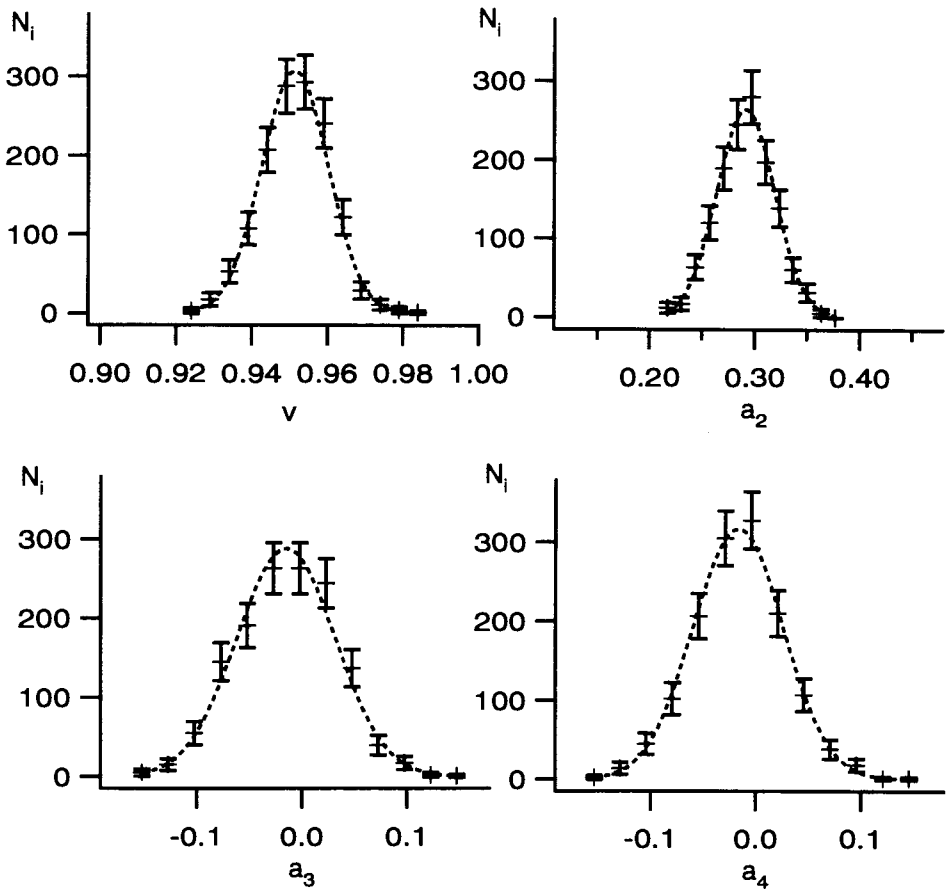

Figure 4.5: Gaussian distributions (dashed lines) as obtained from estimates of the mean values (Eq. (4.18)) and standard deviations (Eq. (4.19)). The error bar of histogram bin i is given by $2/\sqrt{N_i}$.

The observation that, for vesicles with reduced volume v near unity, the mean amplitude of the fourth mode is distinctively smaller than the mean amplitude of the second mode is physically reasonable and expected theoretically on the basis of the ADE model. Since a vesicle assumes that shape which minimizes the bending energy of its membrane, the "best" shape will have large contributions from modes with few "ripples." Together with the geometrical constraints on area and volume, this requirement of minimal bending energy leads, correspondingly, in the ADE model to a hierarchy in the shape amplitudes. In Appendix A, this result, which was first noted by Ling Miao [57, 58], is reviewed in the context of an expansion of vesicle shape in spherical harmonics about the sphere. By relating our parameterization Eq. (4.10) to the spherical harmonic representation, we show in Appendix A that

$$\begin{aligned} a_2 &\sim O(\,(1-v)^{\frac{1}{2}}\,)\,, \\ a_4 &\sim O(\,(1-v)^{1}\,)\,, \\ &\text{etc.}\,, \end{aligned} \tag{4.21}$$

in accordance with our experimental results. This observation is an important result of this Thesis work. Being aware of the hierarchy is crucial for comparison of theoretical with experimental shapes. We will investigate it further in Chap. 6, where we use $< a_4 >$ to map experimental mean shapes into the ADE phase diagram. [5]

As a result of the hierarchy, the numerical values of the mean amplitudes $< a_n >$ for mode numbers $n > 4$ and reduced volume $v > 0.8$ are too small to be measured.

The amplitudes of the odd modes should average to zero for an up/down symmetric prolate vesicle. However, $< a_3 >$ has, typically, always a small – but statistically significant – nonzero value. We will come back to this point in Sec. 5.4.2. The mean amplitude $\langle a_1 \rangle$ is an even smaller quantity, which cannot be distinguished from zero within experimental error. In fact, we don't need to know its value for further analysis. Theoretically, it has to be nonzero whenever there is a nonzero $< a_3 >$ amplitude to ensure closure of the contour. [6]

In the past three paragraphs, we have pointed out some properties of the mean amplitudes. We turn now to a short discussion of the amplitude fluctuations.

The mean-square fluctuations, $\langle (a_n - \langle a_n \rangle)^2 \rangle = {\sigma^2}_{a_n}$, measure the typical departure of the measured amplitudes from their mean. If departures are distributed in a Gaussian manner, then the error $E({\sigma^2}_{a_n})$ in calculating the mean-square fluctuation from N observations

[5] Although $\langle a_2 \rangle$ is much larger than $\langle a_4 \rangle$ it cannot be used for this mapping, since $\langle a_2 \rangle$ is independent of the effective area difference $\overline{\Delta a_0}$ at least to order $(1-v)^{\frac{1}{2}}$ (see Appendix A).

is given by

$$E(\sigma^2_{a_n}) \;=\; \sigma^2_{a_n}\,\left(\frac{2}{N}\right)^{\frac{1}{2}}. \tag{4.22}$$

Thus, the relative error in calculating $\sigma^2{}_{a_n}$ is, typically, of order ($\sqrt{2/1378} \simeq 0.038$), i.e., about 4 %. The dominant fluctuations are, presumably, thermal in origin. When thermal fluctuations are small, their contribution to the mean-square amplitudes go as k_BT/κ [68]. In principal, the bending modulus κ can be determined by analyzing the thermal fluctuation spectrum [42]; however, we will not perform such an analysis in this thesis. Nevertheless, we will use the mean-square amplitudes in Chap. 5 to characterize the approach of a vesicle to the budding transition.

The probability distribution of the second mode differs markedly from all other distributions, see Table 4.1. Whereas the mean amplitude $\langle a_2 \rangle$ is an order of magnitude *larger* than the half-width σ_{a_2} of its distribution, this feature is reversed for higher mode numbers. For the third and fourth mode the mean amplitudes are an order of magnitude *smaller* than the half-widths of their distributions. It requires a careful (statistical) analysis to reliably extract these small mean values from the data. Once the mean shape amplitudes are found, one has to deduce zero-temperature information from the room-temperature data in order to compare experiment with existing theoretical predictions. We will turn now to this central issue of shape reconstruction.

4.3 Estimating the Average 3D Shape at T=0 from 2D Contours with Thermal Fluctuations

4.3.1 General Approach

The quantitative output of the shape experiments is an ensemble of data sets for the thermally fluctuating quantities v_e and $\{a_n\}$ for each particular vesicle at each temperature T. Using this data, we may form ensemble averages like $\langle a_n \rangle$ and $\langle v_e \rangle$ or correlations like the $\langle a_m a_n \rangle$ and so forth, where the brackets indicate an average over the data sets of the thermal ensemble. The set of these correlation functions (including their higher-order analogs) encodes a full description of the experimental data.

This set of ensemble averages, which we shall denote $\langle \Pi a_n \rangle$, does not, in fact, provide a complete description of the physical shape ensemble. The reason for this is that all the experimental two-dimensional contours contain (at least, approximately,) the symmetry axis, (see Sec. 4.3.2) and, thus, cannot give information about the fluctuations in the

azimuthal coordinate. More formally, we can imagine describing a general shape in terms of a spherical-harmonic expansion about the sphere [7] with amplitudes $u_{l,m}$. In this representation the thermal shape observables are the set of ensemble averages $\langle \Pi u_{l,m} \rangle$. There is a well defined (nonlinear) relation expressing $a_n(\{u_{l,m}\})$ (see Appendix A for $m = 0$), so it is straightforward to express the a_n correlation functions in terms of the $u_{l,m}$ correlation functions. A simple counting argument shows that the converse is not generally possible.

The key point with respect to shape reconstruction is that, for the region of the phase diagram which we shall explore in detail, the mean three-dimensional shape is expected to be axisymmetric, even though each instantaneous shape – subject, as it is, to thermal fluctuations – is not. Thus, all planar cuts through the vesicle which include the symmetry axis are equivalent in the sense that averaging the instantaneous *two-dimensional* contour amplitudes $\{a_n\}$ (see Eq. (4.14)) obtained from a particular cut gives the full information about the mean *three-dimensional* shape at temperature T.

To make contact with the shape phase diagram, which is defined only at $T = 0$, it is necessary to infer the $T = 0$ shape parameters, $a_n^{(0)} = \langle a_n \rangle (T = 0)$, from the measured room-temperature shape ensemble. This can only be done in the context of theory, which can link $T = 0$ to nonzero temperatures. In principle, the procedure would involve searching for a set of input variables (A, V, ΔA_0, etc.,) which reproduce all the measured room-temperature correlations and, then, calculating the corresponding zero-temperature shape. In practice, the problem is considerably simplified by the fact that κ/k_BT is small at room temperature, so that thermal fluctuations are generally small and can often be treated at the Gaussian level. When this is possible, thermal shifts $\langle a_n \rangle - a_n^{(0)}$ and thermal fluctuations $\langle (a_m - \langle a_m \rangle)(a_n - \langle a_n \rangle) \rangle$ are both of order k_BT and calculable from the theory [68]. Since these corrections are small, one can imagine carrying out a program of successive approximations: At zeroth order, one approximates $a_n^{(0)}$ by $\langle a_n \rangle (T)$. One then uses theory to infer from these (approximate) zero-temperature shape parameters the (theoretical) control parameters v and $\overline{\Delta a_0}$. Using these variables as input, the theory [68] then predicts the expected thermal shifts, $(\langle a_n(T) \rangle - a_n^{(0)})$. These shifts are then used to correct measured parameters $\langle a_n \rangle (T)$, i.e., to provide a new estimate of the zero-temperature shape parameters $a_n^{(0)}$, and, so on. This procedure may be expected to be consistent (and convergent), whenever the thermal corrections are small. In practice, there are difficulties near shape instabilities, where soft modes make corrections large, and for nearly spherical shapes, where a large number of modes contribute to the thermal corrections. The latter

[7] This expansion is restricted to shapes without "overhangs." This is a technical issue, which is not relevant to the discussion here.

points will be further discussed in Sec. 6.6 in connection with the mapping of experimental shapes into the phase diagram.

We shall implement this program mainly at the zeroth-order level, i.e., neglecting (small) thermal corrections. Nevertheless, we shall at several points see the effects of thermal corrections, and it will be reassuring to find that they are of the expected magnitude.

In the next two Sections, we will investigate in more detail some of the issues just introduced. First, we discuss our definition of the reference system given in Sec. 4.1.2. And, second, we will investigate the effect of thermal corrections on the measurement of the reduced volume.

4.3.2 Defining the Right Reference Frame

A natural reference frame for the representation of instantaneous contours would be the mean symmetry axis of the corresponding vesicle. Thermal averages of contour amplitudes should be performed with respect to this axis. However, the averaging procedure, although straightforward in principle, is complicated by the fluctuations of this axis. Ideally, this mean axis would remain horizontal (so as always to lie in the focal plane of the microscope) and fixed in direction under thermal fluctuations (so as to make analysis easy). In practice, neither idealization is strictly true. The axis of a rigid axisymmetric vesicle undergoes thermal fluctuations both (a) away from the horizontal and (b) in the horizontal plane.

Consider first point (a): For "prolate" and "pear" shapes (which we shall concentrate on) the same gravitational effect used to make the vesicles sit at the bottom of the experimental cell (see Sec. 3.4.1) serves to keep the symmetry axis close to the horizontal plane, since it is this orientation which lowers the center of mass of the vesicle as much as possible. Of course, there is also a trade-off here, since increasing the density difference to improve alignment risks producing gravitational shape distortions which would make comparison with the theory (which ignores such effects) difficult. However, we believe that, under the experimental conditions, the axis may be regarded as horizontal and the gravitationally induced shape distortions are small enough to ignore at this level of precision, at least for the analysis of vesicle fluctuations. This picture will be further discussed in Sec. 6.6.2.

Even in the absence of out-of-plane fluctuations, the in-plane fluctuations (b) still present a problem. The point is that the coefficients of the contour shape (see Eq. (4.14)) depend on the choice of axis. What is needed to compare with the zero-temperature coefficients is an average which keeps the mean axis fixed while averaging over thermal shape fluctuations. To do this it is necessary to disentangle the rotational diffusion of the mean axis from the

thermal shape fluctuations. We discuss this issue further in Appendix B, where we argue that the principal axis of the contour is a natural estimate of the mean symmetry axis of the shape. Further, we find that the systematic error which one makes when using the principal axis instead of the mean symmetry axis to expand the contour is within the statistical uncertainty of the data. Thus, in subsequent analysis, we use the instantaneous amplitudes $\{a_n\}$ with respect to the principal axes without further corrections. The procedure to extract the principal axis has already been implemented in Sec. 4.1.2.

4.3.3 Thermal Effects on the Measurement of the Reduced Volume

In this Section, we discuss the measurement of the mean effective reduced volume $\langle v_e \rangle$, defined in Eq. 4.17, and we investigate its relation to the real reduced volume v of the vesicle. The discussion focuses on the case of a prolate vesicle with reduced volume near unity, which will be important in the analysis of Chapters 5 and 6.

We start by expanding the effective reduced volume, which is a function of the contour amplitudes, around the sphere,

$$v_e = 1 - \sum_{n,m>1}^{\infty} V_{nm} a_n a_m + O(a^3), \tag{4.23}$$

where (V_{nm}) is positive definite [8] and the amplitude of the first mode has been eliminated by using the closure condition Eq. (4.12). We now rewrite each of the contour amplitudes as the sum of its mean value $< a_n >$ and a fluctuation,

$$a_n = \langle a_n \rangle + \delta a_n, \tag{4.24}$$

and take the average on both sides of Eq. (4.23). We have seen experimentally in Sec. 4.2 that there is a hierarchy in the numerical values of the mean amplitudes (see Appendix A for a theoretical argument). Thus, to first order, we may set all mean amplitudes to zero, except the amplitude of the second mode. We find

$$\langle v_e \rangle = 1 - V_{22} \langle a_2 \rangle^2 - \sum_{n,m>1}^{\infty} V_{nm} \langle \delta a_n \delta a_m \rangle + O(\ (1-v)^{\frac{3}{2}}\ ). \tag{4.25}$$

We now define the reduced volume of a shape which is constructed from the mean amplitudes,

$$\overline{v_e} \equiv v_e\left(\{\langle a_n \rangle\}\right). \tag{4.26}$$

[8] The eigenvalues of (V_{nm}) are positive as a consequence of the fact that the sphere is the geometrical object which has the smallest possible area for a given volume.

To leading order in $(1-v)$, the first two terms of Eq. (4.25) are just equal to those of $\overline{v_e}$, so we have

$$\langle v_e \rangle = \overline{v_e} - \sum_{n,m>1}^{\infty} V_{nm} \langle \delta a_n \delta a_m \rangle + O(\ (1-v)^{\frac{3}{2}}\ ). \tag{4.27}$$

Since (V_{nm}) is positive definite, it follows that, for $v \simeq 1$,

$$\langle v_e \rangle < \overline{v_e}\ . \tag{4.28}$$

Thus, the mean value of the effective reduced volume $\langle v_e \rangle$ is always smaller than the reduced volume of the shape $\overline{v_e}$ constructed from the mean amplitudes.

At $T = 0$, when no thermal fluctuations are present, $v = \overline{v_e}$. For $T > 0$ there are thermal shifts in the mean amplitudes, so v and $\overline{v_e}$ are inequivalent. We give now an intuitive argument which shows that

$$v < \overline{v_e}\ . \tag{4.29}$$

At zero temperature,

$$v = \overline{v_e} = 1 - V_{22} \langle a_2 \rangle^2 + O(\ (1-v)^{\frac{3}{2}}\ )\ , \tag{4.30}$$

so $\langle a_2 \rangle$ is effectively determined entirely by the reduced volume v (assuming, as always, that $(1-v)$ is small). Now, at a finite temperature, all amplitudes are thermally excited, as the vesicle needs excess area to fluctuate. Therefore, the $\overline{v_e}$ is increased with respect to v, i.e., the vesicle assumes a more spherical mean shape. This, in turn, implies that $\langle a_2 \rangle < a_2^{(0)}$.

To summarize, there are three different "reduced volumes". First, there is the (constant) reduced volume v of the vesicle. Second, we can calculate the reduced volume $\overline{v_e}$ of the "mean shape" from the mean amplitudes. And, third, direct evaluation of the vesicle contours gives the mean value of the effective reduced volume $\langle v_e \rangle$. These three parameters are in general not equal. Only at zero temperature do their numerical values coincide. In Fig. (4.6), a typical thermal trajectory of $\langle v_e \rangle$ versus $\langle a_2 \rangle$ is compared with a plot of $\overline{v_e} = 1 - V_{22} \langle a_2 \rangle^2$. Note that $\langle v_e \rangle < \overline{v_e}$, as expected.

Unfortunately, the numerical value of $v - \langle v_e \rangle$ is not so easily accessible. In fact, even the sign is not obvious and depends on the relative magnitude of thermal amplitude shifts $\langle a_n \rangle - a_n^{(0)}$ and the mean-square amplitudes $\langle \delta a_n \delta a_m \rangle$. However, since both observables are of the same (linear) order in $k_B T/\kappa$ [68], one expects that the difference $v - \langle v_e \rangle$ is of the same order of magnitude as $\overline{v_e} - \langle v_e \rangle$, or even smaller. From Fig. (4.6), we can read off that $\overline{v_e} - \langle v_e \rangle \approx 0.004$, independent of v. In further analysis, we will, thus, set $v = \langle v_e \rangle$. The absolute error we make in doing so is relatively small. Furthermore, since $v - \langle v_e \rangle$ is approximately constant, the relative error $v(T_1) - v(T_2)$ between successive measurements

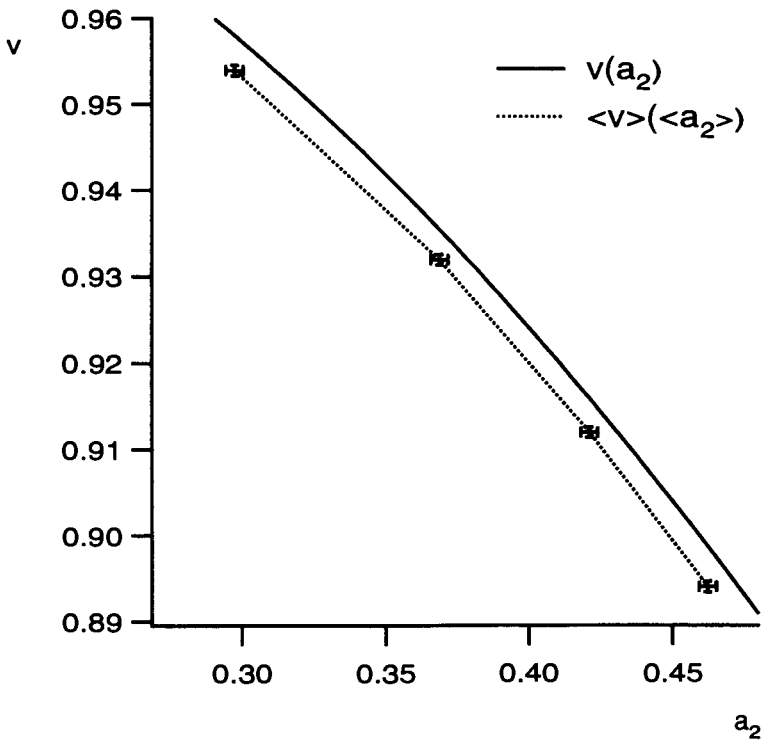

Figure 4.6: Experimental and theoretical relationship of the (effective) reduced volume $v_{(e)}$ and the amplitude of the second mode a_2. Due to thermal shape fluctuations, the effective reduced volume $\langle v_e \rangle (\langle a_2 \rangle)$ is located always below the reduced volume $\overline{v_e} = 1 - \frac{64}{135} \langle a_2 \rangle^2$ of the mean shape. The error bars represent the $3 - \sigma$ intervals for $\langle v_e \rangle$ and $\langle a_2 \rangle$.

of the reduced volume at different temperatures, T_1, T_2, seems to be almost negligible. This observation is especially important for the scaling analysis we will perform in Chap. 5.

Chapter 5

Shape Fluctuations near the Budding Transition

In this Chapter, we report observations of shape fluctuations near the budding transition. In Sec. 5.1, the relevant part of the ADE phase diagram will be recalled. Generically, the budding transition can be either first or second-order in the ADE model. From an estimate of the elastic parameters, one expects the budding transition to be first-order for SOPC/DMPC vesicles in the $1 - 10$ μm size range. In either case, the up/down symmetry of the prolate vesicle phase is broken at the transition. This scenario is rather general, and we will develop a Landau theory for both cases in Sec. 5.2. In Sec. 5.3, experimental results on the statics and dynamics of vesicle fluctuations near the budding transition will be presented. We will focus on the behaviour of the amplitude a_3 of third shape mode which plays the role of an order parameter for the budding transition. In Sec 5.4.1, we will discuss our experimental findings within the framework of the proposed Landau theories. We conclude from a comparison of our data with the theoretical predictions of the two Landau-theory variants that the budding transition is, indeed, first-order. In the first-order budding picture, the prolate phase remains locally stable beyond the point at which the thermodynamically stable state becomes pear shaped. In this metastable region there are two locally stable shapes, one prolate and one pear. The prolate finally becomes unstable at a "spinodal" boundary, and the system transforms irreversibly to a budded shape. We will assemble evidence favoring this first-order budding scenario. In Sec. 5.4.2, we point out that, for reasons not understood, real laboratory vesicles exhibit a weak asymmetry in the prolate phase which breaks the up/down symmetry expected from the ADE model. This extrinsic asymmetry gets magnified near the spinodal line and complicates interpretation of the data.

However, we will show that the effect is quite small and does not alter appreciably vesicle shapes calculated within the ADE model, except very close to the spinodal instability. In Sec. 5.4.3, we discuss previous experiments on the budding transition in the context of our results.

5.1 The Budding Transition in the ADE Phase Diagram

We will discuss in the following the ADE phase diagram in the region near the budding transition [57, 58, 69]. Fig. (5.1) shows this region of the calculated phase diagram of the ADE model at $\alpha = 1.4$ [58], the approximate value for SOPC [61, 58]. The behavior is typical for values of α near unity, although, of course, the locations of all boundaries do vary smoothly with the material parameter α. The horizontal axis gives the reduced volume v; the vertical axis measures the tendency of the vesicles to curve, as described by the effective area difference $\overline{\Delta a_0}$. The part of the phase diagram which we are interested in has, basically, four regions or shape classes. Ordered from smaller to larger values of $\overline{\Delta a_0}$, these are: the oblates (including discocytes), the prolates (including dumbbells), the pears (open necks), and the fully vesiculated shapes, in which the neck between the parent and the bud shrinks to microscopic dimensions. The prolate phase includes up/down symmetric axisymmetric shapes, including both elliptical shapes (at larger v) and dumbbells (at smaller v). It is thermodynamically stable in the region between boundaries C^{pear}, D^{pear} with the pear phase and the boundary D^{obl} with the oblate phase. (Note that the line D^{obl} is not shown in Fig. (5.1). It is located very close to M^{obl} at slightly larger values of $\overline{\Delta a_0}$).) The lines M^{pear} and M^{obl} are spinodal lines , which mark the limits of local stability of the prolate shapes. Between D^{pear} and M^{pear} and, again, between D^{obl} and M^{obl}, prolate shapes remain locally stable, even though they are no longer the global minimum-energy shapes. Pear shapes lack up/down symmetry and become more and more necked as one moves away from the prolate boundary. The limiting line L^{pear} denotes the limit of the pear phase at which the radius of the neck between the parent and the bud becomes microscopic. All shapes on this limiting line are double spheres. The radius of the bud is equal to that of the parent at the point E; it decreases at larger v and approaches zero as $v \to 1$. The form $v_L(\overline{\Delta a_0})$ of the limiting line L^{pear} is given in parametric form by [57]

$$\begin{aligned} v_L &= 1 - \tfrac{3}{2}(\Delta a - 1)^2 - \tfrac{1}{2}(\Delta a - 1)^3, \\ \overline{\Delta a_0} &= \Delta a + \frac{1}{\pi\alpha}\frac{\Delta a}{(\Delta a^2 - 1).} \end{aligned} \tag{5.1}$$

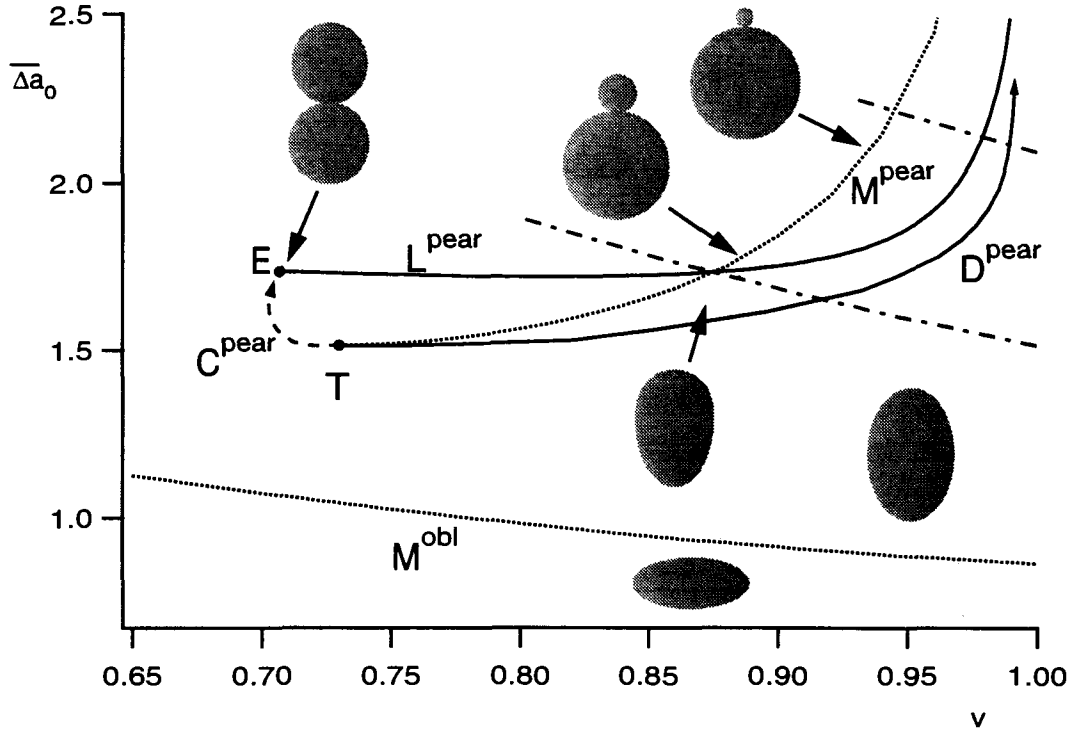

Figure 5.1: Region of the budding transition of the ADE phase diagram for $\alpha = 1.4$. Two common experimental trajectories are depicted by the dashed lines. The vesicles start in the quasi-spherical region and gradually become more prolate as the reduced volume is decreased. Then, at the line D^{pear}, the trajectories cross the first-order transition to the pear phase. However, due to the energy barrier between the (then) meta-stable prolate state and the pear state, the vesicles stay prolate until they become unstable near the spinodal line M^{pear} to fully vesiculated shapes. (The meta-stable prolate state decays when the energy barrier is on the order of thermal energies.) The neck is fully closed at the instability when the spinodal line M^{pear} is located above the limiting L^{pear} which is the locus of two-sphere-shapes with gradually smaller radius of the bud. For a full discussion of the phase diagram and other possible trajectories, see the text.

Note that the lines L^{pear} and M^{pear} intersect, so that metastable prolates with reduced volume $v > 0.87$ which become unstable at the spinodal line M^{pear} may be expected to end up as fully vesiculated shapes.

The ADE model has a tricritical point T. To the left of this special point, along the line C^{pear}, the transition between prolate and pear shapes is second-order, i.e., a vesicle changes shape smoothly and continuously from a dumbbell to a pear. To the right of T, along the line D^{pear}, the transition between prolates and pears is first-order, i.e., the bud is expelled abruptly, and the shape changes discontinuously. The location of the tricritical point $(v^*, \overline{\Delta a_0^*})$ depends on the value of α. As $\alpha \to 0$, the point T moves toward the end point E $(\sqrt{2}/2 \simeq 0.71, \sqrt{2}(4\pi + 4/\alpha))$ of the limiting line, where the shape consists of two equal spheres. This limit has not been studied in detail, but already for $\alpha = 1.4$ one has $v^* = 0.73$. It is clear that for this and smaller values of α the thermodynamic transition between prolates and pears is first-order for $v > 0.73$. Note that estimated values for phospholipids are in this regime ($\alpha_{DMPC} \approx 1.1$, $\alpha_{SOPC} \approx 1.4$ [61, 58]). For $\alpha \to \infty$, the tricritical point moves to the point (1,1). Thus, all budding transitions are continuous for large α, except for very small buds. One recovers, therefore, the predictions of the SC-model ($\alpha = 0$, first-order budding) and of the ΔA-model ($\alpha = \infty$, second-order budding).

Heating the vesicle sample leads to thermal trajectories $(v(T), \overline{\Delta a_0}(T))$ in this phase diagram. Two generic budding trajectories are shown in Fig. 5.1. The general functional dependence of a thermal trajectory will be discussed later in Chapter 6. For now, we consider only the simplest case, for which (see Sec. 6.4),

$$\overline{\Delta a_0}(T) = \frac{\Delta a_0^s}{v(T)}, \tag{5.2}$$

where the effective differential area $\overline{\Delta a_0}$ becomes a hyperbolic function of the reduced volume v. [1] The horizontal position of the different trajectories is parameterized by the value, $\Delta a_0^s \equiv \Delta a_0(v = 1)$ of the area difference at the *sphere*. [2] Thus, a vesicle with a sufficiently large Δa_0^s will eventually cross one of the two transition lines, (C^{pear} or D^{pear}), when heated. Depending on the location of the tricritical point T, it will do so either on the left of T, across the line C^{pear}, or on the right, across the line D^{pear}.

The second-order line C^{pear} is, in fact, only accessible from the prolate phase for a very narrow range of trajectories, with $\Delta a_0^s \lesssim 1.11$. On these trajectories, full budding (i.e., approach to L^{pear}) is never achieved, since the vesicle recrosses C^{pear} almost immediately,

[1] This formula is valid for zero spontaneous curvature and equal thermal expansivities of the two monolayers.

[2] Note that the superscript "s" refers to "sphere" not to "spinodal".

reentering the prolate phase.

For $\Delta a_0^s > 1.11$, all thermal trajectories cross the first-order line D^{pear}. Provided that $\Delta a_0^s > 1.23$, all these trajectories do eventually reach the limiting line L^{pear}. [3] It does not, however, follow that the observed budding will occur at D^{pear}. The reason for this is that the prolate state remains metastable beyond D^{pear}, all the way to M^{pear}. Thus, in the absence of external perturbations, a prolate vesicle will remain metastable in the prolate phase, when it is heated beyond D^{pear}, until the energy barrier for transition out of that state becomes comparable to $k_B T$, at which point the prolate state decays via a thermal fluctuation over the barrier and into a lower-energy budded state. This instability occurs near the spinodal line M^{pear} (see Fig. 5.1), where the energy barrier goes to zero. The loss of stability of the prolates at M^{pear} corresponds to the vanishing of an eigenvalue of the second-variation matrix,

$$\mathrm{Det}\left(\frac{\partial^2 \mathrm{E}_{\mathrm{pro}}(v, \overline{\Delta a_0}; \{a_i\})}{\partial a_n \partial a_m}\right) \equiv 0 \ , \tag{5.3}$$

where the $\{a_i\}$ are the amplitudes (e.g., in the shape representation Eq. (4.10)) corresponding to the prolate shape with parameters $(v, \overline{\Delta a_0})$. This provides a definition of the spinodal locus M^{pear}. Note that, to the left of the tricritical point T, the spinodal M^{pear} merges with the regular second-order transition C^{pear}.

An important feature of the phase diagram is the crossing of the spinodal line M^{pear} with the limiting line L^{pear} at the point ML with coordinates $(v_{ML}, \overline{\Delta a}_{ML})$. [4] This crossing means that for a reduced volume $v > v_{ML}$ the metastable prolate phase extends beyond L^{pear}. Therefore, thermal trajectories which cross L^{pear} at $v > v_{ML}$ miss the pear phase entirely, and the neck of the budded shapes closes completely at the instability. This happens for trajectories with $\overline{\Delta a_0} > 1.52$. [5]

5.2 Two Landau Theories of Budding

In the budding transition the up/down symmetry of the prolate state is broken along some path in the general shape space. To be specific, one might think of the shape representation Eq. (4.10). This symmetry breaking corresponds to a deviation from zero of the mean

[3] In the small parameter regime $1.11 < \Delta a_0^s < 1.23$, the vesicle follows a reentrant trajectory where the prolate phase is left across the line D^{pear} and subsequently reentered across the line C^{pear} [49]. In practice, the two different kinds of reentrant trajectories will be hardly distinguishable.

[4] The position of this point is also dependent on α. For $\alpha \to \infty$, ML moves to $(1, 1)$.

[5] We note that the regions in $\overline{\Delta a_0}$ for the different budding scenarios are dependent on α. They have been given above for $\alpha = 1.4$.

amplitudes of the odd modes, as explained in Sec. (4.1.3). Near the spinodal instability of the metastable prolate state, the local minimum of the bending energy functional is characterized by a second variation which is small in one direction of shape space and which eventually disappears at the instability line M^{pro}. Fluctuations in this shallow minimum become more pronounced, as the instability is approached. At the same time, the restoring forces diminish, and it takes increasingly long for fluctuations to decay ("spinodal slowing down"). This "softening" of the fluctuations will actually be divergent for the symmetry breaking normal mode with the lowest energy. One might use the amplitude of this soft mode as an order parameter for the (spinodal) budding transition. We shall find experimentally in Sec. 5.3 that the soft mode has a large component along the direction of the shape mode a_3 of our expansion Eq. (4.10).

We have seen in the last Section that the budding transition can be first or second-order. For either of these situations, one can develop a Landau theory, which quite generally captures the situation just described. [6] We will do so now.

5.2.1 First-Order Budding

Let us begin by assuming a first-order budding transition, as suggested by the ADE model and estimates of the elastic parameters. In the following, we are not interested in the first-order transition itself, but rather in the behaviour of the vesicle near the spinodal line. If a_u denotes the amplitude of the dominant unstable (odd) mode, the potential in this a_u direction can be modeled [7] as

$$V(a_u) = \kappa[\tau a_u^2/2 - g a_u^4/4 + u a_u^6/6] \,, \tag{5.4}$$

where $g, u > 0$ and τ is proportional to the second derivative of the bending energy at the metastable minimum, which changes sign at the instability. Note that the bending energy κ sets the overall energy scale, so that the Landau coefficients τ, g, and u are dimensionless and generically of order unity. We denote the spinodal reduced volume as v_s and the corresponding spinodal temperature as T_s. [8] We expect

$$\tau \approx c_0(v - v_s) \approx c_1(T_s - T)/T_s. \tag{5.5}$$

[6] The following Section is based in large parts on notes by Dr. Udo Seifert [72].

[7] The last term of the potential is added only for reasons of stability. It is not important for the following discussion. For simplicity, we assume $\tau u \ll g^2$.

[8] It is important to note that the spinodal volume and the spinodal temperature, at which the prolate phase becomes unstable, have no absolute meaning. They are defined relative to a given thermal trajectory. Note that the budding transition here is *not* a thermodynamic phase transition but, rather, an instability. Temperature is only used as a control parameter to dial the reduced volume.

The constants c_0 and c_1 (not to be confused with curvatures) are generically of order unity. In principle, c_0 could be calculated from a diagonalization of the second variations of the bending-energy functional. The second linear relationship follows from the assumption of a constant thermal area expansion coefficient [9] β_A.

When $\tau \geq 0$, the potential (5.4) has a local minimum at $a_u = 0$, which is metastable when u is small. Under these circumstances, the metastable state is constrained by an energy barrier centered near $a_u^+ \equiv \pm\sqrt{\tau/g}$ of height approximately $V(a_u^+) = \kappa\tau^2/4g$. The mean-square amplitude $\langle a_u^2 \rangle$ of fluctuations about the metastable minimum is given at the Gaussian level by equipartition as

$$\left\langle a_u^2 \right\rangle = \frac{k_B T}{\kappa\tau} \approx \frac{1}{c_0}\frac{k_B T}{\kappa}(v - v_s)^{\zeta_s}. \tag{5.6}$$

We thus find that the static equal-time fluctuations diverge as v approaches the spinodal point v_s with an exponent [10] $\zeta_s = -1$.

We turn now to the dynamics of the soft mode. The simplest assumption is that near the instability the amplitude a_u of the soft-mode obeys a dynamical equation of the form [70],

$$\dot{a}_u = -\Gamma\frac{\partial V}{\partial a_u} \approx -\Gamma V''(a_u = 0)a_u \approx -\Gamma\kappa\tau a_u, \tag{5.7}$$

which will be further justified below. The kinetic coefficient Γ has the dimensions of $1/(time \times energy)$. Since friction is determined by the viscosity η of the surrounding liquid and the only lengthscale available is the "wave-length" of the unstable mode, i.e, the size R of the vesicle, dimensional analysis leads to

$$\Gamma = c_2/(\eta R^3), \tag{5.8}$$

with a numerical factor c_2 (generically of order unity) which could in principle be determined by a more careful (non-trivial!) analysis of the dynamical eigenmodes. Note that the dynamical eigenmodes do not coincide in general with static ones: The static normal modes are coupled dynamically, a feature which is neglected in Eq. (5.7). Nevertheless, we can gain support for the reasoning just given by reference [70] to the relaxation equation for the amplitude of a planar membrane with wave-vector q, which reads (for $q \to 0$)

$$\dot{a}_q = -\frac{1}{4\eta q}\,(\kappa q^4)\, a_q\ . \tag{5.9}$$

[9] One finds $c_1 = \frac{3}{2}\beta_A v_s T_s\, c_0$.

[10] Note that ζ_s is not a critical exponent in the strict thermodynamic sense but rather a "spinodal" exponent. Indeed, the "divergence" suggested by Eq.(5.6) cannot, in fact, be reached for $T > 0$, since the metastable state decays before the instability, as soon as the barrier is comparable to $k_B T$.

Thus, for long wavelengths $q \sim 1/R$, this is the same as (5.7) with (5.8). This equation holds for the relaxation of an unstructured incompressible membrane and neglects the dissipation caused by inter-monolayer friction. [11]

An estimate of the full time-dependent correlation function can be easily derived from Eq. (5.7):

$$\langle a_u(t)a_u(0)\rangle = \left\langle a_u^2 \right\rangle e^{-t/t_c} , \tag{5.10}$$

where the equilibrium fluctuations $\langle a_u^2 \rangle$ are given by (5.6) and the correlation time t_c is defined by

$$t_c \equiv 1/(\Gamma\kappa\tau) . \tag{5.11}$$

Inserting τ from Eq. (5.5), we find that the correlation time diverges on approach to the spinodal with a dynamical exponent ζ_d,

$$t_c = \frac{1}{c_0 c_2} \frac{\eta R^3}{\kappa} (v - v_s)^{\zeta_d}, \tag{5.12}$$

which has, in fact, the same numerical value as the static exponent ($\zeta_d = \zeta_s = -1$). Thus, the relaxation time of the soft mode is expected to grow near the spinodal in the same way as the mean-square amplitude. For the typical values, $\eta = 10^{-2} erg\ sec/cm^3, R = 10^{-3} cm$, and $\kappa = 10^{-12} erg$, one finds

$$t_c \approx \frac{1}{c_0 c_2} 10 \frac{1}{v - v_s}\ sec . \tag{5.13}$$

One has to keep in mind that in deriving the relations (5.6) and (5.12) one makes the implicit assumption that the metastable state is not yet decaying thermally. However, the prolate vesicle cannot approach the instability closely without being subject to thermal decay over the barrier into the budded state. Thus, the "spinodal exponents," ζ, which describe the divergent behaviour near the spinodal, are not well defined thermodynamic quantities but should, rather, be viewed as an effective way of describing the properties of the fluctuation spectrum of the vesicle near but not at the spinodal.

The (finite) mean lifetime t_l of the metastable prolate state can be estimated as

$$t_l = t_c \exp(V(a_u^+)/k_B T), \tag{5.14}$$

where the exponential factor reflects the static probability of a thermal excitation sufficient to overcome the energy barrier and $1/t_c$ plays the role of an attempt frequency. Far away

[11] A full analysis [70] which takes into account the bilayer structure and allows for monolayer compressibility shows that there is a crossover of the slowest mode from a regime dominated by dissipation due to hydrodynamic viscosity to a regime where dissipation within the bilayer dominates. This crossover takes place on a length scale of about 1 μm. The bilayer aspect is irrelevant as long as the shape changes happen on a scale larger than that. This should be the case, at least for the onset of the budding transition.

from the (spinodal) instability the two time scales t_c and t_l are well separated. This is the region where (5.6) and (5.12) apply. The two timescales become comparable when $V(a_u^+) \simeq k_B T$, i.e., for $\tau \simeq 2\sqrt{g(k_B T/\kappa)}$. [12]

For this and smaller values of τ, the definitions of the spinodal exponents ζ become fuzzy, since thermal averages of the metastable state are no longer well defined. Nevertheless, using this estimate for τ in the definition (5.11) of t_c, we obtain

$$t_c = \frac{1}{c_2 2 g^{1/2}} \frac{\eta R^3}{(\kappa k_B T)^{1/2}} \approx \frac{1}{c_2 2 g^{1/2}} 50 \text{ sec} \tag{5.15}$$

as a typical timescale of the soft mode near the spinodal. This is much larger than the timescale (see Eq. (5.13)) away from the spinodal. Indeed, that is what we will find in experiments.

5.2.2 Second-Order Budding

For large α or small reduced volume v at budding, the budding transition becomes continuous. In this case, there is no metastable state and no spinodal. Within a Landau picture, the potential near the transition may now be approximated by

$$V(a_u) = \kappa[\tau a_u^2/2 + g a_u^4/4] \, . \tag{5.16}$$

The relations,

$$\tau \approx c_0(v - v_c) \approx c_1(T_c - T)/T_c \tag{5.17}$$

and

$$V''(a_u = 0) = \kappa\tau \, , \tag{5.18}$$

still hold (with the spinodal subscript s now replaced by c for "critical"). Therefore, the fluctuations (in the Gaussian regime) of the symmetric shape behave the same way as a function of τ for first and second-order transitions, provided one is still *above* v_c (i.e., below T_c). In particular, the mean-square amplitude,

$$\left\langle a_u^2 \right\rangle = \frac{k_B T}{\kappa\tau} \, , \tag{5.19}$$

and the relaxation time of the soft mode,

$$t_c = \frac{1}{\Gamma \, V''(a_u = 0)} = \frac{1}{\Gamma \, \kappa\tau}, \tag{5.20}$$

[12] Nonlinearities become important for $g \left\langle a_u^2 \right\rangle \gtrsim \tau$, i.e., $\tau \lesssim \sqrt{g \, (k_B T/\kappa)}$, which is again the same criterion.

still diverge with the ("critical") exponents $\zeta = -1$, as the critical reduced volume v_c is approached from above.

For reduced volumes below v_c, the situation is quite different. For $\tau < 0$, the stable minimum now is at $a_0^- = \pm\sqrt{-\tau/g}$, representing two degenerate pears related by mirror symmetry. The symmetric, "prolate" point, $a_u = 0$, is now at the top of an energy barrier, $-V(a_0^-) = \kappa\tau^2/4g$, which separates the two energy degenerate minima. As long as this energy barrier is small compared to k_BT, one expects strong fluctuations. Beyond this point the shape settles into one of the new asymmetric minima and increases its asymmetry according to $a_u^- \sim (v_c - v)^{1/2}$. Fluctuations around this shape have mean-square amplitudes proportional to $V''(a_u^-) = -1/(2\tau\kappa) \sim 1/(v_s - v)$, which is large near the transition but become less pronounced. Note the contrast with the spinodal behavior described in the previous subsection, where beyond the instability the asymmetry parameter, $\langle a_u \rangle$, jumps to a finite value and the fluctuations decrease abruptly to a low, noncritical level in the budded configuration. Thus, the two cases are easy to distinguish experimentally.

5.3 Experimental Results

This Section presents experimental results for the fluctuation spectrum of the budding transition. We will first look at the static properties in Sec. 5.3.1; then, in Sec. 5.3.2, the dynamical behaviour will be explored.

5.3.1 Statics: Mean Square Amplitudes

As the budding transition is approached, prolate vesicles show enhanced symmetry-breaking fluctuations. In Figs. (5.2) and (5.3), video sequences of a fluctuating vesicle, which we will denote henceforth as vesicle "A," are shown for two different reduced volumes. Several snapshots at equal time delays were taken. Far away from the transition, i.e., at a large reduced volume, the vesicle fluctuates weakly around a symmetric state (see Fig. (5.2)).

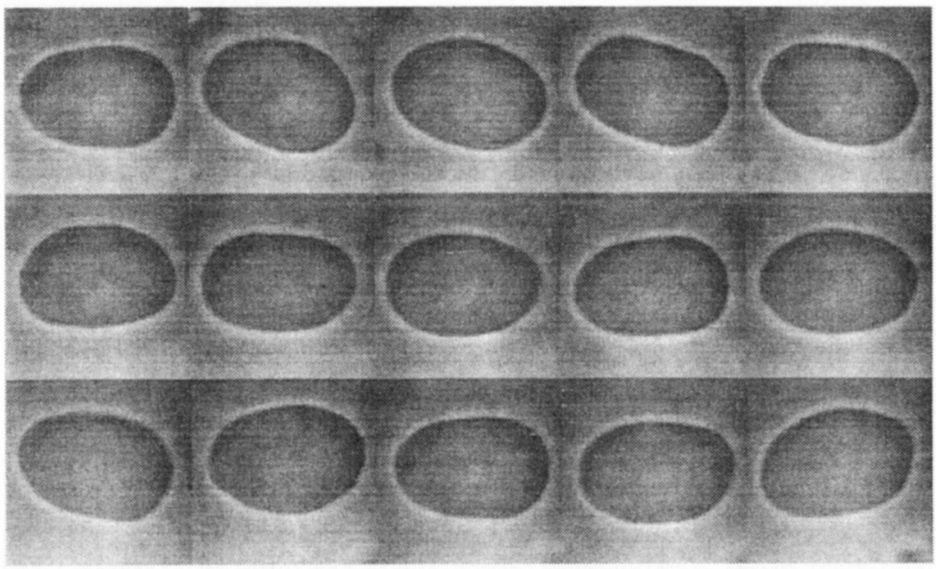

Figure 5.2: Time sequence of images of a fluctuating vesicle ("A") at $v = 0.954$. The elapsed time between each snapshot is 6.3 seconds. In the figure, the images are ordered in time from the upper left to the lower right. The vesicle fluctuates around an axisymmetric prolate shape. Each particular contour, however, is non-axisymmetric. The linear dimension of the images is approximately 20 μm.

This changes dramatically as the reduced volume is decreased towards the transition (see Fig. (5.3)). There are now frequently quite strong deformations away from the prolate shape. This change in the fluctuation spectrum can be nicely seen in Fig. 5.4, where time sequences of the a_3 amplitude are compared for the two reduced volumes of vesicle "A" illustrated in Figs. 5.2 and 5.3. The strong asymmetric fluctuations which are visible in the video pictures

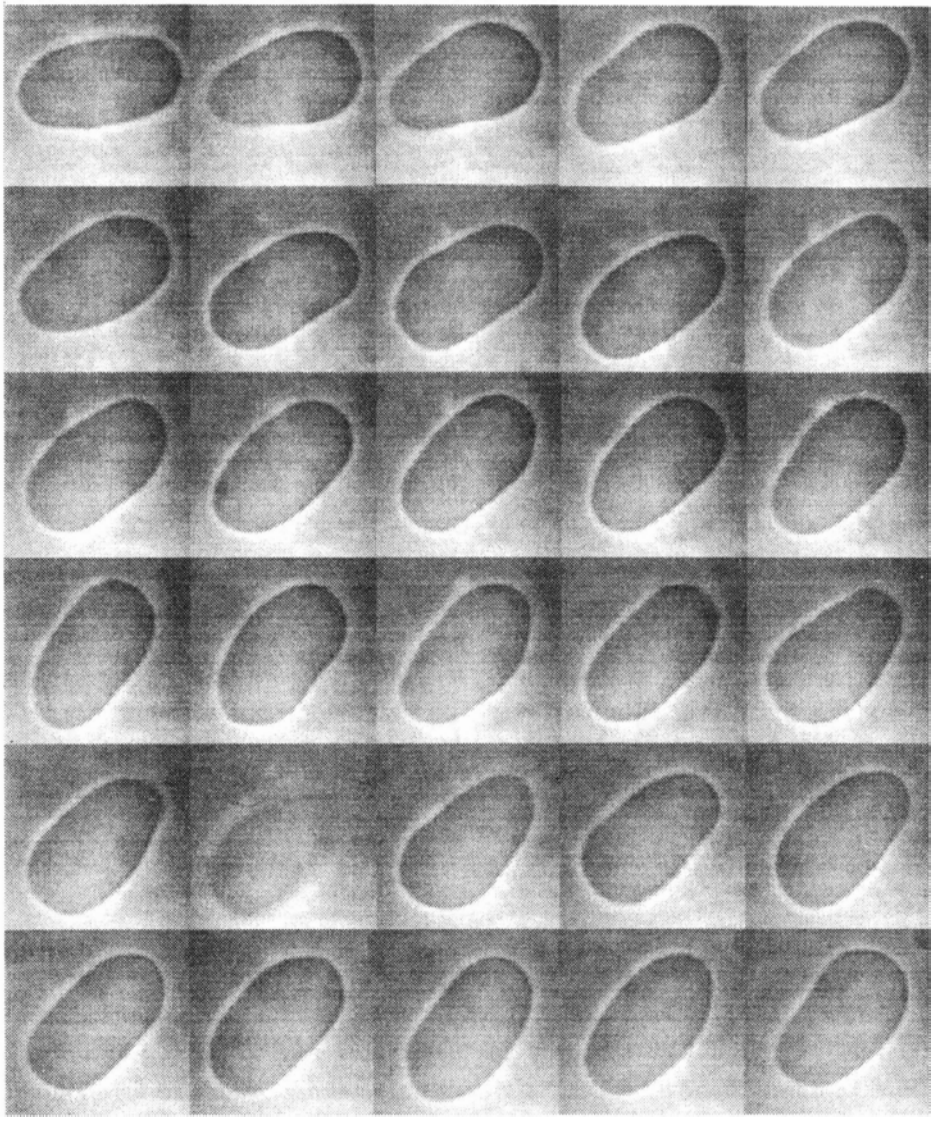

Figure 5.3: Time sequence of images of vesicle "A" at $v = 0.912$. The elapsed time between each snapshots is again 6.3 seconds. In the figure, the images are ordered in time from the upper left to the lower right. The vesicle is now more elongated than it was at $v = 0.954$. Strong pear-shape fluctuations are clearly visible. Note, the great variability in the degree of asymmetry of the instantaneous shape.

are reflected in the time series of the a_3 amplitude as excursion to large positive or negative values. Note for future reference that the amplitudes a_3 are characteristically both larger in magnitude and slower in time at the lower reduced volume. Vesicle "A" became unstable at reduced volume $v = 0.878$.

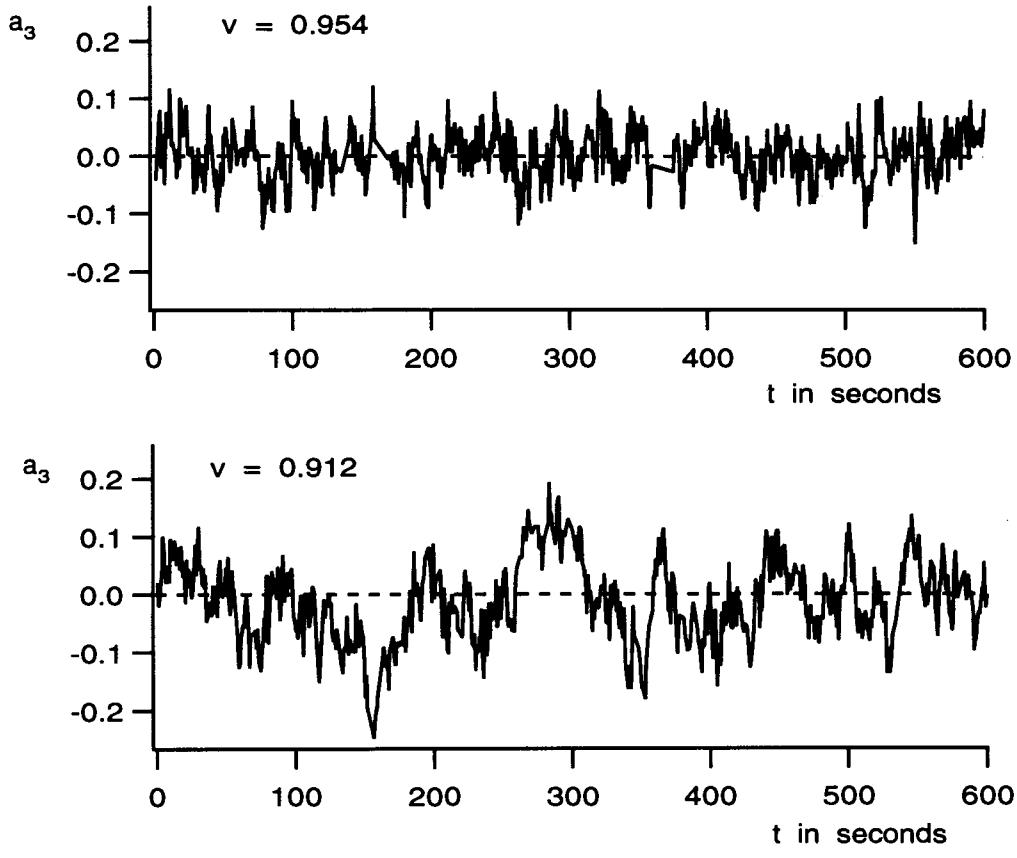

Figure 5.4: Time series of the a_3 amplitude of vesicle "A" at reduced volumes $v = 0.954$ and $v = 0.912$. The dashed line corresponds to zero amplitude. The amplitude a_3 is characteristically both larger in magnitude and slower in time at the lower reduced volume.

This qualitative picture of the enhancement of symmetry breaking fluctuations near the spinodal instability can be analyzed quantitatively by calculating the mean-square amplitude fluctuations, i.e., the static part of the amplitude-amplitude correlation function. In Fig. 5.5, the mean-square amplitudes $\langle (a_n - \langle a_n \rangle)^2 \rangle$ of vesicle "A" are shown as a function of the reduced volume v. There is an increase in magnitude of all modes with decreasing volume. However, the amplitudes of the first and third mode show a rapid growth as v decreases towards the instability point, whereas the amplitudes of the other modes stay approximately constant by comparison.

Another way to look at the data of Fig. 5.5 is to plot the mean-square amplitudes as a function of the mode number n. In Fig. 5.6, the resulting fluctuation spectra are shown. As expected theoretically [42], the amplitudes fall off for higher mode numbers. Note that, the second mode is strongly suppressed. This is a consequence of the area and volume constraints on the vesicle fluctuations [68]. The spectra recorded at lower reduced volume clearly show a strong growth of the third mode. [13]

[13] The growth of a_1 is not conveniently visible on the scale of this plot.

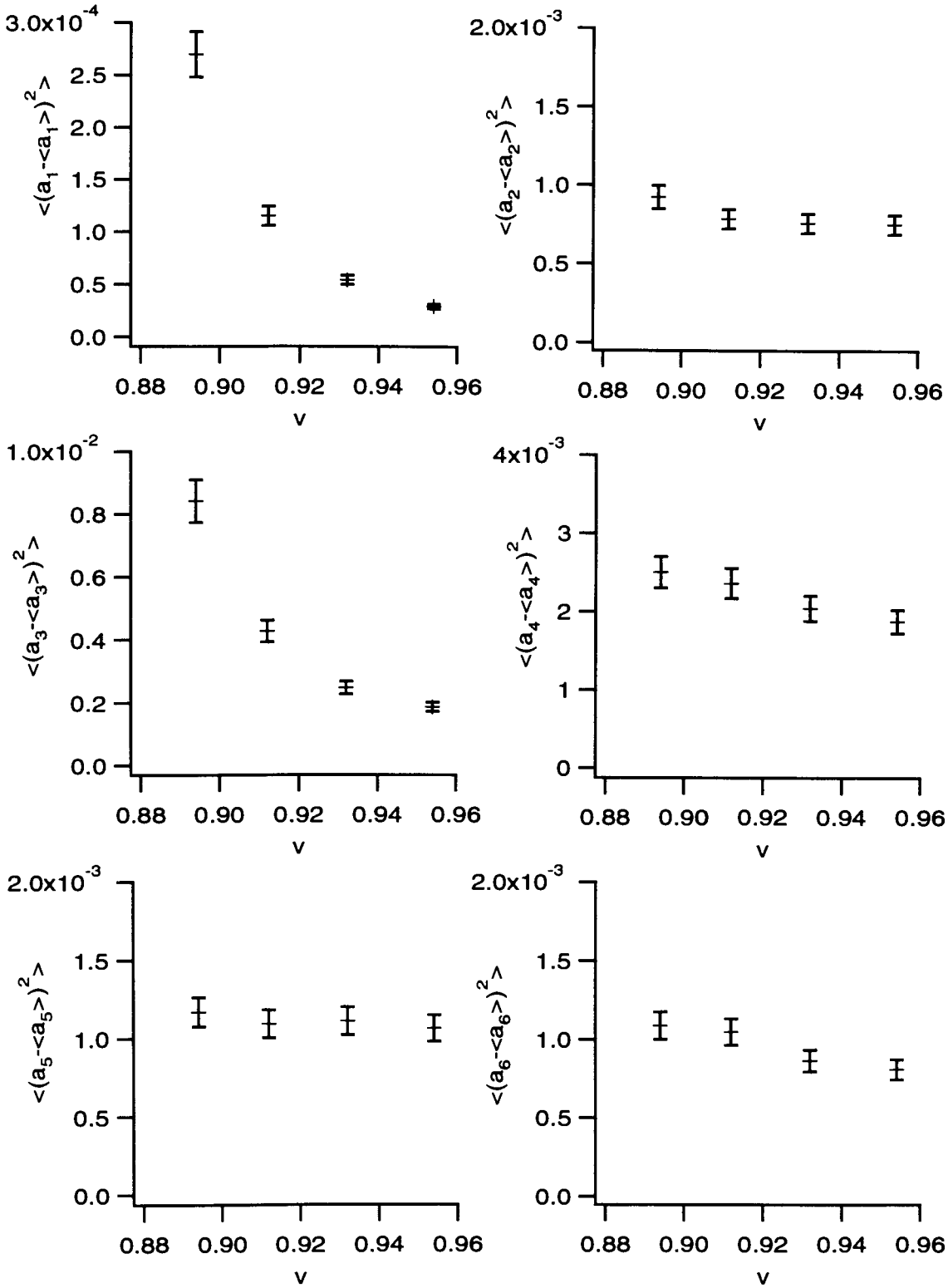

Figure 5.5: Mean square amplitudes of the first six modes for vesicle "A" at different reduced volume. The amplitude fluctuations of the first and third mode apparently diverge. Note, the different vertical scales.

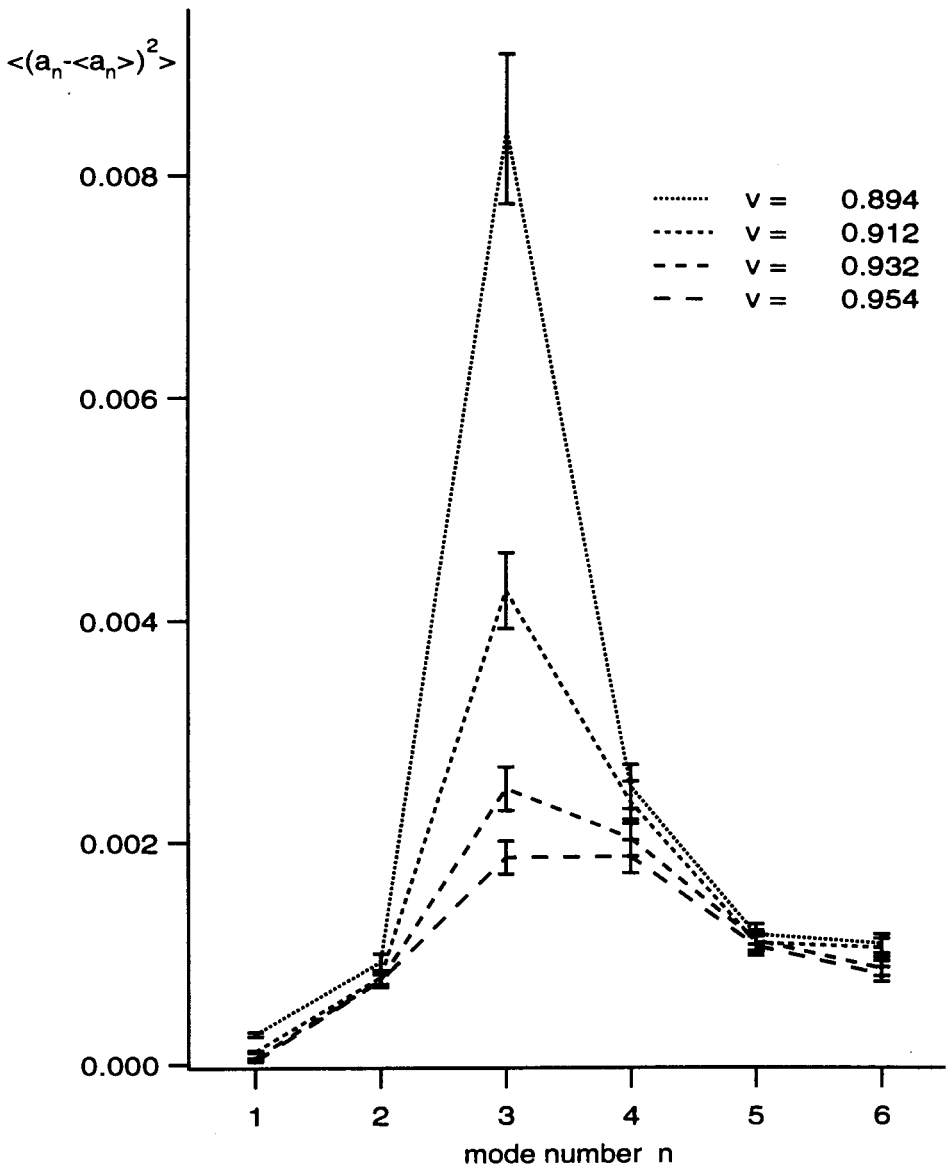

Figure 5.6: Fluctuation spectra of vesicle "A" as it approaches the budding transition: Mean-square amplitudes as a function of the mode number n at different reduced volume v. The amplitude fluctuations peak strongly at the "soft" third mode as the spinodal instability is approached.

5.3.2 Dynamics: Relaxation Time

We now turn to a description of the observed dynamics near the budding transition. We have argued in Sec. 5.2.1 that, as the spinodal line is approached, one expects not only an increase in the amplitude of the soft mode but also a corresponding increase in its time scale. Indeed, that is what is observed in experiment. A comparison of Figs. 5.2 and 5.3 reveals a clear distinction in time scale between pear fluctuations of the prolate shape at large v versus small v. Inspection shows that at large v vesicle shapes are essentially uncorrelated between the frames shown, whereas at small v there is substantial correlation in the degree of "pearness" between subsequent snapshots. Both time sequences were recorded with the same time difference (6.3 seconds) between frames.

This feature is captured in the time-dependent amplitude correlation functions of the third mode $\langle a_3(0)a_3(\Delta t)\rangle$ for different reduced volume v. These functions are depicted in Fig. (5.7) for vesicle "A." All correlation functions are calculated directly from the time

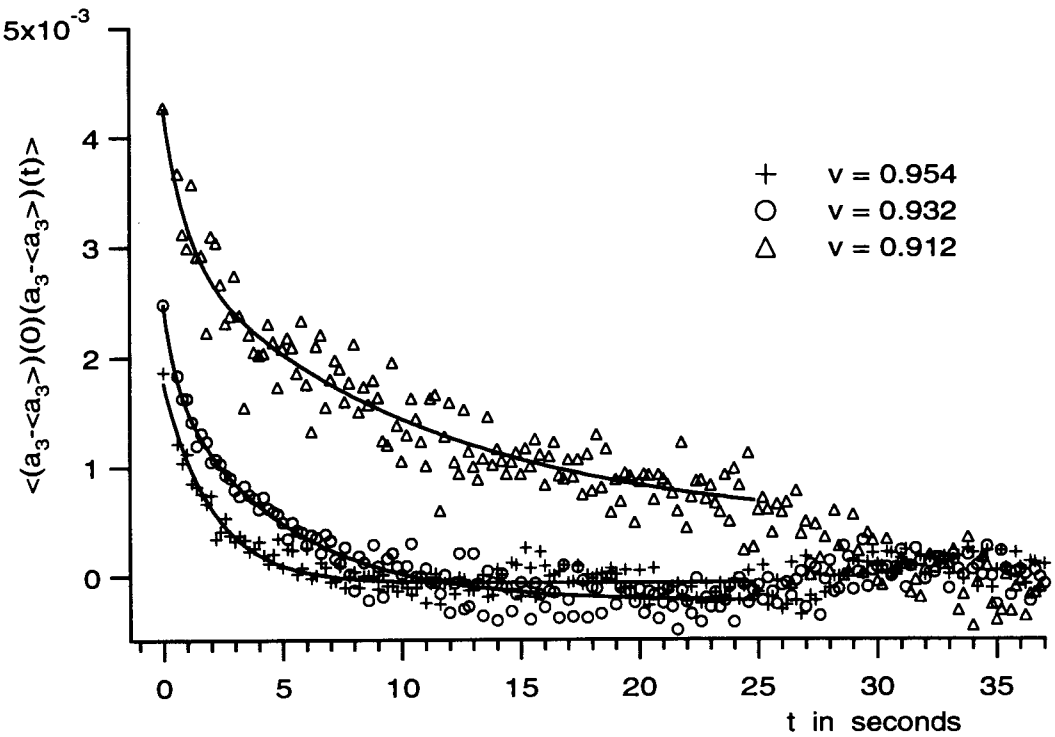

Figure 5.7: Time-dependent amplitude correlation function of the third mode for different reduced volumes v. The solid curves are the result of fitting a biexponential ($v = 0.912, v = 0.932$) and exponential ($v = 0.954$) function to the data.

series as

$$< a_n(0)a_n(\Delta t_j) >= \frac{1}{N_j}\sum_{i}^{N_j} a_n(t_i)a_n(t_i + \Delta t_j), \tag{5.21}$$

where $\Delta t_j = j \times 0.2s$ and N_j is the number of pairs with a time lag Δt_j. [14]

The time-dependent amplitude correlation functions (5.21) may be expected to be composed of a sum of contributions from distinct dynamical modes, [15] each decaying exponentially with some characteristic relaxation time [42]. It is, therefore, common to parameterize such functions as a sum of exponentials,

$$< a_n(0)a_n(\Delta t_j) >= A_1 \exp(-t/t_{c,1}^{(n)}) \quad + \quad A_2 \exp(-t/t_{c,2}^{(n)}) \; + \; \cdots. \tag{5.22}$$

The dominant relaxation time was extracted for each mode, $n = 2, 3, 4, 5$, and 6, by least-squares fit. In general, the data support only a single-exponential fit. Near the instability and for modes $n = 3$, we used a biexponential fit (see Fig. 5.7). In Table (5.1), the relaxation times of the first six modes are shown as a function of the reduced volume. The corresponding temperatures are also given. All relaxation times stay approximately constant with reduced volume, except the one for the third mode. The relaxation time of this mode shows a strong increase as the budding instability is approached. For the lowest reduced volume measured ($v = 0.894$) before the instability, a fit of the correlation function was not attempted, due to the very slow decay and high noise level at large times. Note that the correlation times of modes two, and four to six fall off with increasing mode number, as expected theoretically [42] for non-critical thermal fluctuations.

T in °C	28.7	32.7	37.8	42.4
v	0.954	0.932	0.912	0.894
$t_c^{(2)}$ in s	2.3 ± 0.4	1.8 ± 0.4	1.9 ± 0.4	2.8 ± 0.4
$t_{c,1}^{(3)}, t_{c,2}^{(3)}$ in s	2.2 ± 0.4	0.6 ± 0.2, 4.8 ± 1.0	1.0 ± 0.3, 11 ± 2.2	-
$t_c^{(4)}$ in s	1.4± 0.3	1.2± 0.3	1.3 ± 0.3	1.7 ± 0.4
$t_c^{(5)}$ in s	0.5 ± 0.2	0.5 ± 0.2	0.5 ± 0.2	0.5 ± 0.2
$t_c^{(6)}$ in s	< 0.4	< 0.4	< 0.4	<0.4

Table 5.1: Relaxation times of the first six modes for different reduced volume v.

In the video sequences, the final transition to the budded configuration takes place via a giant thermal fluctuation which does not decay. The vesicle remains for some time in a

[14] For the grabbing of frames at "equally" distant times $t \approx t_i$, we allowed for a small time window with $0 < (t - t_i) < 0.05s$. Events were collected in bins centered at t_i for calculation of correlation functions. This coarse graining procedure does not affect relaxation times but overestimates amplitudes with relaxation times $\tau \leq \frac{1}{\sqrt{24}} 0.05$ s.

[15] The dynamical eigenmodes are not, in general, the same as the static eigenmodes.

shape with an "open" neck (see Fig. 5.8); finally, the neck closes down completely, i.e., its

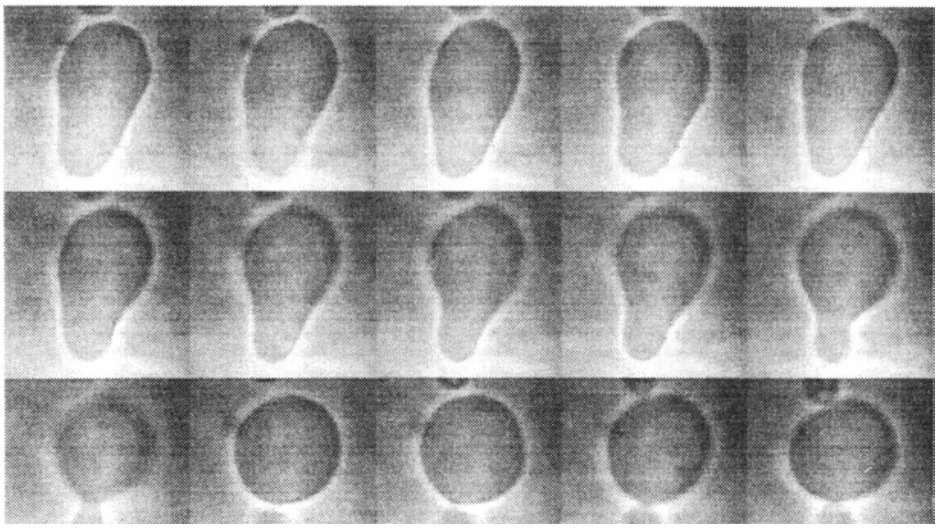

Figure 5.8: Time sequence of images during budding. The time elapsed between each frame is 1.2 seconds. Vesicle "A" ($R_V = 8.8\ \mu m$) diffuses over the barrier of the metastable prolate state. The reduced volume is $v \simeq 0.878$.

radius shrinks to a value below optical resolution. The resulting shape then becomes two fluctuating spheres or a fluctuating prolate ellipse with a quasi-spherical bud. The pear-shaped transients, which appear in the first few frames, never reappear at later times, where only the two-sphere configurations are present. The fluctuation amplitudes of the budded shape are strongly reduced with respect to the metastable shape before the transition. Thus, there are no visible "critical" fluctuations of the vesicle *after* the transition, as would be expected if the transition were second-order.

It is important to note, that the first few pictures of the time sequence in Fig. 5.8 do *not* represent the mean shape of the vesicle right at the instability. This is evident in Fig. 5.9, where another time sequence of the same vesicle is shown for a slightly smaller reduced volume ($\Delta v \simeq 0.005$). In fact, in this regime the notion of a mean shape is not well defined as explained at the end of Sec. (5.2.1).

The time scale of the escape of the vesicle out of the metastable state depends strongly on size. In Fig. 5.10, budding of a smaller vesicle ("B") is shown. This vesicle overcomes the barrier much more quickly than does vesicle "A." This is as expected theoretically for the diffusion over the saddle point, since fluctuation times scale with the third power of the radius of the vesicle (see Eq, (5.15)).

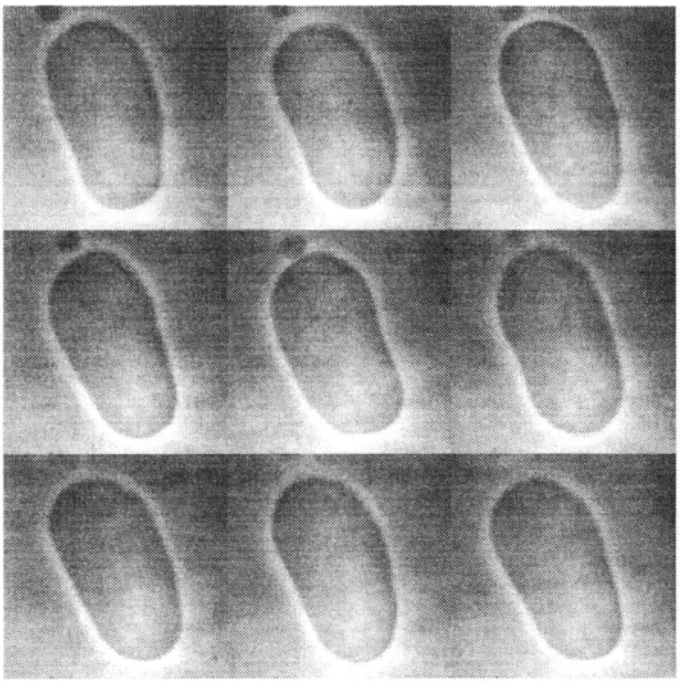

Figure 5.9: Time sequence of images of vesicle "A" just below the budding instability, at $v \simeq 0.883$. At this reduced volume, the vesicle is only 0.005 units away from budding (compare Fig. (5.8)). Note that the vesicle appears to be prolate in this sequence. The time elapsed between frames is 1.2 seconds. The apparent "bud" in the middle frame of this sequence is just an independent small vesicle floating by as is evident from the snapshots before.

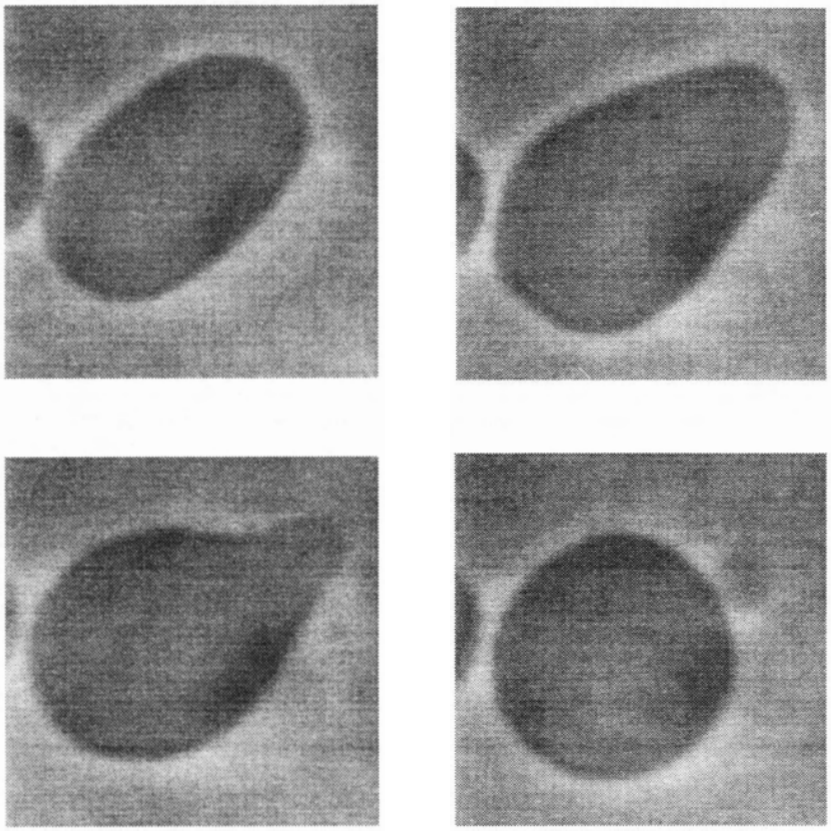

Figure 5.10: Time sequence of images during budding for vesicle "B." The time elapsed between each frame is 1.2 seconds. This vesicle "B" ($R_V = 5.4\ \mu m$) diffuses over the barrier of the metastable prolate state much quicker than vesicle "A" ($R_V = 8.8\ \mu m$) in Fig. 5.8.

5.4 Discussion

We discuss now the experimental data on the budding transition presented in the previous Section and compare them to theory.

As we have argued in Sec. 5.1, the ADE model predicts a first-order budding transition for PC vesicles. In this transition, the up/down symmetry of the prolate shape is broken. We may choose – guided by the experimental results – the amplitude a_3 of the third mode as a suitable measure of this symmetry breaking. [16] The mean value $\langle a_3 \rangle$ is (approximately) zero for a symmetric prolate shape and has a finite value in the budded configuration.

In Sec. 5.4.1, we collect all the experimental facts which suggest a first-order budding transition. First, we investigate the static and dynamic properties of the fluctuations of the third mode. We shall find evidence for the existence of a spinodal line. Second, we discuss the mean asymmetry parameter. A large spontaneous jump in this quantity at the spinodal instability supports the notion of a first-order transition. We conclude from the experimental data that there are only two phases, [17] the prolates and the pears, between the spherical shape and the limiting line. We identify the first-order transition between these two phases as the budding transition of the ADE model.

The behaviour of the mean amplitude of the third mode will be further investigated in Sec. 5.4.2. We find that the third amplitude seems *always* to have a small but statistically significant non-zero value, which becomes larger as the spinodal line is approached. One has to conclude from the experimental data that the up/down symmetry is always broken even in the "prolate" phase. Nevertheless, we will show that the effect is, in fact, quite small. The principal phases of the ADE model are preserved and the scaling behaviour of the soft eigenmode is not changed from what one expects within that model. We believe that the origin of small symmetry breaking is extrinsic, as we shall discuss more fully in Sec. (5.4.2).

In Sec. 5.4.3, we relate our results to previous experiments on the budding transition.

[16] In Sec. 5.2.1, it was shown that the instability of the prolate shape near the spinodal line of the budding transition reflects the existence of a soft mode, which breaks the up/down symmetry of the prolate shape. Since in our expansion (see Eq. 4.10) it is the odd modes which break this symmetry, and eigenmodes with different parity do not mix, the soft eigenmode can only have contributions from odd modes. As we have seen experimentally, the strongest contribution comes from the third mode. Therefore, it makes sense to choose the third mode as a measure of asymmetry.

[17] There have been reports of three possible distinct phases in previous experiments [50].

5.4.1 Evidence for a First-Order Budding Transition

Statics and Dynamics of Shape Fluctuations

The experimental results of the last section show clearly the existence of a soft mode of the prolate shape near the spinodal line of the budding transition. The evidence presented includes dramatic growth (apparent divergence) of both the static fluctuations ("spinodal fluctuations") and the characteristic decay time ("spinodal slowing down") for the amplitude of the third shape mode, a_3. In order to characterize this divergence further, we apply the scaling analysis derived in Sect. 5.2 to the amplitude of the third mode. This is legitimate since we have found experimentally that the projection of the soft mode has a large component in the a_3-direction. [18]

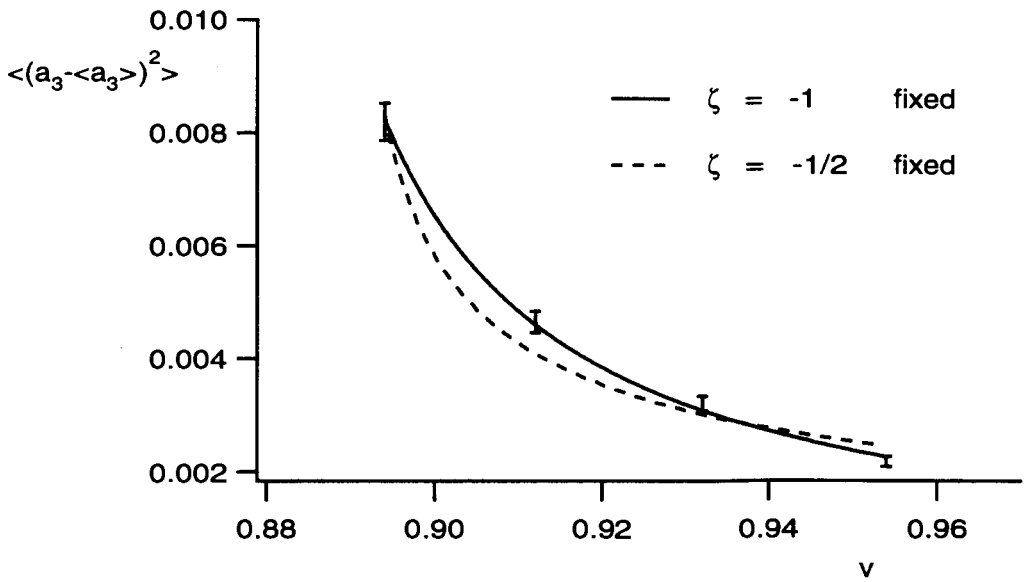

Figure 5.11: Power-law fits to the behaviour of the mean-square amplitude of the third mode of vesicle "A." Fit results for two different (fixed) exponents are shown. The theoretically expected exponent $\zeta = -1$ for budding out of a prolate shape gives the better fit. For a discussion of the exponent $\zeta = -1/2$ for budding out of a "pear" shape see Sec. 5.4.2.

[18] The only other noticeable component is along the a_1 direction. However, there is no new information on the soft mode in the a_1 amplitude. It is basically reflecting the behaviour of a_3 in this respect. The reason for that is the closure condition Eq. (4.12), which reads $a_1 \simeq 1/2\ a_2 a_3 + \cdots$. Noting that the mean value of a_2 is typically an order of magnitude larger than its fluctuations, i.e., $\langle a_2^2 \rangle \simeq \langle a_2 \rangle^2$, and setting $\langle a_1 \rangle$ and $\langle a_3 \rangle$ to zero, we find for the mean square fluctuations of the first mode $\langle a_1^2 \rangle \simeq 1/2 \langle a_2 \rangle^2\ \langle a_3^2 \rangle$. Thus, the mean-square fluctuations of the first and third mode are approximately linear dependent on one another.

In Fig. 5.11, the result of a power-law fit to the mean-square amplitude,

$$\left\langle (a_3 - \langle a_3 \rangle)^2 \right\rangle (v) \sim \frac{A_3}{v - v_s} \quad , \tag{5.23}$$

is shown. For the position of the apparent singularity, which gives the location of the instability, we find $v_s^{\text{static}} = 0.87 \pm 0.01$. The same procedure can be applied to the (long) relaxation time of the third mode (see Fig. 5.12) and yields $v_s^{\text{dynamic}} = 0.90 \pm 0.01$. Thus,

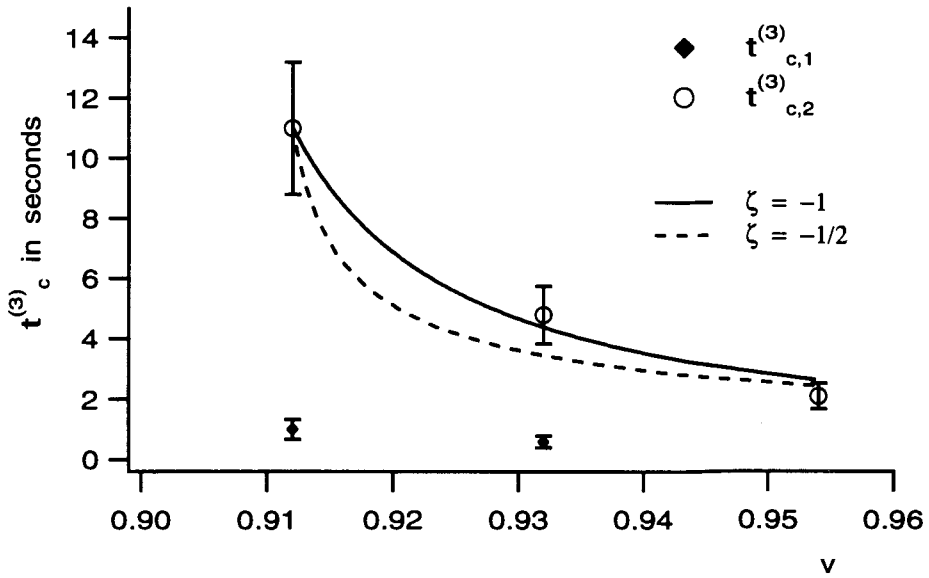

Figure 5.12: Power-law fits to the growth of the longest correlation time of the third mode.

we find that the growth in both the static fluctuations and the dynamical relaxation times of the third mode is consistent with the theoretical expectation of $\zeta = -1$ and, consistently, the separate fits give approximately the same location of the instability.

A third independent estimate of the location of the instability can be obtained by extrapolating the thermal trajectory (see Fig. 5.13) of the reduced volume to the budding temperature. The thermal expansion coefficient β can be read off from the slope of this plot of the reduced volume versus temperature by using Eq. (6.24). One finds a thermal expansion coefficient $\beta = (2.9 \pm 0.2) \times 10^{-3}$. The same coefficient has been found by the pipette technique [10]. Using this number, one extrapolates to a volume $v_s^{\text{thermal}} = 0.878 \pm 0.001$. Note that the latter number is found with a ten-fold higher accuracy than it is possible from the power-law fits.

Thus, reduced volume at which the budding instability occurs can be determined in three independent ways, and good agreement is found. The exponents ζ_s and ζ_d provide

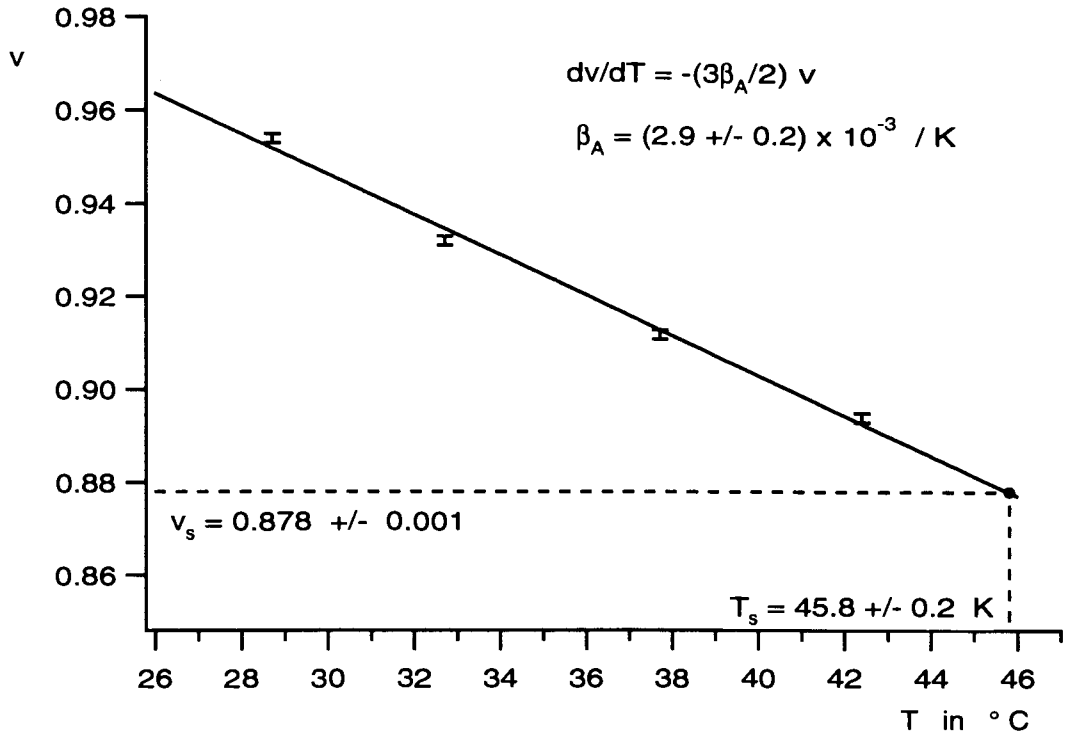

Figure 5.13: Reduced volume of vesicle "A" as a function of temperature, approaching the budding instability from below. The slope of the straight-line fit gives the bilayer thermal expansion coefficient (see Sec. (6.4)) and is consistent with other determinations of this quantity [10]. By extrapolating to the observed transition temperature, we can infer a precise value for the reduced volume at the instability (see text).

clear quantitative signatures of the budding instability. On this basis, we may conclude that we are observing (first-order) budding close to a spinodal line (metastability limit).

In principle, a second-order transition could give the *same* pretransitional scaling behaviour (in the prolate phase) as expected for the approach to the spinodal for both of the mean-square amplitudes and relaxation times of the third mode (see Sec. 5.2.2). However, in the case of a second-order transition, one would not see an instability of the shape, i.e., the degree of asymmetry would not grow suddenly and spontaneously at the transition. Instead, the shape asymmetry would increase continuously and strong fluctuations would persist beyond the transition, as long as the energy barrier separating the two degenerate asymmetric minima remained small compared to $k_B T$. This is clearly not what is seen in experiment. Thus, a second-order transition can be ruled out, and we determine the budding transition to be first-order.

Asymmetry Parameter

As we have seen, the amplitude a_3 of the third mode plays the role of an "order" parameter of the budding transition. In principle, its numerical mean value is zero in the up/down symmetric prolate phase, and nonzero in the pear (or fully vesiculated phase), which has lost the up/down symmetry. The orientation of a pear-like vesicle fixes the sign of its a_3 amplitude. Since both possible orientations (and, indeed, a complete rotational family of shapes) have equal bending energy and, in fact, correspond to the same vesicle shape, it is advantageous to use the absolute value of $\langle a_3 \rangle$ to characterize the degree of symmetry breaking. Henceforth, when we use the word "asymmetry (parameter)", we shall mean the mean absolute amplitude of the third shape mode, $|\langle a_3 \rangle|$.

For a first-order transition with metastability, one expects a jump in the order parameter at (or close to) the spinodal instability. This is exactly what is seen in the case of the budding transition. In Fig. 5.14, experimentally determined values for the asymmetry of the budded configuration (and the saddle point) are plotted along with the values in the prolate phase for vesicle "A". There is, indeed, a clear jump in the asymmetry by an order of magnitude at the instability of the prolate shape. This is another strong indication of a first-order transition.

5.4.2 Weakly Broken Reflection Symmetry of Experimental Vesicle Shapes.

Although the asymmetry in the "prolate' phase is approximately zero, at least compared to its value in the budded phase, nevertheless, it is larger than zero in a statistically significant way for *all* $v < 1$. The reason for this weakly broken symmetry of the prolate phase is not clear. In the following, we investigate the consequences of this weak asymmetry for the theoretical interpretation of our data. We will arrive - in several ways - at the conclusion that the effect is quite small, as is already evident from Fig. 5.14. We believe that, at this point, there is no reason to doubt the validity of the ADE model. Our interpretation of the data is that experimental vesicle shapes are governed mainly by the physics of the ADE model. However, all shapes, especially the prolate phase, are slightly altered by a weak extrinsic source of asymmetry of unknown origin.

It is important to realize that our shape experiments are conducted on *single* vesicles and not on some kind of vesicle ensemble. Each vesicle has to be inspected individually to avoid obvious artifacts. In a typical experimental chamber, one finds quite often vesicles

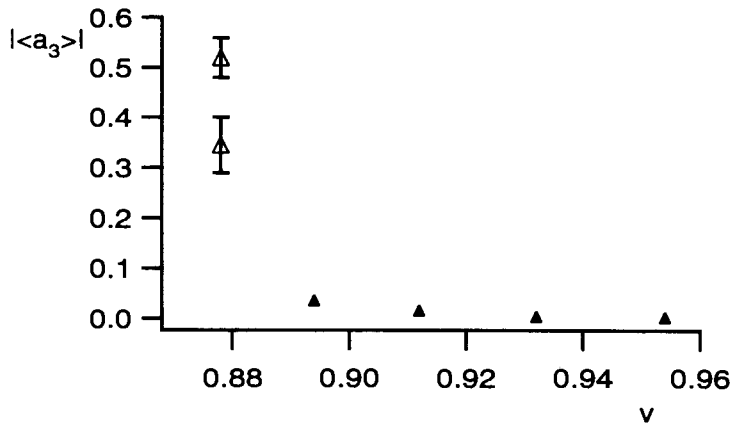

Figure 5.14: Asymmetry parameter ($|\langle a_3|\rangle$) of vesicle "A" at a sequence of reduced volumes. Within the "prolate" phase (i.e., before the jump), the symmetry is only slightly broken (see Sec. (5.4.2). At the instability to the budded configuration the asymmetry jumps by an order of magnitude. The two hollow triangles depict the asymmetry of the saddle point and of the budded shape, respectively. The asymmetry of the shape on the saddle point is estimated from a few vesicle contours, taken during diffusion over the energy barrier. The asymmetry of the budded shape is obtained from a measurement of the radii of the two spheres. ($|a_3|$ can be calculated analytically from the ratio of the radii of the two-sphere shape.)

which have a small but visible "defect" [19] but are otherwise topologically spherical, "nice" vesicles. In these observations, there is a correlation between the position of the defect on the membrane and the local curvature of the vesicle. In most cases, defects tend to curve the membrane more strongly at the point where they are incorporated into or attached to the bilayer. Another potential source of asymmetry are local attachments of the vesicle to the substrate. The vesicle can get entangled on a rough spot on the glass slide and thereby develop a slightly asymmetric shape. We have to the best of our ability excluded such vesicles from the analysis by visually inspecting the membrane and monitoring the (free) rotational and translational diffusion of the vesicles. Fortunately or unfortunately, even after rejecting such obvious artifacts, some (extrinsic) asymmetry apparently remains.

We examine now the "size" of this extrinsic asymmetry. In Fig. (5.15), the asymmetry

[19] By "defect," we mean, e.g., a small microbud, which does not exchange area with the vesicle, or a small piece of junk within the membrane.

(within the "prolate" phase) of vesicle "A" is shown on a scale larger than that of Fig. 5.14. What is plotted are the asymmetry parameters of the left and right side of the contour and their average for different reduced volumes. The average asymmetry seems to extrapolate

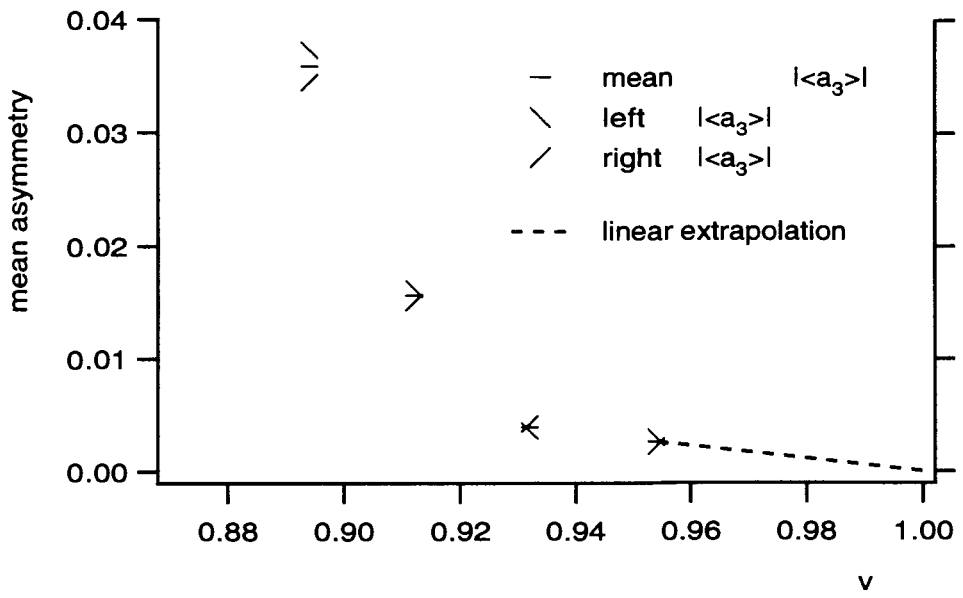

Figure 5.15: Mean absolute amplitude of the third mode, $< a_3 >$, for vesicle "A." This observable is a measure of the asymmetry of the shape. Note the vertical scale.

to zero for a spherical vesicle, as it must. It is evident that the asymmetry gets larger as the spinodal line is approached. The reason for this enhancement of the extrinsic asymmetry of the vesicle is very likely the existence of the soft mode, itself. Near the instability, it costs increasingly less (bending) energy (within the ADE model) to force a change in the soft mode amplitude, so a_3 becomes highly "susceptible" to any small additional terms in the Hamiltonian. We will come back to this reasoning below in more detail.

We emphasize that the dramatic increase in asymmetry (by an order of magnitude), visible in Fig. (5.15), is actually quite small on the scale of the asymmetry of the saddle point and the fully vesiculated budded shape, as shown in Fig. (5.14). In fact, the asymmetry of the mean vesicle shapes corresponding to the two largest reduced volumes is hardly visible by eye. In any case, one would like to have some tool at hand to estimate the importance of the symmetry breaking more quantitatively than just by looking at plots of the asymmetry.

Within the framework of a Landau theory, a simple method to deal with such an unknown source of asymmetry is to introduce a "magnetic field" h into the Landau functional. Such a field breaks the reflection symmetry of the original Landau model and allows one – quite generally – to investigate the consequences of a small asymmetry for the prolate phase.

We start by writing down an appropriate Landau potential for a first-order budding transition out of a pear state,

$$V(a_u) = \kappa[-ha_u + \tau a_u^2/2 - g a_u^4/4 + u a_u^6/6], \tag{5.24}$$

where a_u is, again, the amplitude of the soft mode. One performs now the same kind of calculations as outlined in Sec. (5.2.1). After some algebra (see Appendix C), one finds that the correlation time and the static mean-square fluctuations in the metastable state obey different power-laws (as a function of the distance in reduced volume from the the spinodal line) from those of the symmetric case, Eqs. (5.6) and (5.12). We find, in particular, that

$$\begin{aligned} t_c &\sim 1/(T_s - T)^{1/2} \\ \left\langle (a_u - \langle a_u \rangle)^2 \right\rangle &\sim 1/(T_s - T)^{1/2}\,, \end{aligned} \tag{5.25}$$

where $\langle a_u \rangle$ is the average asymmetry of the metastable state. Thus, we expect modified exponents, $\zeta_s = \zeta_d = -\frac{1}{2}$, for the budding instability. The characteristic power laws for the correlation function hold universally, whenever the decaying metastable state is asymmetric, irrespectively of the physical origin of the asymmetric term.

We do *not* see the exponents (5.25) in the observed fluctuations of the third mode. As shown in Fig. (5.11), a scaling exponent, $\zeta = -1/2$, does not give a good fit to the data. We might draw the same conclusion from the result of the constrained fits (Fig. (5.12) to the correlation times.

How can this result be understood? Shouldn't we see an exponent $\zeta = -1/2$ instead of $\zeta = -1$? After all, budding takes place out of a shape which is (weakly) asymmetric. The answer is, "no," the soft mode should only show the asymmetric exponent in a regime where the fluctuations in the asymmetry are much smaller than the mean value, i.e., in some "inner critical" regime. In fact, in our measurements, the opposite is the case: the fluctuations are always much larger in amplitude than the mean value. Thus, we are still in the "outer critical" regime, where the fluctuations do not show the characteristics of asymmetric budding.

To quantify this statement further, let us compare the energy which is stored in the weak pear with the energy in the fluctuations around that shape. Setting the Landau parameters

g and u to zero (for simplicity) in the Landau functional (5.24), we find for the mean energy of the weak pear

$$E_{\text{pear}} = -\frac{1}{2}\,\kappa\tau\ <a_u>^2\ . \tag{5.26}$$

Since the curvature at the minimum is $\kappa\tau$, the mean energy of a thermal fluctuation is

$$E_{\text{fluct}} = \frac{1}{2}\,\kappa\tau\ <(a_u - <a_u>)^2>\ . \tag{5.27}$$

Thus, we find for the ratio of the two energies

$$\left|\frac{E_{\text{pear}}}{E_{\text{fluct}}}\right| = \frac{<a_u>^2}{<(a_u - <a_u>)^2>}. \tag{5.28}$$

We can calculate this ratio from the experimental data by identifying a_u with a_3. This is a good approximation, since the soft mode points almost exclusively along the a_3 direction. The ratio is plotted in Fig. (5.16) for vesicle "A." One observes that the energetic contribu-

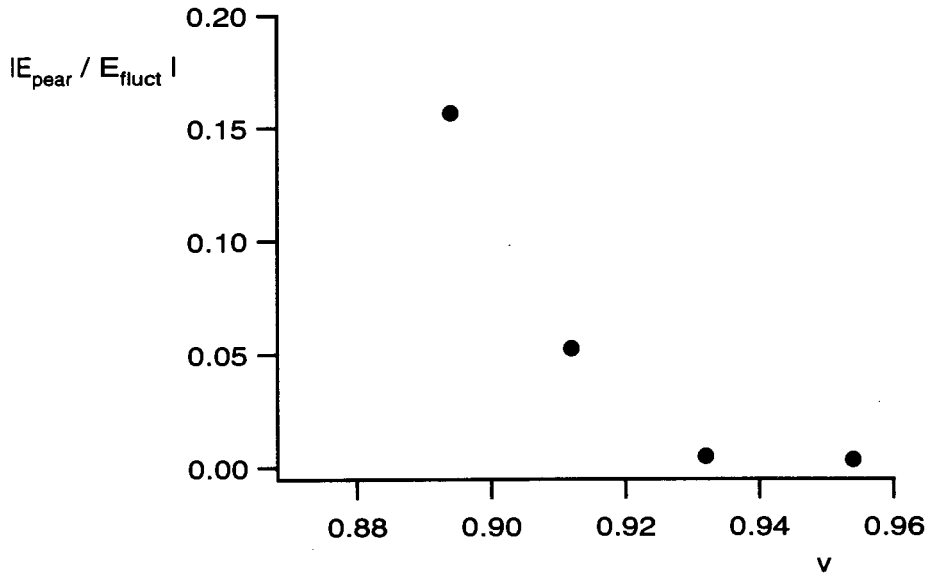

Figure 5.16: Ratio of the energy of the mean pear shape to the mean energy of a fluctuation along the direction of the soft mode.

tion of the symmetry breaking term is always small, even in the region where the intrinsic asymmetry gets enhanced by the symmetry breaking soft mode. Therefore, the vesicle shape is governed largely by the physics of the (symmetric) ADE model and properly exhibits the various phases of that model.

The preceding discussion justifies, a posteriori, the identification of the experimentally observed weak pears with the prolate phase of the ADE model.

5.4.3 Relation to Previous Experiments on the Budding Transition

We are now in a position to relate our results to previous experiments on the budding transition performed by Käs and Sackmann [50]. These authors have reported the following sequence of events leading from a quasi-spherical shape to a fully vesiculated (closed-neck) budded shape: First, a quasi-spherical vesicle becomes a symmetric prolate. Second, the prolate vesicle looses its reflection symmetry in a continuous, second-order transition and develops into a strong pear. Finally, third, the pear (with an open neck) becomes unstable to a fully vesiculated shape (with a closed neck) in a discontinuous, first-order transition. [20]

The experimental scenario reported by Käs and Sackmann is in contrast to our results and, in fact, not available within the ADE model. Although the ADE model allows the budding transition to be either first- or second-order, depending on the value of α, the subsequently reported first-order transition is not present within that model. Podgornik et al. [71] proposed to explain this additional transition by introducing into the bending energy a term cubic in the area difference. The problem with such an interpretation is that, in order to produce the experimentally observed sequence, the authors were forced to assume a coefficient of this term which is a factor 10^5 higher than the value one expects theoretically [58]. Thus, we prefer to reject this explanation.

Comparing our results to these experiments, we find, however, that there is agreement on the existence of a first-order transition. The basic quantitative difference here is that Käs and Sackmann report this transition from strong pears, whereas we find only a rather small *mean* asymmetry of the vesicles near the instability. A qualitative difference is that they report a well defined continuous symmetry-breaking transition at reduced volumes $v < 1$, which we do not find. In contrast, our vesicles are slightly asymmetric for all reduced volumes right up to the spherical shape ($v = 1$). In some sense, this difference is also quantitative, since it relies on a measurement of the degree of up/down asymmetry ("pearness") of the vesicles. We note that the interpretation of the data in [49, ?] was based on a measurement of reduced volumes only. The degree of asymmetry was judged visually from dynamically fluctuating vesicles or estimated from snapshots of vesicle shapes.

In Fig. 5.17, we have juxtaposed hypothetical values of the asymmetry parameter of the experimental sequence reported in [50] with those of our results. The degree of asymmetry of the last stable pears is estimated *roughly* from the pictures published in [50]. These pictures are *snapshots* of fluctuating vesicles but, as implicitly suggested by the authors, close to the mean shape of the vesicle under consideration. One observes that, for a second-order, transition one would have a bifurcation structure in $|\langle a_3 \rangle|$. In contrast, the

scaling behaviour of our $|\langle a_3 \rangle|$ is qualitatively completely different and not consistent with a bifurcation structure. Furthermore, an additional second-order transition, which would preempt the symmetry breaking of the first-order budding transition, should also show up in the behaviour of the soft mode. It would be expressed as a second apparent divergence in addition to the divergence at the spinodal line. Such a signature is also absent in our data (see Fig. 5.5). We conclude, therefore, that there is no real second-order transition detectable in our data. We also note that we consider it impossible unambiguously to detect a second-order transition for vesicle shapes without quantifying the degree of asymmetry and performing a scaling analysis.

We propose that it was the existence of weak *mean* pears, which are detectable by visual inspection only below a certain reduced volume, in combination with the large pear *fluctuations* near the spinodal line which led to the proposition of a second-order budding transition in [49, 50]. Thus, it is probably not so much the experimental results which are in contrast to our findings but rather their interpretation.

In summary, we note that our interpretation of the sequence of events found in this work might also be applicable to the experiments reported in [49, 50]. We find that a) budding is a first-order transition, b) it is a metastable *prolate* shape and not a (strong) pear which becomes unstable at the spinodal line, c) there is no additional second-order transition, and d) the reflection symmetry of the prolate phase is weakly broken by an extrinsic, unknown source of asymmetry, so the prolate phase of the ADE model appears experimentally as consisting of weak pears.

It is our belief that our interpretation gives a complete and internally consistent picture and has the merit of theoretical explanation within the ADE model. Regrettably, we have at present no strong evidence as to the origin of the asymmetry. We can only point out that visible "defects" are common, so it does not stretch credibility to suggest that such defects continue to exist at length scales below our resolution, where we cannot select against them.

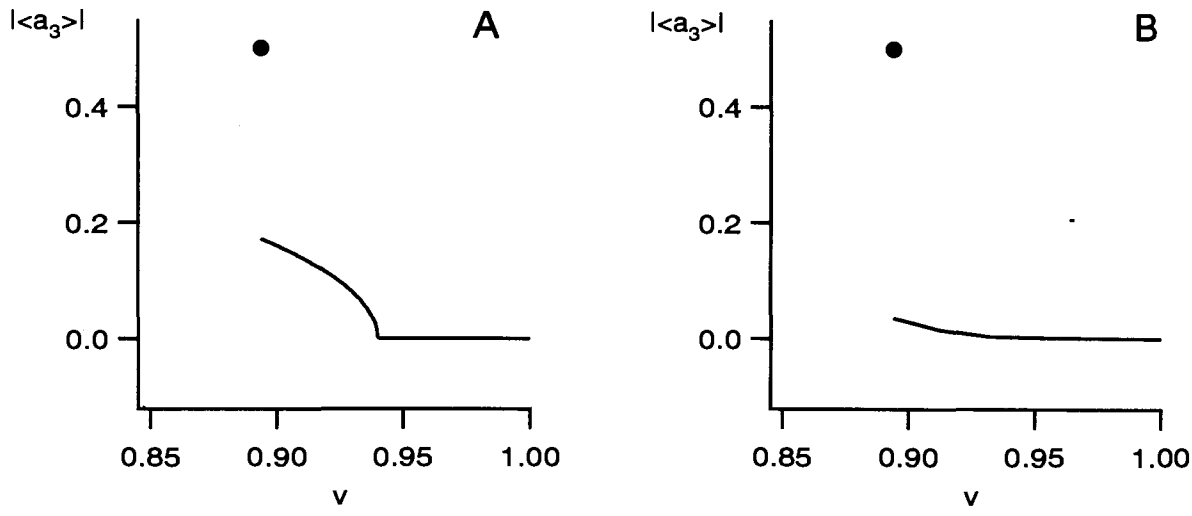

Figure 5.17: Two different scenarios for the budding transition. Scenario A corresponds to the results reported in [49, 50]. Scenario B corresponds to our findings. In both cases, there is a clear jump of the asymmetry at some finite reduced volume. In scenario B, the bifurcation structure corresponding to a second order transition is absent.

Chapter 6

Mapping of Prolate Vesicle Shapes into the ADE Phase Diagram

In the previous Chapter, we investigated qualitative signatures of budding behavior, especially the way in which the up/down symmetry is broken. In this work the focus was to study the static and dynamic vesicle fluctuations just prior to the budding instability leading from the prolate phase towards pear or vesiculated shapes, as monitored via the dominant asymmetry measure $|\langle a_3 \rangle|$. In this Chapter, by contrast, we focus on the finer details of the (mean) vesicle shape, as measured via the mean-shape amplitudes, $< a_n >$, within the prolate phase. In particular, we shall explore the extent to which these shapes can or cannot be accurately predicted/described within the context of the ADE model. Thus, the ultimate goal is to locate these shapes in the appropriate phase diagram and to see whether observed and predicted shapes agree, thereby "mapping" the observed shapes into the ADE phase diagram.

The ADE phase diagram is described (Sec. (2.4)) in terms of three parameters, the ratio α of elastic constants, the reduced volume v, and the effective bilayer area difference, $\overline{\Delta a_0}$, defined by

$$\overline{\Delta a_0} = \Delta a_0 + \frac{1}{2\pi\ \alpha} c_0 \ . \tag{6.1}$$

The first parameter, α, is characteristic of the lipid-solvent system and, thus, should be the same for all vesicles in a given (uniform) preparation. α may be measured independently of the shape experiments, e.g., from tether pulling experiments [74]. We have already discussed in Sec. 4.3.3, how to estimate the reduced volume v from the data. If Δa_0 and c_0 were directly measurable, [1] then the analysis would be straightforward: We would use

[1] Note that c_0 is, like α, characteristic only of the lipid-solvent system, while Δa_0 is in principle determined

Eq. (6.1) to compute $\overline{\Delta a_0}$ and then simply compare the measured shape with the shape predicted by the ADE model at that point in its phase diagram. Unfortunately, this is not possible, because neither Δa_0 nor c_0 can be measured directly. Luckily, it turns out that it is possible to infer $\overline{\Delta a_0}$ directly from the shape data. Thus, the significance of Eq.(6.1 is not that it allows calculation of $\overline{\Delta a_0}$ but that it provides information about the unknown quantities Δa_0 and c_0.

Of course, inference of $\overline{\Delta a_0}$ from the shape data requires the use of theory, thus risking making comparison between experiment and theory circular. We shall find, however, that the parameter which fixes $\overline{\Delta a_0}$ does not (in principle) exhaust the shape data. Furthermore, data from a thermal sequence of points and from the geometry of the eventual budding at the end of such a sequence provide additional and nontrivial comparisons between theory and experiment.

Finally, we note that the mapping (shape comparison) is complicated by thermal effects (fluctuations and thermal shifts) (see Sec. (6.6.1)), by gravitational deformations (see Sec. (6.6.2)), and by the small intrinsic up/down shape asymmetries (see Sec. (6.6.3)).

The next subsection outlines the theory by which we have extracted $\overline{\Delta a_0}$ from the shape data.

6.1 How to Infer the Effective Area difference $\overline{\Delta a_0}$ from Shape Data

The logic for extracting $\overline{\Delta a_0}$ from the shape data has two steps:

Within the context of the ADE model, there is a simple relation between $\overline{\Delta a_0}$ and the reduced area difference Δa, which is a geometrical quantity (hence, in principle, directly measurable). To start, recall the form of the ADE energy functional from Eq. (2.5),

$$E[\overline{\Delta a_0}; S] = G[S] + \frac{\alpha}{2}(\Delta a[S] - \overline{\Delta a_0})^2, \tag{6.2}$$

where we have used square brackets to indicate dependence on the full shape S. Note that $G[S] = (1/8\pi)\int da\,(c_1 + c_2)^2$ (which is just a dimensionless version of Eq. (2.4)) is independent of $\overline{\Delta a_0}$. The zero-temperature equilibrium shape minimizes Eq. (6.2) at fixed reduced volume v, thus leading to a ground-state energy function $E(\overline{\Delta a_0}, v)$. This minimization can be carried out sequentially [58]. First, we may imagine minimizing over all shapes with a given numerical value of the reduced area difference Δa. The second term

at vesicle closure and can vary from vesicle to vesicle of the same preparation.

in Eq. (6.2) does not change in this process. This restricted minimization defines an energy function $G(\Delta a, v)$ which is, in fact, the ground-state energy function of the pure ΔA-model. Subsequent minimization of the full ADE energy over the variable Δa leads to

$$\overline{\Delta a}_0 = \Delta a + \frac{\tilde{c}_0}{2\pi\alpha}, \tag{6.3}$$

where

$$\tilde{c}_0 = \tilde{c}_0(\Delta a, v) \equiv \frac{1}{2}\,\frac{\partial G(\Delta a, v)}{\partial \Delta a}. \tag{6.4}$$

If the function $G(\Delta a, v)$ is known, then Eq. (6.3) determines $\overline{\Delta a}_0$ implicitly, as a function of v and Δa. Note that, for fixed v, the minimum of $G(\Delta a, v)$ corresponds to $\tilde{c}_0 = 0$, so, at this point, $\overline{\Delta a}_0 = \Delta a(v)$, which is in general nonzero.

It will be useful to record here for future reference a remark about the general relation between the variables Δa and $\tilde{c}_0$. Note that the definition (6.4) makes $\tilde{c}_0$ the Legendre transform conjugate of Δa in the sense that the "potential,"

$$F = F(\tilde{c}_0, v) = \frac{1}{2}\,G - \tilde{c}_0 \Delta a\ , \tag{6.5}$$

has $\tilde{c}_0$ as its natural variable and satisfies

$$\frac{\partial F(\tilde{c}_0, v)}{\partial \tilde{c}_0} = -\Delta a(\tilde{c}_0, v). \tag{6.6}$$

Noting that F (in suitably reduced units) is just the energy of a pure spontaneous curvature model with the spontaneous curvature $\tilde{c}_0$, we conclude that $\tilde{c}_0$ is (in reduced form) just the spontaneous curvature which would be required in a pure spontaneous curvature model to achieve the (reduced) area difference Δa.

Now, in principle, inversion of Eq. (6.3) solves the problem of inferring the unknown quantity $\overline{\Delta a}_0$ from the experimental shape data (Δa). In practice, however, in the region of the phase diagram which we study, the shape variable Δa is ineffective, because (for reasons we shall make clear below) it has a very narrow effective range and cannot be measured from the video images with sufficient precision. It is, therefore, preferable to infer the conjugate variable $\tilde{c}_0$ directly from the experimental data in step one and then to use the relation (6.3) in the form,

$$\overline{\Delta a}_0 = \Delta a(\tilde{c}_0, v) + \frac{\tilde{c}_0}{2\pi\alpha}, \tag{6.7}$$

to find $\overline{\Delta a}_0$ in step two. This inference is achieved by comparing experimental values of the shape coefficient a_4 (Eq.(4.14)) with the results of calculations based on the pure SC model starting from the energy functional $F[S] = (1/8\pi)\int da\ (c_1 + c_2 - \tilde{c}_0)^2$, which is just a dimensionless version of Eq. (2.3) but with a spontaneous curvature $\tilde{c}_0$. In such

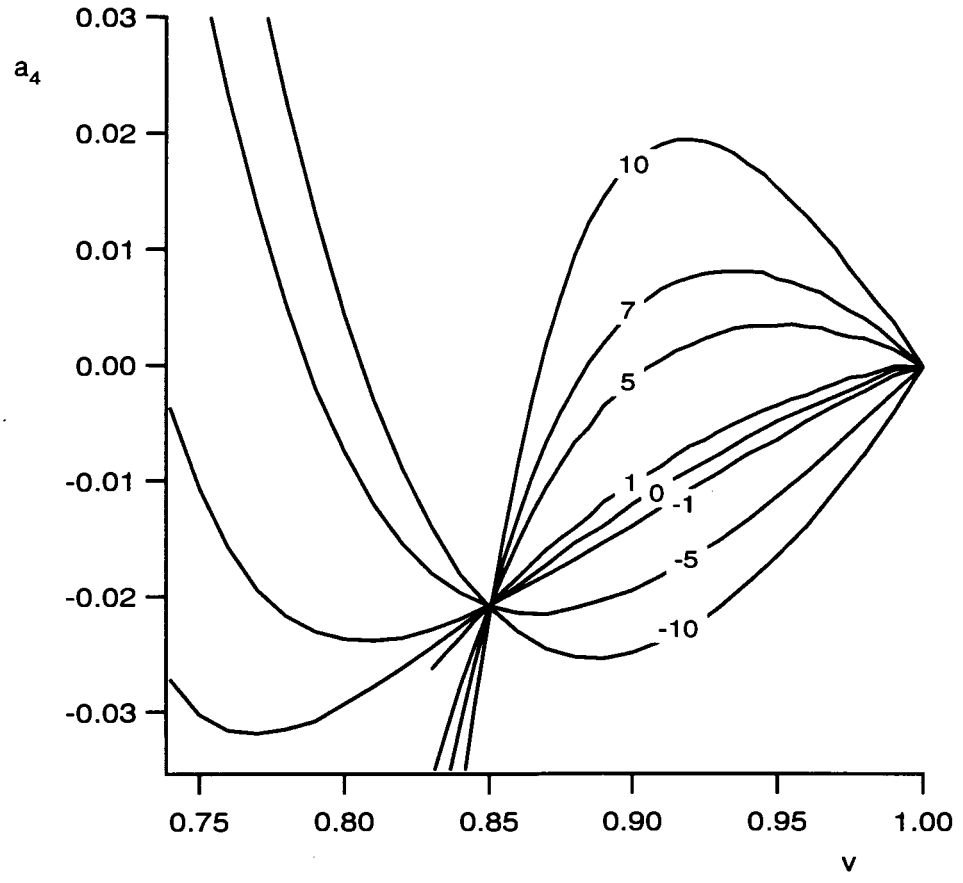

Figure 6.1: Dependence of the shape amplitude a_4 as a function of the reduced volume v on the value of the "spontaneous curvature" $\tilde{c}_0$. (Although a_4 is almost independent of $\tilde{c}_0$ at $v \simeq 0.85$, there is no common crossing point.) We have used this functional dependence to relate experimentally measured shapes (characterized by $(v \approx \langle v_e \rangle, \langle a_4 \rangle)$) to their theoretical counterparts (characterized by $(v, \tilde{c}_0)$).

a model, the equilibrium values of all physical quantities (like Δa, the shape coefficients $\{a_n\}$, etc.) depend only on v and $\tilde{c}_0$, so measurement of any one such variable at fixed v in principle determines $\tilde{c}_0$. In practice, for reasons which we shall explain more fully below, it is convenient to use the shape amplitude a_4.

The predicted dependence of a_4 on $\tilde{c}_0$ computed for the spontaneous-curvature model is displayed in Fig. 6.1. These results show that (except near reduced volume $v = 0.85$) a_4 is delicately dependent on $\tilde{c}_0$. Thus, given measured values of v and a_4 from the video images, we infer $\tilde{c}_0$ (numerically) from the dependence depicted in Fig. (6.1) and then use Eq. (6.3) to obtain $\overline{\Delta a}_0$. In fact, for v near unity Δa is a linear function of the reduced volume $1 - v$

and independent of $\tilde{c}_0$ to leading order,

$$\Delta a \approx 1 + \frac{1}{3}(1-v) + O(1-v)^{3/2}. \tag{6.8}$$

Thus,

$$\overline{\Delta a}_0 \approx 1 + \frac{1}{3}(1-v) + \frac{\tilde{c}_0}{2\pi\alpha}\ , \tag{6.9}$$

which shows that Eq. (6.3), which maps the experimental data, v and $\tilde{c_0}(a_4)$, into the ADE variable, $\overline{\Delta a}_0$, is approximately linear in this region of the phase diagram.

Since this mapping depends on the theory (which is in principle being tested), other data must be used to test consistency. In principle, the remaining shape coefficients, a_2, a_6, etc., contain independent data. In practice, these coefficients are not useful: a_2 effectively depends only on v; and, a_6, a_8, etc., are too small to be measured with precision. Thus, with our current precision, there are no additional data to provide cross-checks of the mapping. The only test of the correspondence between theory and experiment which a single, isolated data set can provide is whether or not the mapped point lands in a region of the ADE phase diagram where the (prolate) shape is predicted to be locally stable (see Sec. (6.5.1)). In Sec. (6.5.2), we show how, by using a single vesicle at a sequence of different temperatures, a test of the theory can be made.

6.2 Nearly spherical prolate shapes: The hierarchy

Before mapping the experimental data, it will be useful to devote a section to a detailed discussion of the shapes in the prolate region of the phase diagram near reduced volume $v = 1$. This discussion will serve to explain the special features of the mapping protocol outlined in the preceding section.

We start with discussion of the SC model based on the energy functional $F[S]$, as explained in the last section. The full ADE model is, in turn, related to the SC model via the mapping $\tilde{c}_0 \rightarrow \overline{\Delta a}_0$ defined by Eq. (6.3).

For nearly spherical shapes, we may use our representation Eq. (4.10),

$$\psi(s) = \pi\frac{s}{s^*} + \sum_{n=1}^{\infty} a_n \sin(n\pi\frac{s}{s^*})\ , \tag{6.10}$$

and imagine expanding all important shape functionals, $F[\tilde{C}_0, S], V[S], A[S]$, and $\Delta A[S]$, in the amplitudes $\{a_n\}$, where, in omitting the azimuthal variable (intrinsically absent in our representation) and setting $b_n = 0$, we have specifically restricted to axial symmetry. We

further simplify in what follows to up/down symmetric phases (like the prolate) for which the odd coefficients $\{a_{2n+1}\}$ vanish.

In the SC model, we are required to minimize $F[\tilde{c_0}; S[s^*, \{a_n\}]]$ at fixed values of $V[S]$ and $A[S]$. Note that the functionals have a dependence on the length scale s^*. However, it is not hard to show [73] that the results can only depend on the reduced variables v and $\tilde{c}_0$, so that the length scale s^* drops out and the problem reduces to minimization of a function, $f(\tilde{c}_0, \{a_n\})$, of dimensionless variables at fixed reduced volume, [2]

$$v = 1 - \frac{64}{135}a_2^2 + \frac{1024}{4725}a_2 a_4 - \frac{45056}{118125}a_4^2 + \cdots . \tag{6.11}$$

This minimization problem involves an infinite number of degrees of freedom and is, in general, very complicated; however, an important simplification takes place near the sphere point, $v = 1$, where the problem lends itself to expansion in the small parameter,

$$(1 - v)^{\frac{1}{2}}. \tag{6.12}$$

The form of the result is

$$\begin{aligned} a_2 &= A_1\,(1-v)^{\frac{1}{2}} + \{B_1\tilde{c}_0 + B_2\}\,(1-v) \\ a_4 &= \{B_3\tilde{c}_0 + B_4\}\,(1-v) \\ &\textit{etc.}, \end{aligned} \tag{6.13}$$

where the A_i and B_i are numerical coefficients given in App. A. Note that the amplitudes decrease systematically as $a_{2n} \sim (1-v)^{n/2}$, producing a "hierarchical" structure, which will play an important role in what follows. The hierarchical structure of the modal expansion of an equilibrium vesicle shape near the sphere was first noted by Ling Miao in [57, 58], who performed calculations for a prolate vesicle [3] within the spontaneous curvature model using a spherical-harmonic expansion of the vesicle shape. In App. A, we recall these earlier results and relate our shape representation to that of [58], thus showing that the amplitudes (6.13) of our representation inherit the hierarchical structure.

We are now in a position to investigate the special features of the mapping procedure outlined in the last section. Let us note first that the a_2 amplitude is independent of $\tilde{c}_0$ to first order in the small quantity $(1-v)^{1/2}$,

$$a_2 = \sqrt{\frac{135}{64}(1-v)} + O(\,(1-v)^1\,)\,. \tag{6.14}$$

Thus, due to the hierarchy, the stationary shape of a nearly spherical prolate vesicle is determined to leading order simply by the reduced volume v. The shape becomes dependent

[2] All expansions given in this Section have been obtained with the program Mathematica ©.

[3] The only other possible stable shape near the sphere is an oblate

on $\tilde{c}_0$ only in the next higher order in the reduced volume. This feature is also manifest in the expansion of the reduced area difference,

$$\Delta a = 1 + \underbrace{\frac{64}{405}\, a_2^2}_{(1-v)^1} + \underbrace{\frac{18176}{127575}\, a_2^3 - \frac{1024}{141175}\, a_2 a_4}_{(1-v)^{3/2}} \quad + \quad O(\,(1-v)^2\,)\,. \qquad (6.15)$$

Taking $a_2 = \sqrt{\frac{135}{64}(1-v)} + O(\,(1-v)^1\,)$ and $a_4 \sim O(\,(1-v)^1, \tilde{c}_0)$, one finds that a (linear) dependence on $\tilde{c}_0$ arises only at second order in $(1-v)^{1/2}$ via the dependence on a_4 ,

$$\Delta a = 1 + \frac{1}{3}\,(1-v) + (\,\underbrace{\frac{71}{630}}_{\simeq 0.11}\,(1-v) - \underbrace{\frac{128}{4725}}_{\simeq 0.03}\, a_4\,)\,\sqrt{15}\,(1-v)^{\frac{1}{2}} \quad + \quad O(\,(1-v)^2\,). \quad (6.16)$$

It is evident from Eqs. (6.14) and (6.16) why a_2 and Δa are poor candidates for extracting the parameter $\tilde{c}_0$ from the experimental shape data. The dominant part of both these variables does not depend on $\tilde{c}_0$. Thus, it is best to use the amplitude a_4 to deduce $\tilde{c}_0$, because (a) the dependence on $\tilde{c}_0$ appears in leading order and (b) a_4 is the largest amplitude with this property, since the amplitudes of higher modes are progressively smaller due to the hierarchy.

Eqs. (6.13) demonstrate the hierarchical structure of the ADE mode amplitudes for nearly spherical prolate shapes. It turns out numerically that this structure persists, even for quite strongly nonspherical, "deflated" shapes. In Fig. 6.2, the first three nonvanishing mode amplitudes are shown as a function of the reduced volume v for $\tilde{c}_0 = 0$. These amplitudes are obtained by expanding (numerical) solutions [4] to the Euler-Lagrange shape equations which express the minimization of the bending energy functional (6.2) [58]. Note that the amplitude of mode $2n$ remains roughly one order of magnitude larger than the amplitude of mode $2(n+1)$, down to at least $v \sim 0.8$.

One might expect from "order counting" in the hierarchy that the $\tilde{c}_0$ sensitivity of a_4 and of the second order term, $(a_2 - A_1\,(1-v)^{1/2})$, in a_2 would be comparable. Numerically, this turns out not to be so. Fig. (6.3) illustrates these sensitivities by plotting the differences, $a_{2n}(\tilde{c}_0 = +5, v) - a_{2n}(\tilde{c}_0 = -5, v)$, for the three lowest nonvanishing mode amplitudes. It is remarkable how little the second mode changes with $\tilde{c}_0$. Although the mean amplitude of the second mode has the largest numerical value of all amplitudes and can, thus, be measured with high accuracy, it contains hardly more experimental information than the value of the reduced volume. Therefore, one is forced to extract $\tilde{c}_0$ from measurements of the next smaller amplitude, a_4.

[4] We are grateful to Dr. Udo Seifert for providing the source code of his shape-finding algorithm.

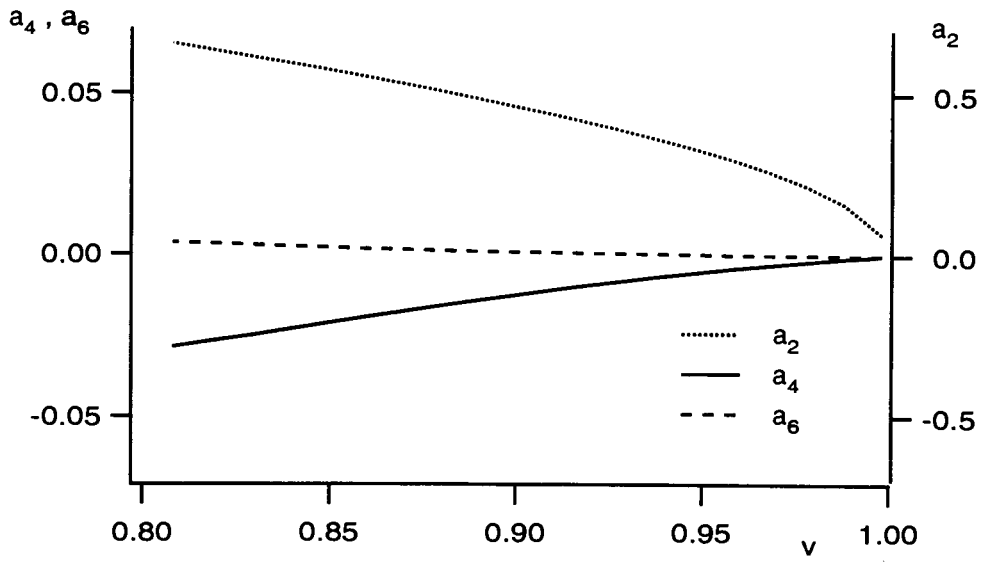

Figure 6.2: The mode hierarchy. Numerically calculated prolate shape amplitudes $a_{2n}(\tilde{c}_0 = 0, v)$ for the SC model. Note the different vertical scales.

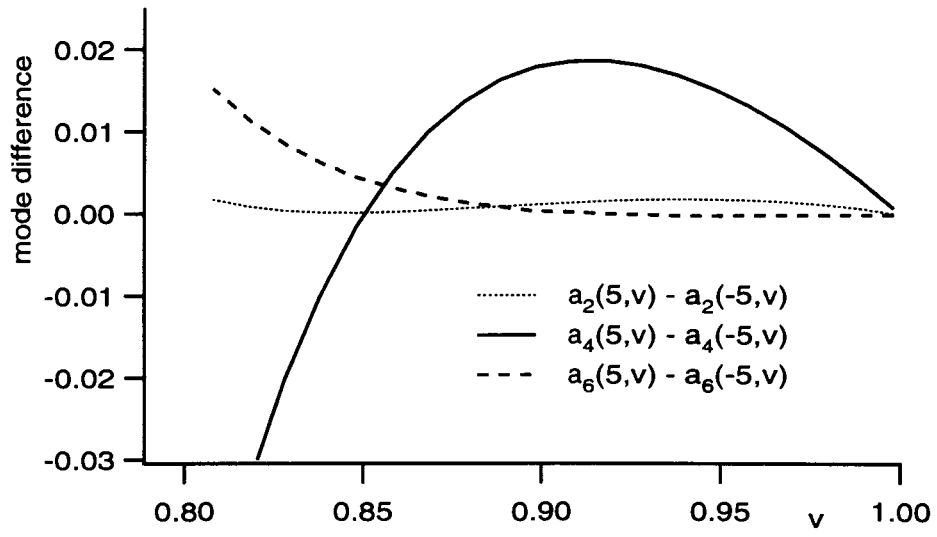

Figure 6.3: Mode amplitude differences for $\tilde{c}_0 = \pm 5$ for the SC model, illustrating the effect on the shape of changing the spontaneous curvature $\tilde{c}_0$ at fixed v. Note that a_2 is nearly independent of $\tilde{c}_0$.

In summary, as a consequence of the amplitude hierarchy which holds for prolate vesicles not too far from the sphere, the general connection Eq. (6.7) between the control parameters $\overline{\Delta a_0}$ of the ADE model and $\tilde{c}_0$ of the corresponding SC model is [5]

$$\overline{\Delta a_0} = 1 + \frac{1}{3}(1 - v) + \frac{\tilde{c}_0}{2\pi\alpha} + O(1 - v)^{3/2}. \tag{6.17}$$

Thus, the protocol for extracting data from the experiments is to measure the mean shape amplitude $\langle a_4 \rangle$ and the reduced volume v, which we approximate by $\langle v_e \rangle$ (see the discussion in Sec. (4.3.3)). We then infer $\tilde{c}_0$ from $\langle a_4 \rangle$ via Fig. (6.1) and use Eq. (6.7) (which is shown to be approximately linear by Eq. (6.17) above) to find $\overline{\Delta a_0}$.

6.3 Experimental Resolution

This section discusses the accuracy and reproducibility with which the phase-diagram parameters v and $\overline{\Delta a_0}$ can be derived from the experimental data, i.e., the "resolution" of the mapping of the experimental shapes into the phase diagram. This resolution will depend in detail on what region of the phase diagram is being studied; however, to get an idea of what can be achieved, let us look at derived values of v and $\overline{\Delta a_0}$ at two closely spaced reduced volumes in the prolate regime. At each volume, three measurements have been done which are visible as clusters in Figs. (6.4) and (6.5). For each point, we have averaged $N \approx 500$ contours. After performing the first set of three measurements during which the temperature had been kept constant, the temperature was raised 2.4 °C in order to decrease the reduced volume by $\Delta v = 0.01$.

As can be seen in Fig. (6.4), the resolution in reduced volume is very high. (Note the scale!) Since we normally use about $N = 1500$ contours for each measurement (i.e., more than in the figures above), we may expect that the uncertainty in v is well below 0.001. [6] Thus, two vesicle shapes with reduced volumes which are $\Delta v = 0.01$ apart can be easily distinguished. In the following, we omit error bars for the reduced volume, since they would be hardly visible on the scale of the plots we are going to discuss.

As has been discussed at length in the last two Sections, the value of the effective area difference $\overline{\Delta a_0}$ is derived in a two-step, one-to-one mapping from the average amplitude

[5] We can use this equation to find the minimizing shape amplitudes for the ADE model. In this regard, we have to express the parameter $\tilde{c}_0$ as a function of $\overline{\Delta a_0}$; to the order the amplitudes are given in Eq. (6.13), it is sufficient to approximate the differential area with unity to obtain $\tilde{c}_0 = 2\pi\ \alpha\ (\overline{\Delta a_0} - 1) + O(1 - v)$. Inserting this expression into Eq. (6.13), we get the minimizing shape amplitudes a_2 and a_4 in terms of the parameters of the ADE model.

[6] For vesicle shapes which are very close to the sphere, i.e., $v > 0.99$, the resolution is diminished. This is mainly due to the fact that the vesicles undergo prolate-oblate shape fluctuations in this regime.

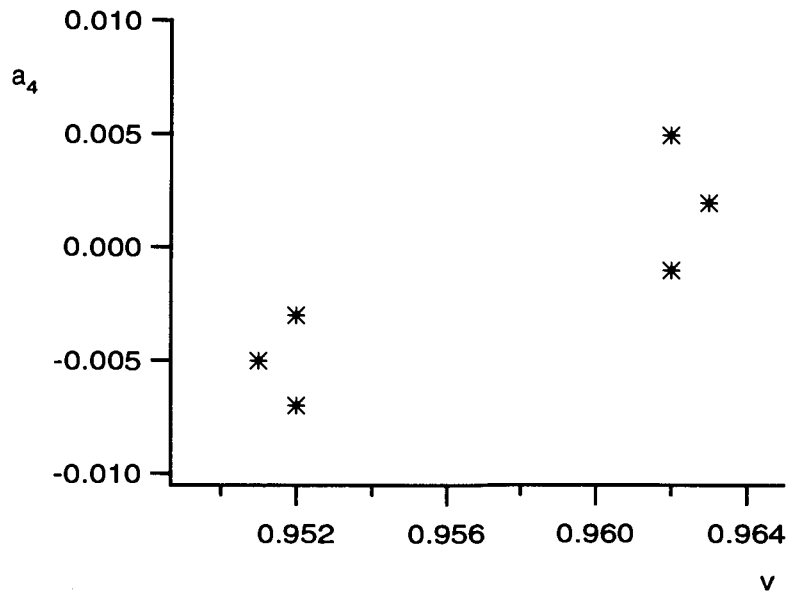

Figure 6.4: Repeated measurements of $(\langle a_4 \rangle, \langle v_e \rangle)$ under identical conditions. The two clusters represent two distinct temperatures, which differ by $\Delta T = 2.4$ °C and correspond to a difference $\Delta v = 0.01$ in reduced volume. The spread in each cluster is indicative of the experimental uncertainties (see text).

$\langle a_4 \rangle$. Thus, the resolution in $\overline{\Delta a}_0$ is directly dependent on the scatter of $\langle a_4 \rangle$, which is on the order of $\pm$ 0.001, as can be deduced from Fig. 6.4. In Fig. 6.5, the derived values of $\tilde{c_0}(\langle a_4 \rangle)$ and $\overline{\Delta a}_0(\tilde{c_0})$ are shown. Although the parameter $\tilde{c_0}$ is obtained numerically from the amplitude $\langle a_4 \rangle$ (as will be done in all further analysis), as described in Sec. 6.1, we have chosen, for the illustration in Fig. 6.5 (only!), to approximate the effective differential area by the formula $\overline{\Delta a}_0 \approx 1 + \tilde{c}_0/(2\pi\ \alpha\ )$ (see Eq. (6.17). Using this simple scaling relation (which is exact in the spherical limit) allows $\tilde{c_0}$ and $\overline{\Delta a}_0$ to be shown within one plot with two axes and, thus, illustrates the order of magnitude relation of both quantities for $\alpha = 1.4$. In the actual presentation of the data, we will refer to the full Equation (6.7). The scatter in $\langle a_4 \rangle$ translates into a resolution in $\tilde{c_0}$ of approximately ± 1. The resolution in $\overline{\Delta a}_0$ depends on α, of course. For large α, the absolute resolution in this quantity becomes very large. This just reflects the fact that the region of the phase diagram in which stable prolate shapes exist becomes very small [51]. [7] Of course, the relative resolution stays the same.

[7] In the limit $\alpha \to \infty$, the ADE model reduces to the ΔA model, where $\Delta a \equiv \Delta a_0$. Since, to linear order in $(1 - v)$, the geometrical quantity Δa is independent of $\tilde{c_0}$ (see Sec. 6.2), the shapes of vesicles with equal reduced volumes v but different spontaneous curvatures $\tilde{c_0}$ do not deviate much from each other. We note that this is a direct consequence of the hierarchy.

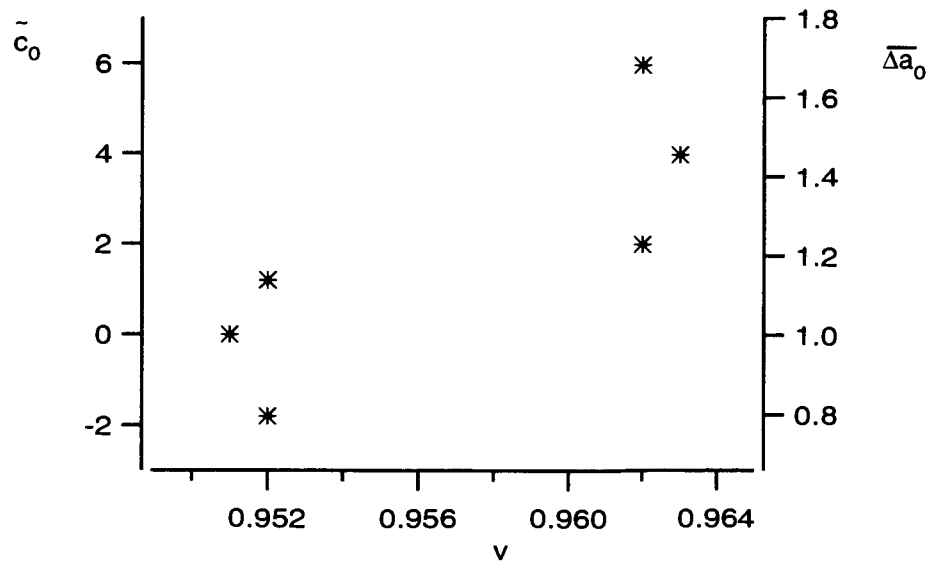

Figure 6.5: Derived values of $\tilde{c_0}$ and $\overline{\Delta a}_0$, based on the data of Fig. (6.4). The spread in each cluster gives a measure of the experimental uncertainties.

We conclude this Section with a remark on the delicate shape discrimination which is necessary in order to resolve the prolate near-spherical region of the (shape) phase diagram. Vesicle shapes change in a very delicate manner as parameters of the models are changed. Consider, for example, the overall, pole-to-pole distance d, measured along the symmetry axis for a vesicle of fixed volume, characterized by $R_V = 10\ \mu$m at a reduced volume $v = 0.9$. Within the SC model, this distance may then be regarded as depending on the single control parameter $\tilde{c_0}$. Taking as a reference the value of d for $\tilde{c_0} = 0$, Fig. 6.6 plots the variation Δd as $\tilde{c_0}$ changes. As can be read off from Fig. 6.6, changing $\tilde{c}_0$ from zero to one increases d by only 22 nm! This number (the smallness of which is a direct consequence of the hierarchy) is below the *local* lateral resolution of the contour (see Sec. 4.1.1). At first sight, it seems very astonishing that such a small number can be measured at all reliably. How can this be done? First, one has to realize that one does not measure only a single distance. Instead, the amplitudes are calculated *globally* from an integral over the different contours (see Eq. (4.14)), which deviate consistently from a reference shape over the whole length of typically about 600 contour points. Second, one is interested in a low mode, which is insensitive to local perturbations in the membrane. And, third, the amplitudes are averaged over typically $1-2\ \times 10^3$ contours. This amounts to an effective sampling size on the order

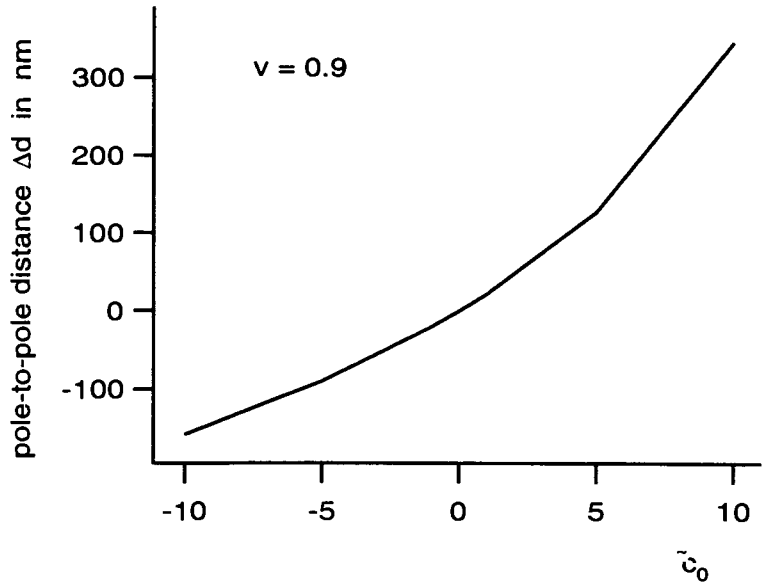

Figure 6.6: Theoretical differential pole-to-pole distances of a vesicle with $R_V = 10\mu m$ at reduced volume $v = 0.9$ as a function of $\tilde{c_0}$. The reference distance is taken for $\tilde{c}_0 = 0$.

of 10^5. Thus, shape differences on the 10 nm scale are detectable.

6.4 Thermal Trajectories in the Phase Diagram

By measuring the sequence of shapes assumed by the same vesicle as its temperature is changed, it is possible to explore systematic effects. As temperature changes, the control parameters change together in a systematic way, thus tracing a "thermal trajectory" through the appropriate phase diagram. The phase diagram is described in terms of the control parameters reduced volume v and the reduced effective area difference $\overline{\Delta a_0}(v)$. We recall the definitions,

$$\overline{\Delta a_0}(T) = \underbrace{\frac{\Delta A_0(T)}{8\pi D(T) R_A(T)}}_{\Delta a_0} + \frac{1}{2\pi\ \alpha}\ \underbrace{R_A(T) C_0}_{c_0}, \tag{6.18}$$

$$v(T) = \frac{R_V^3}{R_A^3(T)}, \tag{6.19}$$

where $R_A = (A/4\pi)^{1/2}$ and $R_V = (3V/4\pi)^{1/3}$ are the area- and volume-equivalent radii of the vesicle, respectively. D is the thickness of the bilayer, and ΔA_0 is the unscaled relaxed area difference of the two monolayers of the bilayer, as defined in Sec. (2.1). The intrinsic

spontaneous curvature C_0 of the membrane is also given in unscaled form for clarity.

In writing Eq. (6.18), we have assumed that the ratio of the elastic constants α, and the parameters C_0 and R_V are temperature independent. Although the assumption of temperature independence for C_0 and α is mostly ad hoc, [8] the temperature independence of R_V does have an experimental justification: The volume expansivity of the aqueous solution enclosed by the vesicle is much smaller than the membrane area expansivity. Typical numbers are $\beta_V(\mathrm{H_2O}) \simeq 3 \times 10^{-4}/\mathrm{K}$ and $\beta_{A_0}(\mathrm{SOPC}) \simeq 3 \times 10^{-3}/\mathrm{K}$. Thus, to a good approximation, we may safely ignore volume expansion effects.

The remaining variables in Eqs. (6.18) and (6.19) are all distances or areas and may be characterized in terms of thermal expansivities,

$$\beta_X = \frac{1}{X}\frac{dX}{dT}, \tag{6.20}$$

where $X = A_0^{\mathrm{ex}}, A_0^{\mathrm{in}}, A_0$, or D. The temperature dependence of Δa_0 is simplified by the fact that the *bilayer* volume DR_A^2 stays effectively constant [57], i.e., the thermal expansivity of the bilayer thickness is given by $\beta_{\mathrm{D}} \sim -\beta_{\mathrm{A_0}}$. If we make the assumption that $\beta_{A_0} = \beta_{A_0^{\mathrm{ex}}} = \beta_{A_0^{\mathrm{in}}}$, and set $c_0 = 0$, then we arrive (see below) at a particularly simple form for the trajectory, Eq.(5.2),

$$\overline{\Delta a}_0(T) = \frac{\Delta a_0^s}{v(T)}, \tag{6.21}$$

which we have already stated in Sec. 5.1. Here, $\Delta a_0^s \equiv \Delta a_0|_{v=1} = \overline{\Delta a}_0|_{v=1}$. In this form, the possible trajectories are a one-parameter family of curves determined by the reduced area difference of the spherical vesicle Δa_0^s. This quantity is initially set at the time of vesicle closure, during swelling. [9] An area excess with respect to the sphere on the outer monolayer, e.g., leads to a numerical value of Δa_0^s larger than unity. The larger the parameter Δa_0^s is, the higher up in the phase diagram (Fig. (5.1)) are thermal trajectories shifted and the sooner (with respect to temperature increase) a vesicle will bud.

This simple form, Eq. (6.21), of the trajectory assumes (a) a vanishing spontaneous curvature and (b) equal thermal expansivities for the inner and outer monolayers. The first assumption is strictly true only if the leaves of the bilayer and the inner and outer aqueous environments are chemically identical. Since we work with a sucrose/glucose solution, it is presumably not valid. The second assumption should hold for the pure SOPC membranes of our experiments. However, due to the different interaction between the sugar molecules

[8] One may argue that thermal effects on C_0 and α are negligible in comparison to the thermal area expansion. However, this is by no means evident. For simplicity, we take C_0 and α as temperature independent.

[9] On long time scales (e.g., several hours), there is presumably a small amount of lipid flip-flop between the monolayers or lipid degradation which may change Δa_0^s (see the comment at the end of this section).

in the inner and outer solution and the lipid headgroups, [10] it is possible that there may be some small difference between the inner and outer thermal expansivities. This observation may be especially important, since it was pointed out by Berndl et al. [49] that the area difference ΔA_0 is potentially very sensitive to differences in the thermal expansivity of the inner and outer monolayers. This sensitivity arises because of the large ratio of the typical radius of curvature to the membrane thickness $R_A/D \simeq 10^3$; and, it has the result that a small amount of additional area has a large effect on the (relaxed) integrated mean curvature $\Delta A/(2D)$. Let us, therefore, explore the consequences of different thermal expansivities of the outer and inner membrane leaflets. In this connection and following Refs. [49, 51], we define an asymmetry parameter γ,

$$\beta_{A_0^{ex}} = (1+\gamma)\beta_{A_0^{in}} \ . \tag{6.22}$$

Seifert et al. [51] derived an equation for the behavior of $\overline{\Delta a}_0(T)$ with a nonzero asymmetry parameter under the simplifying assumption of constant thermal expansivities and $C_0 = 0$. Generalizing their treatment to non-zero values of C_0, we find

$$\overline{\Delta a}_0(v) = v^{-r}\ (\Delta a_0^s + b(v^{-\gamma q} - 1)) \ + \ \frac{c_v}{2\pi\ \alpha}\ v^{-\frac{1}{3}} \ , \tag{6.23}$$

where the exponents are given by $r = (2-\gamma)/(2+\gamma)$ and $q = 3/(2+\gamma)$. The scaled relaxed area difference Δa_0^s and the coefficient $b \equiv A_0^{ex}/(8\pi\ DR_A) \simeq \frac{1}{2}\frac{R_A}{D}$ are evaluated at the spherical vesicle shape. Finally, $c_v = C_0 R_V$ is the spontaneous curvature scaled by the volume-equivalent radius, as is appropriate for a parameter of a thermal trajectory which keeps the vesicle volume constant. From the intermediate steps of the derivation only the temperature variation of the reduced volume is given here for reference,

$$\frac{dv}{dT} = -\frac{3}{2}\beta_A v \ + O(\gamma). \tag{6.24}$$

Although the coefficient $b \simeq 500$ is a large quantity, the thermal asymmetry $\gamma < 0.01$ is expected to be a small number. Therefore, one can simplify the expression (6.23) by expanding in powers of γ up to first order, thus reducing the number of free parameters to three. Defining those parameters as

$$\begin{aligned} t_1 &= \Delta a_0^s \ , \\ t_2 &= \frac{c_v}{2\pi\ \alpha} \ , \\ t_3 &= (\Delta a_0^s - \frac{2}{3}b)\gamma \ \simeq \ -\frac{2}{3}\ b\gamma \ , \end{aligned} \tag{6.25}$$

[10] Such an interaction might arise due to the different steric structure of the OH-groups of the sugars sucrose and glucose [75]. The dipole moments of the sugar molecules should interact differently with the dipole of the choline head.

we arrive at the linearly parameterized trajectories,

$$\overline{\Delta a_0} = t_1 \frac{1}{v} + t_2 \frac{1}{v^{1/3}} + t_3 \frac{\ln(v)}{v} + O(\gamma^2). \tag{6.26}$$

The last term vanishes at $v = 1$, so the sum of the first two parameters $(t_1 + t_2)$ measures the effective area difference, $\overline{\Delta a_0}|_v = 1$, of the spherical vesicle. Note that the intrinsic spontaneous curvature c_v is only determined via t_2, when α is measured independently. The third parameter t_3 gives a measure of the thermal asymmetry. We will explore in the next Section the extent to which this linear model of thermal trajectories is consistent with the data.

The derivation of this temperature trajectory contains an implicit assumption. In all of the above arguments, the difference ΔN in the number of molecules of the inner and outer monolayers is assumed to remain constant during experiments. If it does not, the notion of a thermal trajectory makes no sense. The area difference, $\Delta A_0 = a^{in}_{lipid} N^{in} - a^{out}_{lipid} N^{out} \simeq \overline{a_{lipid}} \Delta N$, could change (and, in fact, does so slightly over the time course of several hours) due to lipid flip-flop or lipid degradation, in addition, of course, to whatever change it may have due to thermal expansion. Therefore, care has to be taken when using Eq. (6.26) for analysis of experimental trajectories which were obtained over an extended time period.

6.5 Budding Trajectories: Experimental Results and Discussion

In this Section, experimental results on thermal trajectories which lead to budding will be presented. As we have seen, the mapping of an experimental mean shape into the ADE phase diagram is a two step process. One first determines the parameters $(\tilde{c}_0, v)$ of the shape. This step is independent of α. Then, the shape is mapped into the phase diagram for some fixed value of α. Accordingly, experimental data are first given in the $(\tilde{c}_0, v)$ diagram in Sec. 6.5.1. Then, in Sec. 6.5.2, we discuss trajectories in the full ADE phase diagram.

6.5.1 Trajectories in the $(\tilde{c}_0, v)$ diagram

In this Section, we present the shape data in a form which is independent of α. In Fig. 6.7, experimental trajectories for three different vesicles are given in the $(\tilde{c}_0, v)$ diagram. Presentation of the data in this way provides two levels of consistency test. First, it is obviously possible to find a $\tilde{c}_0$ which reproduces the observed a_4, i.e., the experimentally

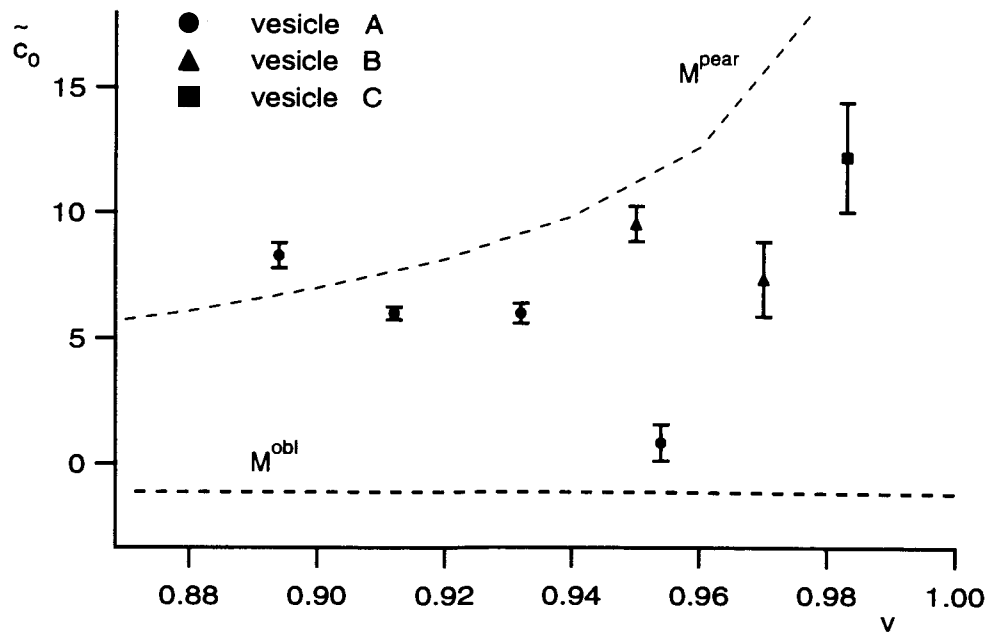

Figure 6.7: Experimental trajectories in the $(\tilde{c}_0, v)$ diagram approaching the budding transition. With the exception of one point, all experimental prolate shapes are correctly mapped into the (meta) stable prolate region of the shape parameters $(\tilde{c}_0, v)$. This region is bounded by the two dashed spinodal lines. Above the upper spinodal line (M^{pear}), vesicles are unstable to budded shapes. Below the lower spinodal line (M^{obl}), vesicles are unstable to oblate shapes. Trajectories are depicted for three different vesicles. Note that the trajectories approach the spinodal line along paths of increasing $\tilde{c}_0$ as expected by theory. The uncertainty in reduced volume (± 0.001) is well below the size of the data symbols. The experimental error in $\tilde{c}$ is much larger and increases for $v \to 1$. This is because the available shape space becomes very small in this quasi-spherical region.

found shapes exist as extremal points of the Euler-Lagrange Equations. That in itself is experimentally not trivial considering the extremely small shape differences alluded to in Sec. (6.3). After all, we could have found c_0-values which are completely out of line, e.g., $c_0 = 100$. Second, finding a shape does not guarantee its stability, i.e., there are stationary prolate shapes which are unstable. We have included the two spinodals (M^{pear}, M^{obl}) of the prolate phase in Fig. 6.7. [11] Prolate vesicles outside the region between these two lines (i.e., those which exist beyond the spinodals) are in principle unstable. They would either bud (at the upper spinodal) or transform into an oblate shape (at the lower spinodal). It is important to note in this respect that the region of stability of prolate shapes is independent

[11] We thank Ling Miao and Marija Nikolic for providing the numerical data for these lines.

of α. [12] Thus, prolate mean vesicle shapes observed in experiment should map into the theoretical region of (meta) stability of the prolate phase in the $(\tilde{c}_0, v)$ diagram. Indeed, except for one point, they are all nicely sandwiched between the upper and lower spinodal line, as they should be. Even more so, we have never observed stable shapes with absolute a_4 amplitudes larger than (roughly) 0.02, which would correspond to large positive or negative $\tilde{c}_0$ (see Fig. (6.1)). Thus, prolate shapes do, indeed, exist only in a (very) small region in the space of all possible shapes, as one would expect from the hierarchical structure of the shape amplitudes. The absence of experimental vesicle shapes outside this region is quite a stringent – though indirect – test of the ADE model. This is the main experimental result of this Chapter.

The one "bad" point of vesicle "A" deserves further comment. The reduced volume $v_b = 0.878 \pm 0.001$ at which budding took place for this vesicle has been determined in Sec. (5.4.1) by extrapolation to the budding temperature. Thus, assuming the trend in the trajectory continues, the last metastable shape of vesicle "A" (which we did not measure) is placed even further into the theoretically unstable region. In contrast, vesicle "B" did bud near the spinodal with a reduced volume $v = 0.942 \pm 0.002$. Vesicle "C" budded from the point shown in the figure, which is located quite far away from the spinodal within the prolate region. Therefore, we conclude that, although the last (meta)stable shapes measured do qualitatively follow the trend of the spinodal line, some of them seem to be quantitatively misplaced. [13] It is not clear at present, where this distortion comes from. It cannot result from a false mapping between the parameter $\tilde{c}_0$ and the amplitude a_4, since this is a one-to-one correspondence. However, the assumption (which went into this mapping) that the mean experimental shape represents an axisymmetric $T = 0$ shape, as calculated from the ADE model, may be not quite valid. Indeed, both finite-temperature effects, which tend to make the vesicles more spherical, and the partial flattening of the vesicles induced by gravity were ignored. These points will be further discussed in Sec. 6.6.

[12] An instability to a shape with the same symmetry depends on α [68]. Since the reflection symmetry of the prolate shape is broken along the spinodal lines depicted in Fig. (6.7), these lines do, indeed, form the boundary of the stable prolate region of the ADE model.

[13] We note that the region of instability along the spinodal line is fuzzy, as discussed in Sec. (5.2.1). Thus, it is, in principle, consistent with theory that vesicle "C" budded from within the prolate region. (In order to determine the fuzzy region more quantitatively, i.e., to estimate the mean escape times from the metastable states, one would have to know the contour lines of constant activation energy for the decay. Unfortunately, we do not yet have this information available.) Of course, a metastable state beyond the spinodal is not possible.

6.5.2 Trajectories in the ADE Phase Diagram

Let us proceed, nevertheless, to a discussion of a thermal trajectory in the ADE phase diagram, keeping in mind possible artifacts introduced by the (somewhat naive) interpretation of mean experimental shapes as zero-temperature axisymmetric objects. In Fig. 6.8, the experimental trajectory of vesicle "A" is shown for $\alpha = 1.4$, the estimated value for a single walled SOPC vesicle. In Fig. 6.9, the same vesicle trajectory is depicted for $\alpha = 6.4 = 4\times 1.4$, which is the minimal value of α for a double-wall vesicle.

The feature most obvious, when comparing Figs. 6.8 and 6.9, is that the position of the experimental trajectory relative to the spinodal line of the budding transition does not change with α. The data points (and the spinodal line) are just scaled differently by the mapping (6.3). However, the position with respect to the limiting line *does* change. [14] This behaviour allows us to set an upper limit for α: For $\alpha = 6.4$, vesicle "A" should have had an open neck right after the budding instability at $v_b = 0.878 \pm 0.001$, since at this reduced volume the spinodal line $\mathrm{M}^{\mathrm{pear}}$ is located well below the limiting line $\mathrm{L}^{\mathrm{pear}}$. However, in fact, the neck did close down completely, as one would expect for smaller values of α. From Fig. 6.9, we infer, therefore, that $\alpha < 6.4$. Indeed, noticing that the value of v_b is numerically almost equal to the reduced volume of the crossing point of the spinodal line with the limiting line for $\alpha = 1.4$ in Fig. 6.8, we deduce $\alpha \leq 1.4$, which is an even better estimate. Note that this conclusion is independent of the values of $\overline{\Delta a_0}$. It relies only on measurements of the reduced volume.

More generally, a comparison of the budded shape to the metastable shape allows in principle even a measurement of α . [15] However, the region of the phase digram which lies beyond the limiting line is as yet theoretically unexplored, and we refrain from such an analysis.

The lines in Figs. 6.8 and 6.9 are obtained by fitting the trajectories to various variants of the linear model (6.26). In Tab. 6.1, the result of three restricted fits for the two different α values explored are shown. One notices that the results of the fit depend on α as expected. In addition, the experimental errors become smaller for larger α. This reflects the fact that the region of stable prolate shape gets increasingly narrow as $\alpha \to \infty$, as already noted. We will concentrate in the detailed discussion which follows on the most "likely" case, $\alpha = 1.4$, which is the one we would expect to apply to vesicle "A" according to the experimental

[14] The crossing point of the upper spinodal line with the limiting line moves toward $v = 1$ as $\alpha \to \infty$. This property follows from Eqs. (6.3) and (5.1).

[15] At the spinodal line the two shapes have the same value of $\overline{\Delta a_0}$. Applying the mapping 6.3 to both of them one finds $\alpha = \frac{1}{2\pi}(\tilde{c}_0^{\mathrm{pro}} - \tilde{c}_0^{\mathrm{bud}})/(\Delta a^{\mathrm{bud}} - \Delta a^{\mathrm{pro}})$.

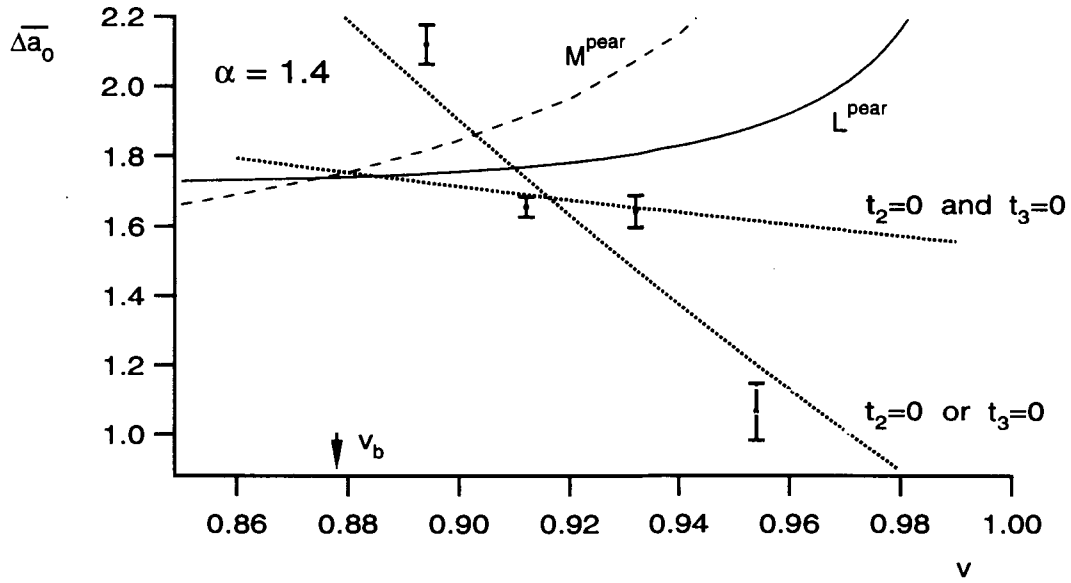

Figure 6.8: Trajectory of vesicle "A" for $\alpha = 1.4$ in the ADE phase diagram. The lines M^{pear} and L^{pear} depict the spinodal and the limiting line, respectively. The spinodal line marks the limit of stability of the (*meta*) stable prolate shapes. The limiting line is the boundary of (*stable*) pear or budded shapes with an open neck. Beyond this line, the neck of the bud is fully closed. Vesicle "A" budded at a reduced volume $v = v_b$, which is close to the crossing point of M^{pear} and L^{pear}. Indeed, we find complete closing of the neck in this vesicle. Note that the relative location of the experimental data to the spinodal line in the $(\tilde{c}_0, v)$ diagram (see Fig. (6.7)) is preserved in the ADE phase diagram, i.e., data above this line stay above, data below stay below. The dotted lines show the results of two different constraint fits of the linear model (6.26) to the experimental vesicle trajectory (compare Table (6.1)). The simplest possibility ($t_2 = 0, t_3 = 0$), which allows only for a simple hyperbola parameterized by the differential area of the vesicle at $v = 1$ (Δa_0^s), gives a poor fit of the data. This is because the experimental trajectory is much steeper than a hyperbola. This behavior is reproduced when either $t_2 \sim c_v$ or $t_3 \sim \gamma$ is allowed to be different from zero in addition to $t_1 = \Delta a_0^s$. See the text for a critique of these fits.

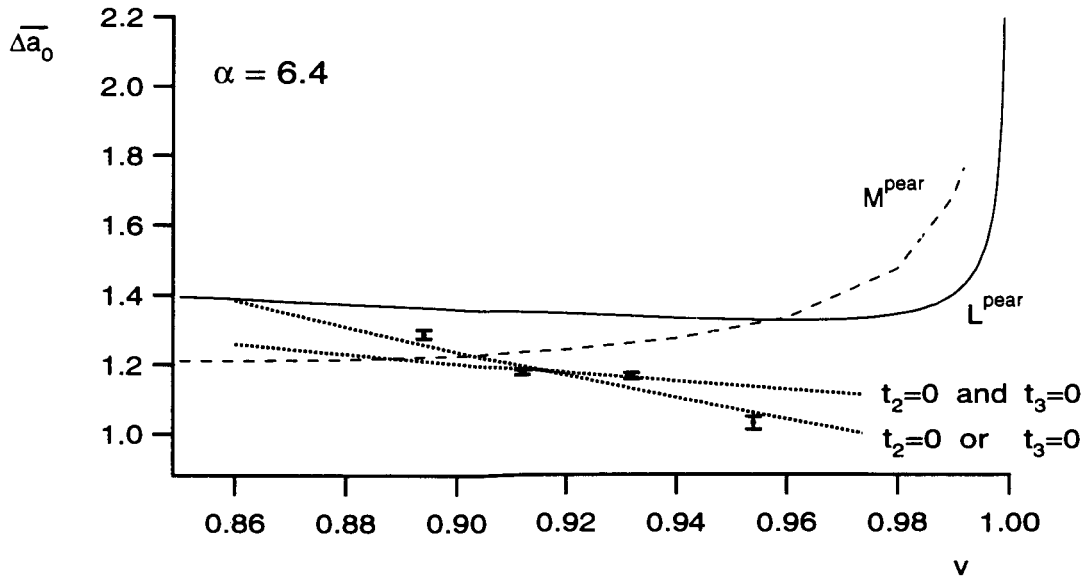

Figure 6.9: Trajectory of vesicle "A" for $\alpha = 6.4$ in the ADE phase diagram. The results of two different constraint fits of the linear model (6.26) to the experimental vesicle trajectory is shown (compare Table (6.1)). Note the different location of the crossing point of the lines M^{pear} and L^{pear} for $\alpha = 6.4$ as compared to $\alpha = 1.4$ (see Fig. (6.8)). The dependence of this crossing point on α leads to a change in the relative position of the experimental data to the limiting line (L^{pear}) with α (compare Fig. (6.8)). In contrast, the relative location of the spinodal line (M^{pear}) to the experimental data does not depend on α.

boundary for α found above. (The results for the case $\alpha = 6.4$ show the same general trends and are added to Table (6.1) for completeness (compare also Figs. (6.9).))

We start with the simplest possible fit, i.e., we allow only the parameter $t_1 \equiv \Delta a_0^s$ (Eq. (6.26)) to be different from zero. Such a fit gives the quite reasonable value $\Delta a_0^s = 1.5 \pm 0.1$ for the relaxed area difference at the sphere. Unfortunately, the resulting trajectory fits the experimental data rather poorly, as is evident from Fig. 6.8. This is due to the fact that the experimental trajectory is much steeper than a simple hyperbola. Allowing, in addition, either t_2 or t_3 to be different from zero gives a much better fit. These two cases are not distinguishable graphically, and the other pointed line in Fig. 6.8 represents both of them. Numerically, the numbers are rather different. The assumption of a vanishing thermal asymmetry leads to large parameters t_1 and t_2 with opposite signs. This would correspond to a critical balance between the two bending energy terms, which seems unlikely. On the

α	t_1	t_2	t_3
1.4	19 ± 7	-19 ± 7	0
6.6	4.4 ± 1.4	-3.5 ± 1.5	0
1.4	0.5 ± 0.4	0	-12 ± 5
6.6	0.89 ± 0.08	0	-2.3 ± 1.0
1.4	1.5 ± 0.1	0	0
6.6	1.08 ± 0.02	0	0

Table 6.1: Results of different fits of the model (6.26) to the experimental data shown in Figs. 6.8 and 6.9. A full fit to three parameters is ill defined because of the limited number of experimental points available. Setting $t_1 = 0$ is not physically meaningful since a finite area difference is intrinsic to the bilayer structure. Setting $t_2 = 0$ corresponds to the absence of an intrinsic spontaneous curvature. For $t_3 = 0$ there is no thermal asymmetry. Thus, the simplest physically sensible restricted fit is just $t_2 = t_3 = 0$.

other hand, allowing for a thermal asymmetry at vanishing spontaneous curvature gives quite a reasonable values for the scaled area difference of the sphere, $\Delta a_0^s = 0.5 \pm 0.4$. The thermal asymmetry γ is positive and on the order of 0.04 for $b \simeq 500$. A full fit to all three parameters is ill defined and not elucidating.

An analysis of vesicle "B" gives the same qualitative results. (As can be seen in Fig. 6.7, the trajectory of vesicle "B" has roughly the same slope as the trajectory of vesicle"A".) For vesicle "C", there is only one point and we do not have information on a thermal trajectory of this vesicle.

Indeed, it is impossible accurately to map vesicles with reduced volume v too close to unity into the ADE diagram. This is *not* only due to the fact that the experimental error becomes larger as $v \to 1$ (which it does!) but there is also a deeper reason. In the spherical limit, the energies of the prolate and oblate shape become degenerate, and so does the energy of the (nonaxisymmetric) saddle point between these two shapes. Thus, the vesicle samples all available phase space and the notion of a phase diagram is not sensible any more, as we have already discussed in Chapter 2. In this intermediate regime, thermal corrections to the mean vesicle shape become increasingly important.

What have we learned from these attempts to fit the thermal trajectories? Note, first, that allowing the parameter γ to be nonzero cannot change the discrepancy we have observed with vesicle "A," which became unstable to budding far beyond the spinodal. Furthermore, the fits with nonzero values of t_2 and t_3, although they are cosmetically improved over the simplest fit with $t_2 = t_3 = 0$, seem to involve large values of the parameters and dubious cancellations. In sum, then, we are inclined to believe that there is no hard evidence for the existence of asymmetric thermal behavior of the monolayers or for large intrinsic

spontaneous curvature. What, then, is causing the apparently anomalous steepness of the observed trajectories? At this point, we do not know and can only speculate. Perhaps, the thermal and gravitational corrections play a role (see Sec. (6.6)). Note, in any case, that, even without corrections, all experimental budding trajectories approach the spinodal line along paths of increasing Δa_0. This is exactly what one would expect from the most simple model trajectory, Eq. (6.21).

6.6 Corrections to the Mapping

In this Section, corrections to the mapping of experimental shapes into the ADE phase diagram are discussed. It was implicitly assumed in the that last few paragraphs that vesicle shapes are described by the $T = 0$ ADE model; however, there are three main effects which alter the mean shapes of real vesicles in the laboratory. First, experiments are done at finite temperature, whereas the ADE phase diagram is obtained from a zero temperature calculation. As was mentioned already in Chapter 2, thermal fluctuations in the presence of geometrical constraints leads to shifts in average mode amplitudes away from $T = 0$ values, even at the Gaussian level. This effect will be described in Sec. 6.6.1. Second, the vesicles are assumed to be axisymmetric; but, the gravitational force, which is crucial to orient the vesicles in the chamber, tends to break this symmetry and will have the effect of partially flattening the shapes. In Sec. 6.6.2, we will discuss this phenomenon and how it might affect our observations. And, third, we have found (see Chapter 5) that vesicles are in general slightly asymmetric, even in the theoretically "symmetric" prolate state of the ADE model. This point will be briefly discussed in Sec. (6.6.3).

6.6.1 Finite Temperature Amplitude Shifts

At a finite temperature, a vesicle is fluctuating around its equilibrium mean shape. These thermal fluctuations need excess area which is taken out of the mean shape. This effect, which influences both the mean amplitudes of the shape as well as its apparent reduced volume $\bar{v}_e \neq v$, [16] is a direct result of the volume and area constraint on the vesicle.

In general, we may write the mode amplitudes at $T > 0$ as

$$a_n =< a_n > +\delta a_n, \tag{6.27}$$

where the mean amplitude is a combination of a zero temperature value $a_n^{(0)}$ and a thermal shift $\Delta_n(T)$,

$$< a_n >= a_n^{(0)} + \Delta_n(T), \tag{6.28}$$

and, by definition, $< \delta a_n >= 0$ and $\Delta_n(0) = 0$. Note that the amplitude correlation functions,

$$< a_m a_n > - < a_m >< a_n >=< \delta a_m \delta a_n >, \tag{6.29}$$

and their higher-order analogs do not, in general, vanish for $T > 0$.

[16] Thermal fluctuations do not, of course, change the actual area and volume of the vesicle, so its reduced volume v is not affected. What is at issue here is the quality of the approximation, $v = \langle v_e \rangle$, which we use. As discussed in Sec. (4.3.3), this procedure has (small) corrections when thermal fluctuations are present.

To build a $T = 0$ phase diagram from $T > 0$ experiments, we need to be able to extract v and $a_4^{(0)}$ from the finite-temperature measurements. In the case of v, we have already discussed this point in Sec. (4.3.3). The upshot is that we need to be able to calculate the shifts $\Delta_n(T)$ and correlations $< \delta a_m \delta a_n >$ from the theory. This problem is unsolved, in general, but it has been solved at the Gaussian level. [17]

In a recent publication by U. Seifert [68], a formalism for calculating thermal fluctuations at lowest (Gaussian) order in k_BT/κ for non-spherical vesicles has been developed. In contrast to all previous calculations on vesicle fluctuations, the volume and area constraints are handled exactly within Gaussian approximation. The result is that both the shifts $\Delta_n(T)$ and correlations $< \delta a_m \delta a_n >$ are linear in T, so

$$< \Delta_n > \sim \frac{k_BT}{\kappa} \tag{6.30}$$

and, for example,

$$< \delta a_4 \delta a_4 > \sim \frac{k_BT}{\kappa} \, . \tag{6.31}$$

For our system, the parameter $k_BT/\kappa \simeq 0.04$. Note, in particular, that in this regime the shifts are always smaller than the rms fluctuations, which are on the order of $(k_BT/\kappa)^{1/2}$. Thus, if the Gaussian approximation is applicable, we may conclude that all thermal corrections are typically smaller than experimental errors and can be neglected, as we have done earlier in the text. In particular, as long as the Gaussian approximation is valid, thermal corrections may be expected to contribute at most small corrections to the thermal trajectories.

Unfortunately, it is not possible to assume that the Gaussian approximation is always valid. Indeed, numerical implementation by Marija Nikolic [76] of the formalism developed in [68] shows that the thermal shifts diverge both at the sphere and at the spinodal line of the budding transition. These divergences signal failures of the Gaussian approximation. Near the sphere, the effect arises because the strict geometrical constraints on the area and volume hinder the thermal fluctuations and force them into higher and higher modes. The Gaussian-level divergence occurs because more and more modes are excited at $v \to 1$. Near the spinodal line the divergence is caused by the onset of the soft mode, which cannot be

[17] It is interesting to note that $\Delta_2(T)$ may be obtained directly from experimental data by using the amplitude hierarchy. The thermal shift of the second amplitude is found by comparing the measured value $\langle a_2 \rangle$ with the quantity $a_2 = \sqrt{\frac{135}{64}}(1 - v(T))$ which may be thermally extrapolated from the "sphere point" of the vesicle at some temperature T_s. At the sphere point the reduced volume is known to be unity, i.e. $v(T_s) = 1$. Thus, its value at a temperature $T > T_s$ can be obtained from Eq. (6.24) when the thermal area expansion coefficient is known. The a_2 amplitude corresponding to the zero temperature shape can then be obtained in first order from the equation given above. Thus, the shift is given by the difference $\langle a_2 \rangle - \sqrt{\frac{135}{64}}(1 - v)$, at least to first order in $(1 - v)$.

treated perturbatively. In both cases, a new small parameter appears in addition to k_BT/κ. Near the sphere we have $(1-v) \to 0$, whereas near spinodal lines $(v - v_s) \to 0$. Thus, at both limits of the prolate phase, the Gaussian treatment of the fluctuations fails and there may be appreciable thermal corrections to the phase mapping data.

It is possible that these corrections would improve agreement between the calculated and measured thermal trajectories. We do not at this point know whether or not this is true. It has not been possible to treat the thermal fluctuations beyond the Gaussian level. Concern has even been expressed that, to go beyond the Gaussian level, corrections to the Liouville factor of the measure would have to be applied [68]. In this situation is is even difficult to estimate with any certainty the precise bounds of the region in which the Gaussian approximation is reliable. For these reasons, we have not at this time attempted systematic thermal corrections of our experimental data. However, we expect that a careful examination of these points will be possible in the immediate future.

6.6.2 Gravity

The effect of gravity can be roughly estimated by considering the ratio of the relevant energy scales. The bending energy is independent of length and its order of magnitude is given by $E_{\text{bending}} \sim 8\pi\kappa$. The gravitational energy of a vesicle sitting at a wall is roughly

$$E_{\text{gravity}} \sim \Delta\rho(\frac{4\pi}{3}R^3)gR, \tag{6.32}$$

where $\Delta\rho$ is the density difference between the inside and outside solution and g is the gravitational constant. The ratio of these two energies is, therefore,

$$G \equiv \frac{g\Delta\rho R^4}{6\kappa}. \tag{6.33}$$

For $G \gg 1$, gravity will dominate and all vesicle will become more or less flat oblates, depending on their reduced volume. (This is because the minimal distance of the center of gravity from the chamber floor is smaller for an oblate than for a prolate vesicle for given volume and area.) For $G \ll 1$, the bending energy will determine the vesicle shape, and the axisymmetry of a prolate vesicle oriented with its axis parallel to the chamber wall will be only slightly broken by gravity. G is critically dependent on the vesicle radius R. Very large vesicles will almost always be flat oblates, largely independent of the density difference. This is, indeed, found in experiment.

The G values of the vesicles discussed in this chapter are given in Tab. 6.2 for the density difference of $\Delta\rho = 4\ g/l$ employed. It would appear that gravity is not an overwhelming

vesicle	G	S	R in μm
A	0.4	256	8.8
B	0.06	36	5.4
C	0.35	223	8.5

Table 6.2: G and S Values of vesicles discussed in the text. The vesicle radius R is also given.

factor in determining vesicle shapes. However, this naive scaling argument is somewhat deceiving, since it is the available *changes* in shape for a given reduced volume which are relevant for the calculation of energy differences. It turns out that vesicles with a high reduced volume are more deformed than those with a smaller value of v [77].

Note that reducing the vesicle weight diminishes the gravitational effect but leads to a less effective stabilization of the symmetry axis within the focal plane. For our technique, this stabilization is crucial for recording time series of vesicle contours. We may estimate crudely the degree of stabilization by looking at the ratio of gravitational to thermal energies,

$$S \equiv \frac{(4\pi/3)\,\Delta\rho g R^4}{k_B T} \,. \tag{6.34}$$

Vesicles with a large $S > 1$ are well stabilized. Vesicle with small $S < 1$ tend to rotate their symmetry axis out of the focal plane under brownian motion, eventually, for $S \ll 1$, rotating freely in the observation chamber. The S values of vesicle A,C, and D are given in Tab. 6.2 along with the vesicle radii. Of course, again, it is really not the total gravitational energy which should be compared to $k_B T$ in Eq. (6.34). Instead, it should be the characteristic differences of gravitational energy between different vesicle orientations, which could be much smaller, especially for vesicles with reduced volumes near unity.

Overall, the "best" vesicles for contour observation are those which are sufficiently stabilized without getting deformed too much. These two requirements define an observational window given by the radii corresponding to $S = 1$ and $G = 1$, respectively. For the parameters given above, we find

$$\begin{aligned} R_{S=1} &= 2.2\ \mu m \\ R_{G=1} &= 11.2\ \mu m \end{aligned} \tag{6.35}$$

Thus, the optimal vesicle should have a radius of about 7 μm. We have tried to select vesicles for observation which are close to this value.

How do these two counteracting effects influence the mapping into the phase diagram? An elliptical contour of an initially prolate vesicle, which is seen in the fixed focal plane

of the microscope, will gradually become circular [18] as G becomes larger. [19] Therefore, the absolute values of all amplitudes tend to zero, and the effective reduced volume $\langle v_e \rangle$ approaches unity. (For a given G, the amplitudes will be increasingly underestimated as the reduced volume gets larger.) Likewise, as S becomes smaller, the vesicle appears more spherical in the mean, since an increasing number of vesicle configurations with their symmetry axes out of the focal plane are included in the average. Again, the amplitudes are under- and the reduced volume is overestimated.

The effect of underestimating the amplitude of the fourth mode, which has been used to determine $\tilde{c}_0$ and $\overline{\Delta a}_0$, respectively, depends on both shape parameters, $\tilde{c}_0$ and v (see Fig. (6.1)). Unfortunately, detailed calculations of the effective shape amplitudes in a suitable cross section of a non-axisymmetric vesicle are not yet available. Thus, at present, we are unable to correct our data reliably.

6.6.3 Residual Asymmetry

We have found in Sec. (5.4.2) that "prolate" vesicle shapes have in general a slightly broken up/down symmetry. This is expressed in a small admixture of odd modes to the shape. The dominant contribution comes from the third mode. We find $\langle a_3 \rangle < 0.05$. Thus, the effective reduced volume of a pear shaped vesicle,

$$v_e^{\text{pear}} \approx v_e^{prolate} - \frac{27}{70} \langle a_3 \rangle^2 , \tag{6.36}$$

deviates from the value for a prolate vesicle with the same reduced volume v. However, typical differences are very small. From the maximal value for $\langle a_3 \rangle$ given above, we find $(27/70)\ (0.05)^2 \approx 10^{-3}$. Therefore, the effect on the measurement of v is on the order of the experimental error and may be neglected.

It is not so obvious whether $\langle a_4 \rangle$ is also not affected. Actually, the numerical values one finds for $\langle a_4 \rangle$ and $\langle a_3 \rangle$ can be of the same order of magnitude. However, gaining confidence from the negligible effect on the reduced volume, we conjecture that there is only a small cross-coupling between even and odd modes. Thus, the derived parameters $\tilde{c}_0$, or $\overline{\Delta a}_0$, should not be affected much by a small admixture of odd modes to the up/down symmetric shape described by $(v, \tilde{c}_0)$.

[18] Note that the cross section of an oblate with its symmetry axis oriented perpendicular to the focal plane is circular.

[19] There is, in fact, a transition of the non-axisymmetric vesicle to an oblate at some finite value of G [77].

Chapter 7

Summary

In this Thesis, we have developed a new technique for quantitative vesicle shape analysis. We have taken video phase contrast images of SOPC vesicles in aqueous solution and carried out for the first time a fully quantitative shape analysis, comparing the observations with the predictions of the area-difference elasticity (ADE) model. In particular, we have concentrated on thermal trajectories of prolate shapes which lead to the budding transition.

Fluid lipid vesicles have been prepared from 1-Stearoyl-2-Oleoyl-sn-Glycero-3-Phosphatidylcholine (SOPC) in a sucrose/glucose solution. Vesicles were observed in a sealed microchamber, which prevented evaporation of the exterior solution, in order to keep the vesicle volume constant. Shape changes were induced by heating the vesicle sample, thereby increasing the membrane area of the vesicle. The volume-to-area ratio was used as the principal control parameter of vesicle shapes.

The outcome of the observations is a set of video images of vesicle-shape contours. We have developed a protocol for digitizing a subset of these shape contours. We have discussed in detail the procedures for reconstructing three-dimensional shapes from the digitized two-dimensional contours. The shape contours include the effects of thermal fluctuations, and a set of such contours at fixed temperature T constitutes a sampling of a thermal ensemble. To parameterize each particular image, we have chosen the instantaneous principal axis to be the reference frame and we have developed a procedure for describing the shape in terms of a set of Fourier amplitudes. The thermal ensemble is then characterized by the set of these amplitudes or, more precisely, by the mean amplitudes and the amplitude-amplitude correlation functions. We have discussed the relation between these mean amplitudes and correlation functions and important physical control parameters like the area and volume of the vesicle and the area-difference between its inner and outer monolayer leaves.

We have studied in detail a small sample (see the comments in Sec. (3.4.1)) of initially prolate vesicles. When heated slowly along a "thermal trajectory," these vesicles become progressively more elongated and then become suddenly and discontinuously unstable to shape transformation called "budding," in which a small child vesicle forms connected to the parent vesicle by a narrow neck. We have made a careful study of the precursors to this instability. We find, in particular, that the instability is preceded by a dramatic growth in both the magnitude of thermal fluctuations and characteristic relaxation time observed in the time-dependent amplitude-amplitude correlations. We have shown how both these phenomena are quantitatively consistent with interpretation of budding as a "spinodal" instability, i.e., the final decay of a metastable state, as it approaches its limit of stability. We have showed how this interpretation fits into the ADE model and is consistent with other measurements. We conclude that the budding transition of micron-scale SOPC vesicles is probably a first-order transition mediated by a spinodal instability.

The principal unexplained feature of these budding experiments is the systematic appearance of a small but detectable up/down asymmetry in the prolate phase, which is in principal symmetric. This asymmetry is small but detectable deep in the prolate phase. It's effect is apparently magnified near the instability by the "softness" of the mode which becomes unstable at the spinodal. We have estimated the magnitude of the asymmetry necessary to cause this symmetry breaking in the prolate phase. We find that it is small on the scale of other bending-energy contributions. We hypothesize that this symmetry-breaking field is an extrinsic effect, most likely due to a structural or chemical inhomogeneity of the vesicle which is on too small a scale to be visually detectable.

We have discussed at length the theoretical and practical issues involved in "mapping" the observed vesicles and thermal trajectories in the ADE-model phase diagram, in order to test for the first time in a quantitative manner the agreement between theory and experiment. This involved extracting from the data the reduced volume v and effective relaxed area difference $\overline{\Delta a}_0$ for each vesicle. We have explained how to deduce these parameters from the average mode amplitudes for the near spherical prolate region of the phase diagram. The method makes extensive use of the fact that the average mode amplitudes in this region have a "hierarchical" structure, i.e., the higher Fourier modes have successively less weight. Using these simplifications, we have successfully mapped a series of experimental trajectories into the ADE phase diagram. The results of the mapping are largely but not entirely consistent with the predictions of the ADE model. In particular, the effective spontaneous curvature $\tilde{c}_0$ and the stability of the experimental vesicles is in good agreement with

the theory. The observed thermal trajectories are qualitatively consistent with theoretical expectations but appreciably steeper than those expected from the ADE model.

Finally, we have discussed possible reasons for the observed discrepancies. The two major candidates are thermal-fluctuation effects and gravitational distortions. Thermal fluctuations give generically small corrections to zero-temperature amplitudes because the ratio κ/k_BT of the bending elastic energy to thermal energies is small. This simple estimate is good provided that fluctuation effects may be treated in the Gaussian approximation. The Gaussian approximation fails both near the sphere and near the spinodal line, so in these regions thermal corrections may become appreciable. Unfortunately, calculations beyond the Gaussian level have not yet been carried out, so we cannot say how important these corrections may become and over what region. Gravitational corrections may be expected to occur because the experimental vesicles are prepared to be slightly more dense than the surrounding fluid, in order that they should sink to the floor of the experimental cell (for easy observation) and (for prolates) to restrict the range of axial orientation to the focal plane of observation. Too small a density difference makes observation difficult; but, too large a difference causes gravitational distortion of the pure-bending-energy shapes predicted by the theory. We believe that these distortions are small but they are not fully controlled at this point and may not be negligible.

Although it is not possible to make these corrections now, it may become possible in the near future [78]. Once the necessary corrections to shape data are performed, we will have direct access to the extrinsic elastic parameters, spontaneous curvature C_0 and effective area difference ΔA_0 of the membrane. In principle, we have already extracted these quantities from the data via a fit of the thermal trajectories. Although we have provided proof-of-concept, the numerical values cannot be trusted without corrections. We emphasize in closing that the techniques for quantitative shape measurement and analysis that we have developed in this Thesis open the door to the use of vesicle shape as probes of membrane solute/solvent interactions. That is, shape changes of vesicles can be used to monitor - via measurements of, e.g., the spontaneous curvature - the influence of the membrane environment on the elastic properties of the membrane. We expect valuable information from this technique.

Appendix A

The Hierarchy of Shape Amplitudes

In this Appendix, we recall analytical results in the spherical limit presented by L. Miao in [57] for equilibrium vesicle shapes. We will use these results to derive the hierarchy of shape amplitudes in our shape representation, Eq. (6.13).

A.1 The Spherical Limit

In [57], the shape of a vesicle is represented as a spherical harmonic expansion of the radial distance between the shape contour and the origin,

$$R(\theta) = R\left(1 + \sum_{l=2}^{\infty} u_l Y_{l,0}(\theta)\right). \tag{A.1}$$

The shape is assumed to be axisymmetric, so there are no $m \neq 0$ amplitudes. Further, Euclidian invariance allows u_1 to be set to zero without loss of generality. The area and volume of the vesicle are given by

$$A = 4\pi R_v^2(1+\Delta)\,, \quad V = \frac{4\pi}{3}R_v^3\,, \tag{A.2}$$

respectively, where Δ measures the excess area over the sphere. $\Delta^{1/2}$ is used here as a small parameter near the spherical limit. The excess area is related to the reduced volume according to $\Delta = v^{-2/3} - 1$. Both quantities are equivalent measures of the deviation of the volume-to-area ratio from its value for the sphere. The overall radius is given by

$$R \;=\; R_v\left(1 - \frac{1}{2}\Delta\right) \;+\; O(\Delta^{\frac{3}{2}})\,. \tag{A.3}$$

The equilibrium values for the amplitudes u_l are found by minimizing the bending-energy functional of the spontaneous curvature model via an expansion in the small parameter $\Delta^{1/2}$. For up/down symmetric prolate vesicles, one finds that all the odd amplitudes u_{2n+1} are zero and the even amplitudes scale according to $u_{2n} = O(\Delta^{\frac{n}{2}})$. The first few terms of this "hierarchy" in the small parameter $\Delta^{1/2}$ take the forms,

$$\begin{aligned} u_2 &= \sqrt{2\pi}\,\Delta^{\frac{1}{2}} + \frac{\sqrt{5\pi}}{21}\Delta + O(\Delta^{\frac{3}{2}}), \\ u_4 &= \frac{\sqrt{\pi}}{49}(R_v\tilde{C}_0 + 32)\,\Delta + O(\Delta^{\frac{3}{2}})\,. \end{aligned} \tag{A.4}$$

We show now that this hierarchy holds also in our shape representation. In this regard, we relate the two different representation and, then, use Eq. (A.4). The transformation between the two expansions Eq. (6.10) and Eq. (A.1) is non-linear. Thus, we may write formally

$$a_m = I_{nm}u_n + I_{nkm}u_n u_k + O(u^3). \tag{A.5}$$

As shown in App. A.2, the matrix (I_{nm}) has a triangular form, and its components are zero for $m > n$. It is this property which ensures that the mode hierarchy carries over to our representation. To linear order in Δ, one gets

$$\begin{aligned} a_2 &= \underbrace{I_{22}u_2}_{\Delta^{1/2}} + \underbrace{I_{42}u_4 + I_{222}u_2^2}_{\Delta^1} \\ a_4 &= \underbrace{I_{44}u_4 + I_{224}u_2^2}_{\Delta^1}\,. \end{aligned} \tag{A.6}$$

In the equation above, we have explicitly used the fact that $I_{24} = 0$, i.e., that the linear term in the expansion of $a_4(u_2)$ is absent. In order to find the coefficients of Eq. (6.13), we just have to convert the expansion in Δ, Eq. (A.4), into an expansion in $(1-v)$ and then insert the result into Eq. (A.6). With

$$\Delta = \frac{2}{3}\,(1-v) + O(\,(1-v)^2\,) \tag{A.7}$$

we find

$$\begin{aligned} a_2 &= A_1\,(1-v)^{\frac{1}{2}} + \{B_1\tilde{c}_0 + B_2\}\,(1-v) \\ a_4 &= \{B_3\tilde{c}_0 + B_4\}\,(1-v) \end{aligned} \tag{A.8}$$

where the coefficients are given by

$$\begin{aligned} A_1 &= \tfrac{2}{3}\sqrt{3\pi}\, I_{22} \\ B_1 &= \tfrac{2}{147}\sqrt{\pi}\, I_{42} \\ B_2 &= -\tfrac{2}{63}\sqrt{5\pi}\, I_{22} + \tfrac{64}{147}\sqrt{\pi}\, I_{42} + \tfrac{4}{3}\pi\, I_{222} \\ B_3 &= \tfrac{2}{147}\sqrt{\pi}\, I_{44} \\ B_4 &= \tfrac{64}{147}\sqrt{\pi}\, I_{44} + \tfrac{4\pi}{3}\, I_{224}\,. \end{aligned} \tag{A.9}$$

These are the coefficients of Eq. (6.13). The matrix (I_{mn}) is written down in the next section. We have not attempted to calculate the tensor (I_{kmn}), since it is not needed explicitly for the mapping, which we perform numerically.

A.2 Linear Transformation Matrix I for $u_n \rightarrow a_n$.

The transformation matrix I has been obtained by Dr. Udo Seifert [79]. We note the result of his calculation. The matrix I defined by Eq. (A.5) is given by

$$I_{nm} = \frac{1}{\pi}\frac{m^2-1}{m}\int_0^{2\pi} Y_{n0}(\cos\theta)\cos(m\theta)\, d\theta, \tag{A.10}$$

which is zero for $m > n$ or $n - m$ odd. The Y_{n0} are the spherical harmonics for $m = 0$.

Appendix B

Fluctuating Symmetry Axis

The shape representation described in Sec. 4.1 uses the principal axis of the contour as a reference system. The problem with such a choice is that this reference system actually depends on the contour and is not fixed. The principal axis fluctuates thermally around the symmetry axis of the mean shape, which, itself, exhibits rotational diffusion (see Fig B.1). The natural reference system would be the symmetry axis of the mean shape. However, the

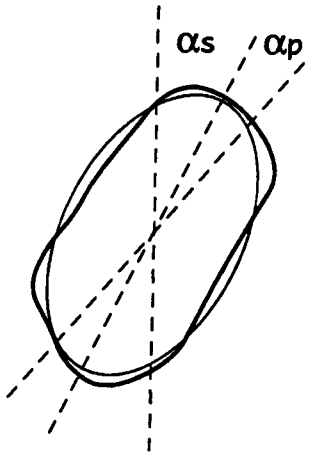

Figure B.1: The angle α of the principal axis with the vertical can be decomposed into a sum of the angle α_s of the symmetry axis with the vertical and of the angle $\Delta\alpha$ of the symmetry axis with the principal axis.

instantaneous principal axis of each individual shape is a good estimate for the symmetry axis of the mean shape, since both axes are identical for a rotationally symmetric shape and since the shape fluctuations, which break the rotational symmetry, are relatively small. It is even a "best" estimate in the sense that it is the most symmetric division of the contour in two halves: One can show by direct minimization that the slopes $k_\pm$ of the principal axis

(see Eq. (4.7)) are minima of the functional,

$$d(k) = \sum_{i=1}^{N} d_k^2(x_i, y_i) \ , \tag{B.1}$$

where $d_k(x_i, y_i)$ is the orthogonal distance of the contour point (x_i, y_i) to the line $y = kx$ through the center of "mass."

If one knew the angle α_s between the symmetry axis and the vertical y axis (see Fig. (B.1)), the contours could be aligned independently of their deviation from the mean shape. (We assume for simplicity that the symmetry axis is located within the focal plane of the microscope. Effects of out-of-plane fluctuations are discussed in Sec. 6.6.2.) The idea is that one may obtain the mean symmetry axis by averaging the ("quick") fluctuations of the principal axis over short times and, then, expanding the contour with respect to this averaged axis. [1] In order better to understand the behavior of the principal axis, we formulate now a simple dynamical model for its angle α with the vertical.

The angle $\alpha = \alpha_s + \Delta\alpha$ is a stochastic variable (under thermal fluctuation) and the underlying dynamics may be modeled as a superposition of an overdamped harmonic oscillation of $\Delta\alpha$ and the Brownian motion of α_s. The longest time scale for the first process is determined by the relaxation time for the lowest eigenmode of the vesicle, $\tau_f \lesssim \frac{\eta R_v^3}{\kappa}$. The second process is characterized approximately by the rotational diffusion constant, $D_r = \frac{kT}{8\pi\eta R_v^3}$, of a sphere with radius R_v. Assuming that the stochastic forces on the two angles are uncorrelated, we find for the correlation function of α

$$\begin{aligned} < \alpha(0)\alpha(t) > \ &\simeq \ < \Delta\alpha(0)\Delta\alpha(t) > \ + \ < \alpha_s(0)\alpha_s(t) > \ = \\ &= \ < (\Delta\alpha)^2(0) > \exp(-\frac{t}{\tau_f}) \ + \ D_r t + \ \alpha_s(0)^2 \ . \end{aligned} \tag{B.2}$$

The *relevant* time scale for the rotational diffusion is, therefore, $\tau_r = \frac{<(\Delta\alpha)^2(0)>}{D_r}$. If the ratio,

$$\frac{\tau_f}{\tau_r} \lesssim \frac{kT}{\kappa} \frac{1}{8\pi < (\Delta\alpha)^2(0) >} \ , \tag{B.3}$$

were small, "fast" oscillations of the principal axis could be averaged out to obtain the mean symmetry axis, without introducing correlations due to the "slow" rotational diffusion of the mean symmetry axis. Taking $\frac{kT}{\kappa} \simeq 0.04$ and estimating $< (\Delta\alpha)^2(0) > \simeq (0.05)^2$ from a running average on α,

$$< \alpha >_n = \frac{1}{2n+1} \sum_{i=-n}^{n} \alpha_i \ , \tag{B.4}$$

[1] One might think that, because of the fluctuations of the principal axis *around* the symmetry axis, the averages of the two sets of amplitudes, $\{a_n|_{\alpha_s}\}$ and $\{a_n|_{\alpha}\}$, are equal. However, this is not true, because of the shift of the integration interval in Eq. 4.14.

over a time on the order τ_f, one gets the crude estimate,

$$\frac{\tau_f}{\tau_r} \simeq 1 . \tag{B.5}$$

Thus, the time scales are *not* well separated and, unfortunately, it is not possible to extract the mean symmetry axis.

Nevertheless, the differences between the mean amplitudes with respect to the principal axis and those with respect to a time-averaged principal axis are within statistical fluctuations for an average over short times (see Fig. B.2). We conclude, therefore, that it does not make any difference at this level of precision whether the contours are expanded with respect to the instantaneous principal axis or to the mean symmetry axis.

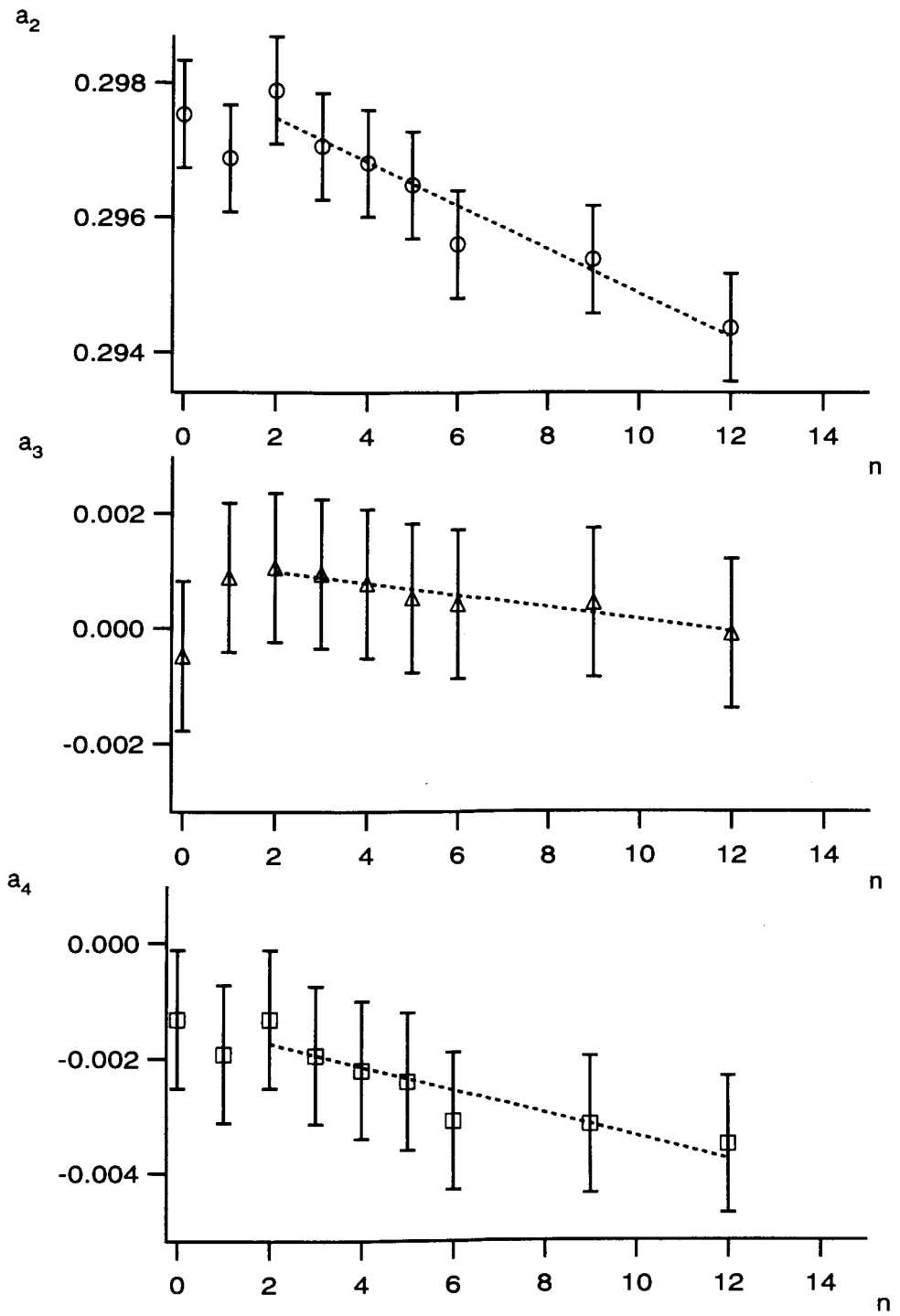

Figure B.2: Effect of performing running averages of α on the mean shape amplitudes $\{a_n\}$. There is no significant effect on the amplitudes for short averaging times. ($n = 2$ corresponds to a time window of approximately 2 s.) Long averaging times lead to correlations due to the rotational diffusion of the mean symmetry axis.

Appendix C

Landau Theory for an External Asymmetry

In the following, we repeat a calculation performed by U. Seifert [79]. For a transition out of an asymmetric shape the Landau potential reads

$$V(a_u) = \kappa[-ha_u + \frac{1}{2}\tau\ a_u^2 - \frac{1}{4}g\ a_u^4 + \frac{1}{6}u\ a_u^6]. \tag{C.1}$$

With the ansatz $a_u = \sqrt{\tau/g}\ f$, one obtains

$$V(f) = \kappa(\tau^2/2g)[-2yf + f^2 - \frac{1}{2}\ f^4], \tag{C.2}$$

where $y = \sqrt{g/t^3}\ h$, and we have ignored the sixth order term which we don't need for the decay. The metastable state (a_u^-) and the saddle point (a_u^+) are given by

$$a_u^\pm = \sqrt{\tau/g} f^\pm(y), \tag{C.3}$$

where $f^\pm$ are the two positive solutions of the relation,

$$f - f^3 = y. \tag{C.4}$$

The instability, i.e., the annihilation of the metastable state against the saddle point, is at $y = y_c = 2\sqrt{3}/9$, as can be seen from Fig. C.1. The energies of the minimum and the saddle point are given by

$$V(a_u^\pm) = \kappa(\tau^2/2g)(-2y\ f^\pm + (f^\pm)^2 - \frac{1}{2}\ (f^\pm)^4). \tag{C.5}$$

Near the instability, the two solutions are $f^\pm \sim \sqrt{3}/3 \pm const\sqrt{(y_c - y)}$. For the curvature, we find

$$V''(a_u^\pm) = \kappa(\tau^3/g^2)(1 - 3(f^\pm)^2) \sim \pm(y_c - y)^{1/2}. \tag{C.6}$$

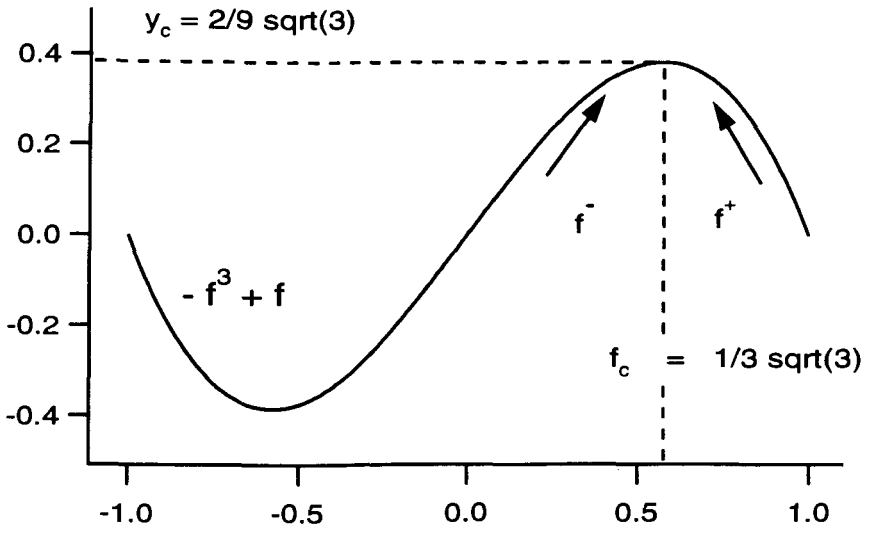

Figure C.1: The metastable state (f^-) and the saddle point (f^+) are given as the two positive solutions of $f - f^3 = y$, where y is proportional to the field h. The instability, i.e.,the point where the metastable state disappear, is located at $(f_c, y_c) = (\sqrt{3}/3, 2\sqrt{3}/9)$. Near this instability, the two solutions $f^\pm$ scale as $f^\pm - f_c \sim \pm(y_c - y)^{1/2}$.

We take $(y_c - y) \sim (T_c - T)$, as usual. Noting that $\langle (a_u - \langle a_u \rangle)^2 \rangle = k_B T / V''(a_u^-)$ and assuming the same simple dynamics as in the symmetric case, i.e., $t_c = 1/(\Gamma V''(a_u^-))$, we arrive at Eq. 5.25.

Bibliography

[1] U. Seifert, Phys. Rev. Lett. **66**, 2404-1407 (1991).

[2] B. Fourcade, M. Mutz, D. Bensimon, Phys. Rev. Lett. **68**, 2551-2554 (1992).

[3] F. Jülicher, U. Seifert, and R. Lipowsky, Phys. Rev. Lett. **71**, 452-455 (1993).

[4] X. Michalet, D. Bensimon, and B. Fourcade, Phys. Rev. Lett. **72**, 168-171 (1994).

[5] D. Marsh, *Handbook of Lipid Bilayers*, (CRC Press, Boca Raton, 1990).

[6] G. Cevc, and D. Marsh, *Phospholipid Bilayers: Physical Principles and Models*, (Wiley, New York, 1987).

[7] H. S. Seung, and D. R. Nelson, Phys. Rev. A **38**, 1005-1018 (1988).

[8] F. C. MacKintosh, and T. C. Lubensky, Phys. Rev. Lett. **71**, 1565-1568 (1993).

[9] M. Bloom, E. Evans, and O.G. Mouritsen, Quart. Rev. Biophys. **24**, 293-397 (1991).

[10] E. Evans, and D. Needham, Faraday Discuss. Chem. Soc. **81**, 267-280 (1986).
J. Phys. Chem. **91**, 4219-4228 (1987).

[11] R.D. Kornberg, and H.M. McConnell, Biochem. **10**, 1111-1120 (1971).

[12] R. Homan, and H.J. Pownall, Biochim. Biophys. Acta **938**, 155-166 (1988).

[13] B. Alberts, D. Bray, J. Lewis, M. Raff, K. Roberts, and J.D. Watson, *Molecular Biology of the Cell*, 2nd Ed, (Garland, New York, 1989).

[14] S.J. Singer, and G.L. Nicolson, Science **175**, 720-731 (1972).

[15] D. E. Golan, and P. Agre, Biophys. J. **66**, 1271-1272 (1994)

[16] Keller et al., Biophys. J. **65**, 23-27 (1993).

[17] G.F. Oster, L.Y. Cheng, H.-P.H. Moore, and A.S. Perelson, J. Theor. Biol. **141**, 463-504 (1989).

[18] E. Sackmann, Can.J.Phys. **68**, 999-1012 (1990).

[19] H.-G. Döbereiner, J. Käs, D. Noppl, I. Sprenger, and E. Sackmann, Biophys. J. **65**, 1396-1403 (1993).

[20] D. Beysens, N. Boccara, and G. Forgacs, Eds., *Dynamical Phenomena at Interfaces, Surfaces and Membranes*, Les Houches 1991, (Nova Science, New York, 1993).

[21] J. Meunier, D. Langevin, and N. Boccara, Eds., *Physics of Amphiphilic Layers*, Springer Proc. Phys. 21, (Springer, Berlin, 1987).

[22] R. Lipowsky, Nature **349**, 475-481 (1991).

[23] R. Lipowsky, D. Richter, and K. Kremer, Eds., *The Structure and Conformation of Amphiphilic Membranes*, Springer Proc. Phys. 66, (Springer, Berlin, 1992).

[24] M. Wortis, S. Udo, K. Berndl, B. Fourcade, L. Miao, M. Rao, and R.K.P. Zia, in D. Beysens, N. Boccara, and G. Forgacs, Eds., *Dynamical Phenomena at Interfaces, Surfaces and Membranes*, pp 221-235, (Nova Science, New York, 1993).

[25] M. Bessis, *Living Blood Cells and their Ultrastructure*, (Springer, New York, 1973).

[26] Y. Lange, and J. Slayton, J. Lip. Res. **23**, 1121-1127 (1982).

[27] E. Gorter, and F. Grendel, J. Exp. Med **41**, 439-443 (1925).

[28] P.B. Canham, J. Theor. Biol. **26**, 61-81 (1970).

[29] W. Helfrich, Z. Naturforsch. **28c**, 693-703 (1973).

[30] H.J. Deuling, and W. Helfrich, J. Phys. (Paris) **37**, 1335-1345 (1976).

[31] H. J. Deuling, and W. Helfrich, Biophys. J. **16**, 861-868 (1976).

[32] E. A. Evans, and Y. C. Fung, Microvasc. Res. **4**, 335 (1972).

[33] M.P. Sheetz, and S.J. Singer, Proc. Natl. Acad. Sci. **71**, 4457-4461 (1974).

[34] E.A. Evans, Biophys. J. **14**, 923-931 (1974).

[35] W. Helfrich, Z. Naturforsch. **29c**, 510-515 (1974).

[36] S. Svetina, and B. Žekš, Eur. Biophys. J. **17**, 101-111 (1989).

[37] E. A. Evans, Biophys. J. **13**, 941 (1973).

[38] E.A. Evans, Biophys. J. **30** , 265-284 (1980).

[39] D. W. Knowles, J. A. Chasis, E. A. Evans, and N. Mohandas, Biophys. J. **66**, 1725-1732 (1994).

[40] B.L.-S. Mui, P.R. Cullis, E.A. Evans, and T.D. Madden, Biophys.J. **64**, 443-453 (1992).

[41] E. Sackmann, H.P. Duwe, and H. Engelhardt, Discuss. Chem. Soc. **81**, 281-290 (1986).

[42] S. Milner, and S. Safran, Phys. Rev. A **36**, 4371 (1987).

[43] M.B. Schneider, J.T. Jenkins, and W.W. Webb, J. Phys. France **45**, 1457-1472 (1984).

[44] H. Engelhardt, H. Duwe, and E. Sackmann, J. Phys. Lett. **46**, L 395 (1985).

[45] I. Bivas, P. Hanusse, P. Bothorel, J. Lalanne, and O. Aguerre-Chariol, J. Phys. **48**, 855 (1987).

[46] J. Faucon, M. Mitov, P. Meleard, I. Bivas, and P. Bothorel, J. Phys. France **50**, 2389 (1989).

[47] H. Duwe, J. Käs, and E. Sackmann, J. Phys. France **51**, 945-962 (1990).

[48] P. Meleard, J. Faucon, M. Mitov, and P. Bothorel, Europhys. Lett. **19**, 267 (1992).

[49] K. Berndl, R. Lipowsky, E. Sackmann, and U. Seifert, Europhys. Lett. **13**, 659-664 (1990).

[50] J. Käs, and E. Sackmann, Biophys. J. **60**, 825-844 (1991).

[51] U. Seifert, K. Berndl, and R. Lipowsky, Phys.Rev. A **44**, 1182-1202 (1991).

[52] L. Miao, B. Fourcade, M. Rao, M. Wortis, and R.K.P. Zia, Phys. Rev. A **43**, 6843-6856 (1991).

[53] S.J. Eastman, M.J. Hope, and P.R. Cullis, Biochem. **30**, 1740-1745 (1991).

[54] B.L.-S. Mui, H.-G. Döbereiner, T.D. Madden, and P.R. Cullis, *Influence of Transbilayer Area Asymmetry on the Morphology of Large Unilamellar Vesicles*, submitted to Biophys. J..

[55] E. Farge, and F. Devaux, Biophys. J. **61**, 347-357 (1992).

[56] S. Svetina, M. Brumen, and B. Žekš, Stud. Biophys. **110**, 177-184 (1985).

[57] L. Miao, *Equilibrium Shapes and Shape Transitions of Fluid Lipid-Bilayer Vesicles*, Simon Fraser University, Ph.D. Thesis 1992.

[58] L. Miao, U. Seifert, M. Wortis, and H.-G. Döbereiner, Phys. Rev. E **49**, 5389-5407 (1994).

[59] U. Seifert, L. Miao, H.-G. Döbereiner, and M. Wortis, in *The Structure and Conformation of Amphiphilic Membranes*, R. Lipowsky, D. Richter, and K. Kremer, Eds., Springer Proc. Phys. 66, pp 93-96, (Springer, Berlin, 1992).

[60] M.P. do Carmo, *Differential geometry of curves and surfaces*, (Prentice-Hali, New Jersey, 1976).

[61] R. Waugh, J. Song, S. Svetina, and B. Žekš, Biophys. J. **61**, 974-982 (1992).

[62] L. Miao, priv. com.; M. Nikolic, priv. com.; U. Seifert, priv. com.; H.-G. Döbereiner, unpublished.

[63] V. Heinrich, and S. Svetina, B. Žekš, Phys. Rev. E **48**, 3112-3123 (1993).

[64] Niggeman, and W. Helfrich, priv. com..

[65] T.Wilson, and C.J.R.Sheppard, Optik **59**, 19-23 (1981).

[66] A. Dougherty, P.D. Kaplan, and J.P. Gollub, Phys. Rev. Lett. **58**, 1652-1655 (1987).

[67] A. Dougherty, and J.P. Gollub, Phys. Rev. A **38**, 3043-3053 (1988).

[68] U. Seifert, *The concept of effective tension for fluctuating vesicles*, Z. Phys. B, in press.

[69] L Miao, and M. Nikolic, priv. com..

[70] U. Seifert, and S.A. Langer, Europhys. Lett. **23**, 71-76 (1993).

[71] J. Käs, et al., J. Phys. II France **3**, 631-645 (1993).

[72] U. Seifert, *Morphology and dynamics of budding of vesicles*, Workshop on "Interplay of genetic and physical processes in the development of biological form"; Les Houches, 1994; Organizers: D.Beysens, M-A.Felix, G.Forgacs, and F.Gaill; to be published in: Springer-Editions de Physique.

[73] B. Fourcade, L. Miao, M. Rao, M. Wortis, and R.K.P. Zia, Phys. Rev. E **49**, 5276-5286 (1994).

[74] A. Yeung, University of British Columbia, PhD. Thesis 1994.

[75] E. Sackmann, priv. com..

[76] M. Nikolic, priv. com..

[77] M. Kraus, U. Seifert, priv. com..

[78] M. Kraus, U. Seifert, and R. Lipowsky, priv. com..

[79] U. Seifert, priv. com..